



DEPARTMENT OF PHYSICS
TECHNISCHE UNIVERSITÄT MÜNCHEN

Dissertation

Molecular functionalization of *h*-BN

Domenik Matthias Zimmermann





DEPARTMENT OF PHYSICS

TECHNISCHE UNIVERSITÄT MÜNCHEN

Molecular functionalization of *h*-BN

Vollständiger Abdruck der von der Fakultät für Physik der Technischen Universität München zur Erlangung des akademischen Grades eines Doktors der Naturwissenschaften (Dr. rer. nat.) genehmigten Dissertation.

Author:	Domenik Matthias Zimmermann
Supervisor:	Prof. Dr. Wilhelm Auwärter
Submission Date:	TODO: Submission date
Chairman:	TODO: Chairman
1. Examiner:	TODO: 1. Examiner
2. Examiner:	TODO: 2. Examiner

I assure the single handed composition of this dissertation only supported by declared resources.

Munich, TODO: Submission date

Domenik Matthias Zimmermann

Acknowledgments

Abstract

Contents

Abstract	v
1 Introduction	1
2 Experimental methods	3
2.1 Scanning Tunneling Microscopy	3
Overview...historically	3
...on 1D tunneling at a single point	3
...and how an image is created	3
Operational modes	4
Experimental details	4
theory	4
Limitations	6
2.1.1 Scanning Tunneling Spectroscopy	6
2.2 X-ray Photoelectron Spectroscopy	9
Peak shapes	11
2.3 Atomic Force Microscopy	12
3 Experimental setup and sample preparation	17
3.1 Experimental setup	17
Vacuum system	17
Cooling system	17
Damping stages	17
3.2 Substrates and ad-layers	20
3.2.1 Single crystal substrates	20
3.2.2 Dislocation lines and crystal orientation	20
3.2.3 Au(111)/Mica	21
3.2.4 Polycrystalline substrates	21
Electropolishing	21
solution of anode atoms in aqueous cell medium	22
chemical reaction	23
Removed mass from working electrode	23
Voltage-current-characteristic or polarization curve	23
gas bubbling	24
Etching solutions in literature	24
Experimental setup	25
Used solution	25
The etching process	25
3.2.5 Growing atomically thin ad layers with Chemical Vapor Deposition	28
self-limitation	28
3.2.6 Geometric effects in ad-layers	30
Periodic change in work function	31
3.3 Used molecules	32
3.3.1 Porphine: [di-[tert-butyl]-phenyl]-porphyrin derivatives	32

3.3.2	Pyrene: Pyridilethynyl functionalized pyrenes	33	
3.3.3	Helicene: Cyano functionalization of helicenes	34	
3.3.4	Coronene: HBBNC and HBC	35	
4	Epitaxial hexagonal boron nitride on copper foils	37	
4.1	Pre-treatment of Cu-foils: Polishing	37	
	Experiment realization	37	
	After etching treatment	37	
	SEM	38	
	AFM	39	
	not done yet - maybe future?	39	
	STM	39	
4.2	Characterization: SEM & STM of <i>h</i> -BN on Cu-foil	41	
	surface structure of <i>h</i> -BN on Cu-foil	41	
4.3	Characterization: XPS of self-grown <i>h</i> -BN/Cu-foils	46	
4.4	Characterization: XPS of bought <i>h</i> -BN/Cu-foils	47	
	O1s	47	
	C1s	47	
	N1s/B1s	47	
	Cu3p	49	
	An exchange of O with B or N would be easily visible in XPS (due to changed N/B surroundings. Not sure if the signal of oxygen is large enough for that. Check DATA - confirm maybe	49	
4.5	Application: Molecular functionalization with TPCN	49	
	Adding Co	51	
4.6	Conclusion	52	
5	Tert-Butyl-Phenyl Porphine	53	
5.1	Single leg functionalization	53	
5.1.1	on Cu(111)	53	
	“head-to-head”	55	
	“head-to-tail”	55	
	Flexible tert-butyl-groups	55	
5.1.2	on Ag(100)	55	
	Annealing	55	
	Assembly	56	
	Flexible Tert-Butyl-Functions	56	
	Spectroscopy	56	
5.1.3	on <i>h</i> -BN	58	
	<i>h</i> -BN grown on Cu(111)	58	
	<i>h</i> -BN grown on Cu-foil	58	
	5.1.4	Conclusion	58
5.2	Double leg functionalization	59	
5.2.1	on Cu(111)	59	
5.2.2	on Ag(100)	61	
	Unit cell	61	
	Molecular orientation	61	
	Contrast within single molecule	62	
	Domain boundaries	62	

6 Borazine functionalized coronene	65
6.1 Find a nice title!	65
HBC	71
7 Summary	73
Appendix	89
1 Crystal facets	89
2 Orbital calculations for pyrene molecules	91
How to determine molecules' distance	96
3 Python interface for a Maxigauge-TPG256A	97
4 Ordered areas of TBP	111
Ordered areas	111
TBP on Ag(100) - Symmetry relations	111
5 HBBNC	113

1 Introduction

This is the introduction..... write some! :D

2 Experimental methods

Several experimental methods are used within this work to determine different physical properties. In this chapter we review the principles, benefits and limitations for each method. All of them are well known in surface science and used to analyze thin films on different substrates with respect to their geometric, electronic and chemical properties.

2.1 Scanning Tunneling Microscopy

Overview...historically A widely used surface sensitive method is the scanning tunneling microscopy (STM). It is used to investigate as well the topography of the sample, as its electronic configuration by utilizing the quantum mechanical tunneling effect. STM has a big advantage compared to space averaging, surface sensitive techniques like XPS and LEED because it offers information in the order of atomic radii. With the help of STM the reconstructed surface of Si(111) was first discovered [1] in 1983 and described on the atomic scale. Because a wave function of an electron does not strictly end within the sample, parts of the electronic wave function spill into the surrounding vacuum. If another material (STM tip) is in close proximity, sample electrons can overcome the vacuum barrier into the tip - a process known as tunneling effect and first observed by Hund in 1926 ¹.

...on 1D tunneling at a single point Two major factors determine the tunneling current: The voltage applied between tip (grounded) and sample (bias) and the tip-sample distance. Assuming the two materials are the same and no voltage is applied, the created, time averaged current is zero because the same amount of electrons tunnel in either direction. If a bias is applied across the vacuum gap, the current in one direction becomes non-zero. The bias may be changed in polarity, causing electrons to originate from either the tip or the sample. This enables detection of occupied (negative bias) and unoccupied (positive bias) states in the sample. The distance between tip and sample influences the amount of electrons that are able to tunnel and gives rise to the resolution of geometric details in STM images. With a constant bias the current is related to the distance between tip and the (homogeneous) sample. Typical tunneling currents are in the range of nA to pA where the applied voltage may range from mV to V.

...and how an image is created The position of the tip (x , y , z) is controlled with a set of piezos (see Figure 2.1(a)). In this work a tubular piezo stack is used to control the tips position with a central piezo element located on top of the tip. The piezo length can be controlled with the voltage applied to them, which is used to choose not only the tip-sample distance, but other parameters like image size and scan speed as well. All of these parameters are monitored with the STM software. A feedback loop controls the piezo voltages. For recording an image the area is raster scanned in consecutive lines, applying a sawtooth voltage to the fast scan direction. The next lines are chosen by slowly increasing the voltage along the slow scan direction. Depending on the operating mode the tip-sample distance is controlled by piezo elements, too.

¹Hund: Zur Deutung der Molekelspektren III, Zeitschrift für Physik, Band 43, 1927, S. 805–826. Hund verwendete für Moleküle meist die Bezeichnung Molekel. Zu Hunds Entdeckung des Tunneleffekts: Rechenberg, Mehra: The historical development of quantum theory, Band 6, Teil 1, S. 535

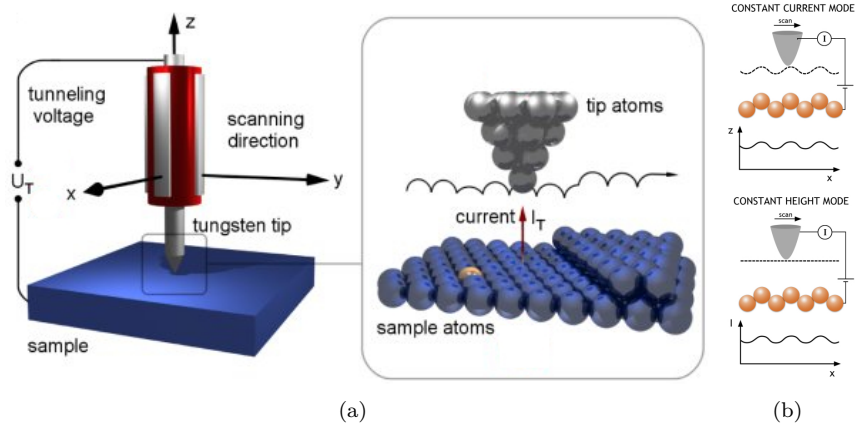


Figure 2.1: Operating principles of an STM. (a) A macroscopic sketch shows the central piezo that controls the tip position above the sample. A microscopic sketch shows the tips movement in constant current mode while moving across a atomic step edge. The main piezo is divided in four parts to control movement in the x-y plane and tip-sample distance[2]. (b) The difference between constant current and constant height mode. While the tip follows the samples LDOS in constant current mode (top) the tip height remains constant in constant height mode (bottom). Taken from [3].

Operational modes There are two common ways to operate an STM as shown in Figure 2.1(b). The **constant current mode** is the most widely used one. The tip height is regulated with a feedback controller to achieve a constant tunneling current for the chosen bias. The recorded information is now the voltage applied to the z-piezo to maintain a plane with the same current. Sample features that increase the tunneling current cause the feedback to decrease it again by retracting the tip. In **constant height mode** the tip has always the same absolute height (no feedback control), but as the tip-sample distance changes the tunneling current varies, which then is the measured quantity. To avoid crashes when the sample is very irregular, many STM's are operated in constant current mode. All STM images in this work are recorded in constant current mode. The current recorded in a certain area of the sample is translated into a contrast variation on a color scale. While some images encourage the operator to interpret points with high intensity as elevated atoms it is not that trivial. Tunneling current between tip and sample depends on the LDOS of tip and surface and is therefore not implicitly maximized at the atomic positions. It may also vary with the bias voltage applied in a non-trivial manner. Investigation of this behavior led to the establishment of a new measurement technique, called scanning tunneling spectroscopy (see subsection 2.1.1).

Experimental details Piezo-Stage:

theory While the tip (metal) is far away from the sample, their vacuum levels are the same. The corresponding Fermi energies of sample and tip lie below the vacuum level by the amount of their work functions (Φ_s and Φ_t for sample and tip respectively). Wave functions of electrons within the tip and sample decay exponentially in vacuum, depended on their energy with respect to the Fermi level. If sample and tip are in thermodynamic equilibrium, their Fermi levels are the same. Electrons now face a potential barrier (approximately rectangular) which can be overcome if their energy is high enough and the barrier sufficiently narrow. When a voltage is applied across the tunneling barrier, the energy of the tip-electrons is shifted by eV as illustrated in Figure 2.3. When a positive bias voltage is

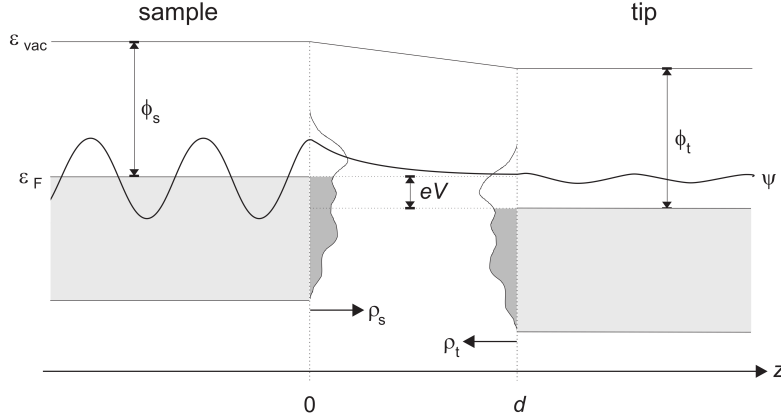


Figure 2.3: Energy diagram to visualize the tunneling process between sample (left) and tip (right) separated by a distance d . Work functions of sample and tip (Φ_s and Φ_t) separate the filled states (shaded regions) and the vacuum level (ϵ_{vac}). Since sample (ρ_s) and tip DOS (ρ_t) may not be uniform, a fictional DOS is sketched in darker colors between both. The samples energy is lifted by eV after a bias is applied and results in a net electron current from the sample into the tip. One tunneling process is indicated by a wave function in the sample. After overcoming the vacuum barrier its amplitude decreases and the corresponding electron occupies a free state (not shaded) in the tip material. Taken from [4]

applied, electrons tunnel from the tip into unoccupied states in the sample - a negative bias results in a tunneling current in opposite direction.

Following the model of Tersoff-Hamann²((1) uniform density of states in the tip, (2) temperature is low, (3) small bias voltage of some mV, (4) waveform of electrons in tip are s-waves) the tunneling current results to

$$I = 32\pi^3 \hbar^{-1} e^2 V \Phi_t^2 R^2 \kappa^{-4} e^{-2\kappa R} \rho_t(E_F) \rho_s(r_0, E_F)$$

where ρ_t is the density of states per unit volume of the tip, R the tip radius and $\rho_s(r_0, E_F)$ the Fermi level density of states in the sample[7]. The distance between tip and sample is denoted as Z and the inverse decay length of the electrons wave function is $\kappa = \frac{\sqrt{2m\Phi_t}}{\hbar}$. If I is held constant one can see that the tip in principle follows a contour of constant Fermi level density of states at the sample surface, measured at the center of the curvature of the s-wave like tip. While its a good first approximation of the system, in many cases the bias is much higher than 10mV (1V to 5V) so more than just the electrons near Fermi contribute. Also a uniform ρ_t may not be accurate in all cases.

Using Wentzel-Kramers-Brillouin (WKB) theory[8–10] the tunneling current is given by

$$I = \int_0^{eV} \rho_s(r, E) \rho_t(r, eV + E) T(E, eV, r) dE \quad (2.1)$$

where $\rho_s(\rho_t)$ is the density of states of the sample (tip) and T is the tunneling transmission probability

$$T(E, eV) = \exp \left(-\frac{2Z\sqrt{2m}}{\hbar} \sqrt{\frac{\Phi_s + \Phi_t}{2} + \frac{eV}{2} - E} \right) \quad (2.2)$$

²Please note that there are more models and corrections to them. An evolution from Bardeen’s approach to the one done by Tersoff-Hamann can be found here [5, 6] including Chen’s expansion.

If $eV < 0$ the tunneling current is largest for $E = 0$ (electrons on the Fermi-level of the sample), if $eV > 0$ the tunneling current is largest for $E = eV$ (electrons of Fermi level in tip).

Due to the fact that the tunneling current is proportional the density of states in the tip and the molecule one can deduce the band structure within a range of several volts in the vicinity of the Fermi energy.

Since states with highest energy have the largest decay lengths in vacuum, most of the tunneling current is determined by electrons within close proximity to the Fermi level.³

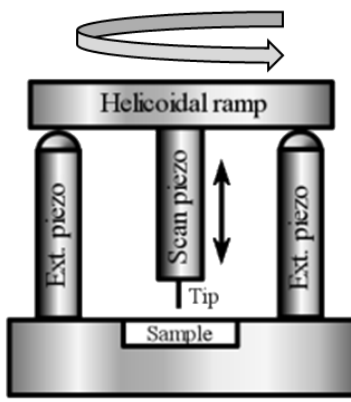


Figure 2.2: STM sample stage to control the tips position. The coarse movement is controlled by exterior piezos. Each move up/down on a heliocoidal ramp with slip-stick motion. The precise scanning is done with a central piezo to which the tip is attached. Taken from

Because STM is sensible to electronic changes, it may change the footprint of an adsorbed compound [11]. When laterally approaching an adsorbate this results in an additional tunneling current, because now electrons do not only tunnel directly into the substrate but through the adsorbate as well. Interferences between both tunneling processes depend on the adsorbate's orbital-symmetry and tip-shape. Local density of states calculations [12–14] is not adapted to grasp this effect since the tip is considered far away from the surface. Moreover, the tip radius or the tip-substrate distance is optimized to fit the lateral size of the adsorbate print with the experimental image [12, 14].

2.1.1 Scanning Tunneling Spectroscopy

First changes of the tunneling current with the bias voltage were observed by Tromp et al. in 1986 [15]. They discovered a change in contrast when scanning a Si(111) surface with either positive or negative bias. The change in contrast is most apparent in semiconductors and semi metals[7], but adsorbates and charged areas of the sample change the DOS locally and therefore the contrast in STM. While

³More information related to tunneling processes can be found here [7].

simple results may be already obtained when comparing two images recorded at different voltages, more detailed information can be achieved. At low temperatures the vanishing lateral movement of molecules makes them also accessible to tunneling spectroscopy. It is possible to deduce the electronic configuration on with atomic spatial resolution.

Spectroscopic information (information on the DOS) can be obtained by either changing the bias voltage ($I(V,z)$ -spectroscopy) or the tip-sample distance ($V(z)$ -spectroscopy).

Therefore the bias is modulated with a sinus like waveform. The frequency of the low amplitude modulation of the DC bias is much larger than the feedback loop frequency (1 kHz to 2 kHz). The AC part of the tunneling signal is than recorded with a lock in amplifier. The in-phase component is directly the $dI/dV|_{V=V_{bias}}$, recorded simultaneously with the topography.⁴

First let us consider small biases. If tunneling conditions are such that $eV \leq \Phi$, observed features in dI/dV are associated with the surface DOS. Critical points in the surface projected DOS give rise to features in dI/dV . Interpretation of these features with the WKB theory (i.e. differentiating equation (2.1)) gives

$$dI/dV = \rho_s(r, eV)\rho_t(r, 0)T(\mathbf{eV}, eV, r) + \int_0^{eV} \rho_s(eV)\rho_t(r, E - eV) \frac{dT(E, eV, r)}{dV} dE$$

The first term contains the DOS of the sample and tip and the transmission function. While it is usually unknown, a closer look to (2.2) indicates a smooth, monotonically increasing function in V. This mannered dependence on V gives a smooth background described by the second term $\int_0^{eV} \rho_s(eV)\rho_t(r, E - eV) \frac{dT(E, eV, r)}{dV} dE$. Because T is smooth and monotonic the first term $\rho_s(r, eV)\rho_t(r, 0)T(eV, eV, r)$ introduces the dependence on the DOS in the sample for energies eV - our desired spectrum.

If dI/dV is recorded simultaneously with the topography, another contribution arises. One usually observes an decrease in atomic corrugation when the distance between tip and sample is increased. The surface looks flat. To have the same tunneling current on atom positions and in between, the decay length in the valleys κ_v must be larger than on the atom positions κ_a . The Z-depended corrugation given by Tersoff-Hamann is

$$\Delta(Z) \approx \frac{2}{\kappa} e^{-\frac{\pi^2 Z}{a^2 \kappa}}$$

where a is the lattice constant and κ the inverse decay length. To make both a flat looking surface one gets the expression

$$\kappa_v = \kappa_a - \frac{2\pi^2}{ka^2} e^{-\frac{\pi^2 Z}{a^2 \kappa}}$$

As the transmission factor changes with the decay length, the tunneling current and with it the dI/dV changes. This is the origin of topographic features in dI/dV maps when recorded at constant current.

The origin of the strongly voltage depended background can be found in WKB theory as well. When writing the tunneling current as

$$I = \int_0^{eV} \rho_s(r, E)\rho_t(r, eV + E) \exp\left(-\frac{2Z\sqrt{2m}}{\hbar} \sqrt{\frac{\Phi_s + \Phi_t}{2} + \frac{eV}{2} - E}\right) dE$$

the tunneling current reduces to

$$\bar{I} = \rho_s \rho_t \bar{V} \exp\left(-\frac{2\sqrt{2m}}{\hbar} \sqrt{\Phi} Z\right) \quad (2.3)$$

⁴If the modulation frequency is too low, the feedback tries to compensate the modulation by changing the distance to the sample. If the modulation frequency is too high, the capacitance between tip and sample leads to an 90 deg phase shifted current which increases with modulation frequency. One usually chooses the modulation frequency slightly above the cutoff frequency for the feedback loop.

Assuming that DOS of tip and sample ρ_t/ρ_s are constant, as well as discarding the change of the tunneling barrier with the bias voltage(an assumption only valid for very small voltages with $eV \ll \Phi$) the derivative of (2.3) is given by

$$\frac{dI}{dV} = e\rho_s \rho_t \exp\left(-\frac{\mathbf{2}\sqrt{2m}}{\hbar} \sqrt{\Phi - \frac{eV}{2}}\right) Z$$

Substituting Z with the one obtained by (2.3) leads to $dI/dV = \bar{I}/\bar{V}$ - which diverges as $1/V$ when going to very low bias voltages and gives another contribution to the background. This makes it hard to observe features in close proximity to the fermi level ($V_{bias} = 0$ V). This background can be reduced when operating at constant tunneling resistance and not at constant current. When doing this, features usually obscured by the $1/V$ diverging background can be observed.⁵

If the bias voltage is higher than the work function of the sample dI/dV reflects mainly states that arise from interaction of electrons at the surface with the polarization they induce in the bulk. Electrons are trapped by this interaction in a region near the surface leaving their lateral movement undistorted. These waves either do interfere con- or deconstructively at the surface. Which type of interference occurs is determined by the applied bias voltage that alternates the bounding condition. The transmission alternates when going from constructive to destructive interference and therefore the tunneling current changes when changing V. As an interesting fact, Becker et al.[17] found that that numerical integration of Schrödinger's equation could be used together with dI/dV spectra to calculate the absolute distance between tip and sample - an value hard to come by with other methods.

Further information can be drawn from the tunneling system when the barrier height may be determined. Taking the limit of the transmission function (2.2) for low bias voltage ($eV \approx 0$, $E = E_F$) results in

$$T = \exp\left(-\frac{\mathbf{2}Z\sqrt{2m}}{\hbar} \sqrt{\frac{\Phi_s + \Phi_t}{2}}\right)$$

Using this in the WKB approximation (2.1), one gets

$$\frac{dI/dZ}{I} = \frac{\mathbf{2}\sqrt{2m}}{\hbar} \sqrt{\Phi_s + \Phi_t}$$

As the work function of the tip usually stays constant, lateral variations in the barrier height can be boiled down to local changes in the work function. This is done by [18].

Determining the barrier height in this way often results in to low values for the work function. Discussion of this is found in [7, p. 96].

Up to now only rectangular tunneling barriers were considered. Already in 1966 Gundlach was the first who calculated transmission currents for trapezoidal potential barriers [19]. The oscillations named after him are due to standing wave states in the potential tip-sample potential barrier [17, 20]

"When the Fermi level of the tip is close to the vacuum level of the sample, the contribution of the image potential is significant. The superposition of the image potential and the electrostatic potential forms a specific potential well, and the lowest-order peak is a Gundlach oscillation related to a standing-wave state in this well. When the Fermi level of the tip is higher than the vacuum level of the sample, the image potential becomes negligible, and the potential well can be approximated by a triangular shape. Those peaks beyond the lowest-order peak are the Gundlach oscillations related to the standing-wave states in the triangular well. Derivation based on quantum mechanics shows that the energy difference of the standing-wave states in the triangular well is proportional to $F^{2/3}$, where F is the electric field in the tip-sample gap"[21]

⁵A comprehensive overview on measurement technique and analysis can be found in [7]. For information on normalization of STS and to reduce the background close to E_F , see [16].

The resolution of STS is determined by the range of energies electrons have when contributing to the tunneling process. When $T > 0$ the DOS is smeared out and described by the Fermi-Dirac statistic[22, 23]

$$f(E) = \frac{1}{1 + \exp\left(\frac{E - E_F}{k_B T}\right)}$$

Since electrons from occupied states (DOS is Fermi distributed) tunnel into unoccupied states the transmission function has the structure

$$T(E, eV, T) = T(E, eV)f(E)[1 - f(eV - E)]$$

When looking at the shape of the Fermi-Dirac distribution one can see that most of the electrons participating in the tunneling process arise from a rather narrow area around the Fermi level of the negatively biased electrode (broadening of fermi edge at $T = 300K \hat{=} 0.026$ eV). Electron distribution of tip and sample are broadened by $2k_b T = 0.054$ eV thus the energetic range where electrons may come from is 0.1 eV. From the uncertainty relation $\Delta x \Delta k \geq 1/2$ and the dispersion relation for metals follows

$$\Delta E \geq \frac{\hbar^2 k_F}{2M^* \Delta x} = 0.47 \frac{E_F - E_0}{r k_F}$$

[24]. “The asymmetric form of $T(E, eV)$, with the sharp increase at E_F , helps to make the effective resolution of the STM somewhat higher when probing empty states of the sample than when probing filled states.” The resolution at room temperature is estimated to be 140 m eV[25]. As the tunneling transmission is always a factor of the tip and sample DOS, STS is always limited to the unknown electronic structure of the tip. While geometry at the tip apex is successfully enhanced with field evaporation techniques its electronic structure may differ greatly from the bulk one due to unusual bonding geometry and small size.⁶

2.2 X-ray Photoelectron Spectroscopy

XPS is a tool to achieve information of the samples chemical structure. Most of the information given here is taken from [30] in [31]. When X-rays with sufficient energy hit metals, electrons are emitted. This effect is called photoelectric effect and was first discovered by Heinrich Hertz in 1887 through the fact that electrodes illuminated with ultraviolet light create electric sparks more easily[32]. 18 years later Albert Einstein received the Nobel Price for his discovery of the law of the photoelectric effect[33] and a scientific explanation which Hertz was missing.

The standard X-ray source is supplied with aluminum and magnesium anodes. Other materials are available that produce various X-ray energies and line widths [34].

As the X-rays hit and penetrate the sample surface they excite electrons and initiate different processes. The meajor two are discussed in the following.

For the **simple core-level excitation** the X-ray removes a single electron next to the core which is then detected. Energy conservation due to elastic scattering of the electron out of the bulk results in the relation

$$E_{kin} = h\nu_{X-ray} - E_B - \Phi_{bulk} \quad (2.4)$$

$$E_B = h\nu_{X-ray} - E_{kin} - \Phi_{bulk} \quad (2.5)$$

$h\nu_{X-ray}$ is the energy of the incident X-ray beam, E_B the binding energy of the excited electron and Φ_{bulk} the work function of the analyzer.

⁶ Some[26–29] groups have calculated band structures for different tip geometries and their influence on the tunneling process.

Table 2.1: Energy and line widths of available anode materials. Taken from

Anode	Radiation	Photon Energy (eV)	Line Width (eV)
Mg	K α	1253.6	0.7
Al	K α	1486.6	0.85
Zr	L α	2042.4	1.6
Ag	L α	2984.3	2.6
Ti	K α	4510.9	2.0
Cr	K α	5417	2.1

In the **Auger process** on the other hand the created core level (lets say at level K) vacancy is filled with a energetically higher lying electron (at for example level L_1). The excess energy can either be radiated away (X-ray fluorescence) or given to an electron in the same or in a more shallow level (lets say $L_{2,3}$). This electron then can leave the sample as Auger electron. Figure 2.4(b) shows the mentioned process.

Due to the fact that this process has two stages these electrons are referred to as secondary electrons. The notation for this process is $KL_1L_{2,3}$. The electron taking part in the Auger process can also originate from within the valence band ($KL_{2,3}V$) or even both electrons may stem from the valence band (KVV). For every element there is a unique series of Auger excitations. This holds even if one or even both electrons come from a valence band, as the dominating term will always be the binding energy E_K . As the Auger energy

$$E_{KL_1L_{2,3}} = E_K - E_{L_1} - E_{L_{2,3}}$$

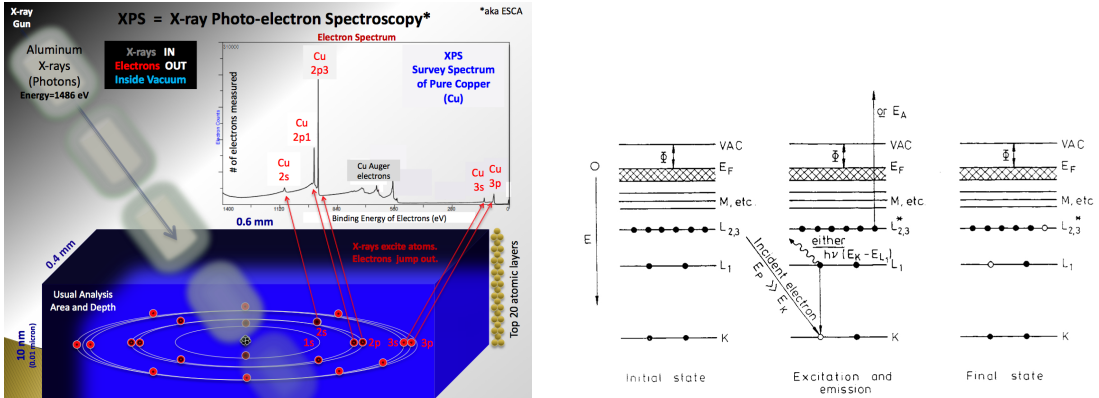
is not a function of the excitation energy it will not shift when changing the X-ray energy. Even very heavy elements (as the number of atomic levels the possible Auger transitions increases) do not exhibit a very large number of Auger emission lines due to the fact that the transition probability favors only a few of this many. [35]

[36] The chemical surrounding of atoms changes their binding energy, making XPS an ideal tool to detect changes in chemical surrounding. Although the analysis is averaged over the area of the incident X-rays (typically profiliate of microns up to several mm) its results are very precise. This makes it possible to distinguish differently bound atoms within single atomic species and therefore gives rise to otherwise not directly observable processes like growth, intercalation, etching and binding of for example graphene islands on Ir(111)[37, 38]. XPS is used to identify oxidation processes of copper surfaces as the interaction of oxygen with the copper surface changes the Cu core level. [39].

With the use of aluminum X-ray sources, electrons are accelerated with typically 15 keV onto the target. Most of the created radiation goes into the principal characteristic line ($K\alpha_{1,2}$). Higher ones ($K\alpha_{3,4}$, $K\beta$) are also observed but with much lower intensities. In addition there is a continuous background called Bremsstrahlung extending up to the energy of the incident electron energy. This background is of no use for the XPS measurement and has to be subtracted in a more or less artificial way.

For the ease of analysis, many spectra are recorded with monochromatic radiation. This selects a certain energy for the following illumination of the sample. This technique relies on the dispersion of X-rays within a crystal. It is described by the Bragg relation $n\lambda = 2d \sin(\theta)$ where n is the diffraction order, λ the wavelength of monochromatic radiation, d the distance between two crystal layers and θ is the so called Bragg angle. The first order peak for Al $K\alpha$ radiation ($\lambda = 0.83$ nm, $E = 1486.6$ eV) is at $\theta = 78.5^\circ$ (using the $10\bar{1}0$ planes of a quartz crystal with $d = 0.425$ nm). Therefore the angle between incident and reflected beam is about 23° .[30]

The spectra used in this work are recorded without monochromatic radiation as not stated otherwise. This is because the electron intensity is attenuated when using a monochromatic source.



(a) Representation of XPS process. X-rays are used to excite core level electrons. After leaving the sample these show element specific signatures in their kinetic energies. A detailed analysis of the peak shape and shift allows for identification of the chemical environment.

(b) Two step Auger process. In contrast to a direct emission of a core electron, the Auger emission involves more electrons from less bound states. Here an (L_1) electron fills the hole in the K shell created by the initial X-ray. The resulting hole in the L_1 shell is then filled with an $L_{2,3}$ electron resulting in a typical Auger emission feature. Adopted from [35].

Figure 2.4: XPS and Auger processes present after irradiation of the sample with X-rays. Two simultaneous processes occur. 2.4(a) shows a scheme of an X-ray gun illuminating a sample area of about 0.4 mm x 0.6 mm. Excited electrons within the first 20 layer escape the sample and are analyzed for their kinetic energy. Core electrons and Auger electrons are excited at the same time resulting in a chemical fingerprint of the sample.

The binding energies of some often observed peaks are given in table 2.2

Peak shapes The shape of the peaks typically resembles the line shape of the used X-rays (Gauss width $\approx 1\text{eV}$). In case of s-states ($l = 0$) (B1s, N1s, C1s) the peaks are singlets. With increasing $j = l + s$, the spin-orbit ($j-j$) coupling introduces a 'parallel' and 'anti-parallel' nature of the spin, resulting in two different $j = 1/2(3/2)$ and therefore two different energies. The split in energy is expected to increase as Z increases (for constant n,l) or as l decreases (n constant). This makes the splitting of 3p orbitals larger than that of the 3d's. The ratio of the two peaks is given by their degeneracy ($2j + 1$).[30, p. 113]

The more atoms of a specific kind are present, the larger the signal gets. Therefore the signal intensity resembles the amount of atoms on the topmost surface layers ($\approx 10\text{ nm}$).

As each irradiated atomic species has a different cross section for adsorption of X-rays with a certain energy they emit auger and core level spectra with a different intensity. Comparing the cross section of e.g. N with B's, one can see that it is roughly 3 times to 4 times as large (B: $6.87 \times 10^3 \text{ b/atom}$, N: $25.82 \times 10^3 \text{ b/atom}$ for AlK_α)[41]. Meaning that the signal from the N is much stronger than that of the B, although their number of atoms is equal.

A calibrated XPS is capable of measuring the surface coverage of an ad-layer (e.g. BN) compared to the bulk of the sample. Calibration works as follows:

- A perfect, full layer of a known material (e.g. C) is prepared (graphene)
- The known cross section for C ($6.87 \times 10^3 \text{ b/atom}$)[41] relates the signal to the number of atoms in the full layer.
- One then has to divide the signal of the unknown coverage (of known material) by the cross

Table 2.2: Element specific transitions and binding energies for some chosen elements as reported in [40]

Element	excited state	E_B [eV]
O	1s	531
N	1s	398.1
C	1s	285
B	1s	189.4
Cu	2p $\frac{1}{2}$ ($\frac{3}{2}$)	953 (933)
Cu	LMM	560-580
Cu	3s	123
Cu	3p $\frac{1}{2}$ ($\frac{3}{2}$)	77 (75)

Table 2.3: Spin-orbit splitting parameters. Ratios are reproduced from [30]

Subshell	j values	Area ratio
s	$\frac{1}{2}$	—
p	$\frac{1}{2}, \frac{3}{2}$	1:2
d	$\frac{3}{2}, \frac{5}{2}$	2:3
f	$\frac{5}{2}, \frac{7}{2}$	3:4

section (of C) and directly receives the coverage. Keep in mind that the X-ray penetration depth (and with it the signal of the substrate) stays only constant if the illumination angle stays constant. Even small angular variations may change the signal.

Referring to [42] the fraction θ_A of an adsorbate A on a surface B can be calculated via

$$\theta_A = \frac{I_A I_B^0 \cdot \exp(\frac{a_A}{\lambda_A} \cos(\Theta))}{I_A I_B^0 (\exp(\frac{a_A}{\lambda_A} \cos(\Theta)) - 1) + I_B I_A^0 \cdot \exp(\frac{a_A}{\lambda_A} \cos(\Theta))} \quad (2.6)$$

where the parameters are given in table 2.4.

Table 2.4: Description of parameters used in equation 2.6

Parameter	Annotation
I_A	integrated intensity of the adsorbate peak
I_A^0	cross section of element A
λ_A	mean free path of electrons in material A
a_A	thickness of adlayer

The mean free path of electrons with energy E in a solid is given by $\lambda_M = 0.41 \cdot a_M^{0.41} \cdot E_M^{0.5}$ where a_M is the atomic size of M.

2.3 Atomic Force Microscopy

Introducing STM as a electronically sensitive method to investigate surfaces, the atomic force microscopy interacts in a different way with the sample. To scan the surface of the sample, one uses a small tip (cantilever) to interact with it. Due to its small distance different kinds of forces occur. The force induced movement of the tip is then interpreted and information about the surface may be derived. The layout of a typical consists of the cantilever itself and some kind of tip-position measurement.

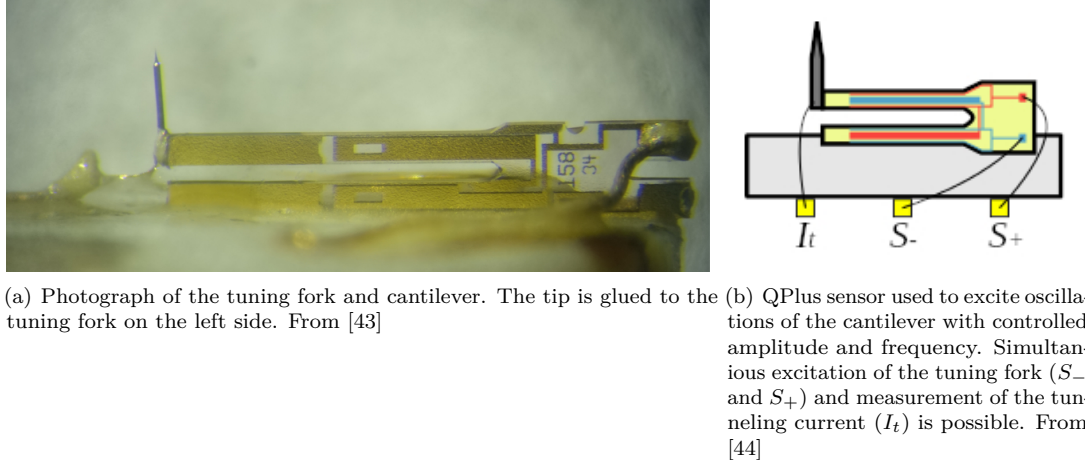


Figure 2.5: Photograph (a) and sketch (b) of AFM cantilever as used in the used setup.

Earlier are made of the position-sensitive detector (PSD) consisting of two closely spaced photo diodes whose output signal is collected by a differential amplifier. Todays AFMs feature a Q-Plus sensor, as shown in Figure 2.5(b). Here the tip is positioned on top of an oscillating fork that is operated close to its resonance frequency. If the tip interacts with the sample, its oscillations is hindered and the frequency of the oscillation shifts. From this shift in frequency one can estimate the strength of the acting force. Since every type of adsorbate atom acts in different ways with the tip, AFM is element specific. A magnetic tip can be used to scan for magnetic forces on the sample surface. With an added wire to the AFM tip, simultaneous AFM and STM measurements are possible.

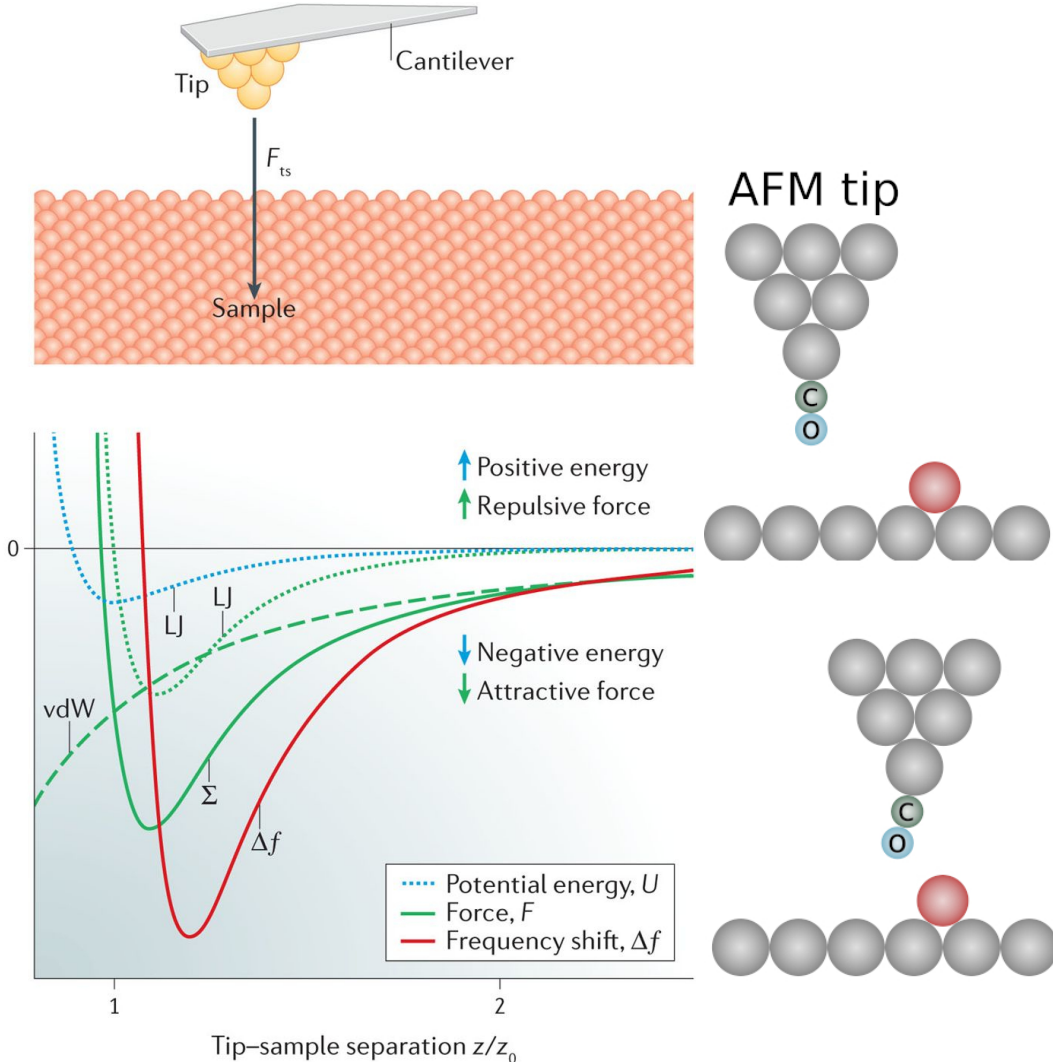
Types of forces are typically:

- Van-der-waals interaction (always attractive)
- Mechanical contact force (always repulsive)
- Capillary forces, chemical bonding, electrostatic forces, Casimir forces, solvation forces and others

The typical resulting force between tip and sample is artistically shown in Figure 2.6(a). On the top part a cantilever with an atomic tip is shown on top of the sample surface. The interaction forces F_{ts} act between tip and sample and are indicated by an arrow. In the lower part a representation of the resulting force in dependence of the tip-sample distance is shown. Although many different forces may act, the resulting potential is often modeled with a Lennard-Jones-Potential LJ [46]. Two of these are plotted with green and blue dots. The acting vdW force is plotted in dashed green. The sum of the acting forces is labeled \sum . A typical frequency shift Δf is given as red graph. One can distinguish different regimes as indicated by the arrows. When tip and sample are in considerable distance to each other, the attractive vdW forces are the dominant part in the sum. While the tip approaches the sample, more and more interactions with the surface and adsorbate add to this force, strengthening F_{ts} . When the separation reaches z_0 , the distance becomes so small that repulsive forces overcome the attractive one - entering the repulsive regime shortly afterwards. The best images were recorded close to the onset where F_{ts}

There are several operational modes to drive an AFM:

1. **Contact (static) mode:** The cantilever is operated in contact with the sample surface. At very close proximity, repulsive forces are stronger than the attracting ones. The signal used to



(a) Schematic representation of cantilever tip and atomically flat sample surface. The force between both F_{TS} is indicated with an arrow. The attractive/repulsive force regimes are shown for varying tip-sample distances. From [45]

(b) Enlarged scheme of AFM tip and top most sample layer with single adsorbate atom. CO functionalization of the metallic AFM tip is shown in (b). The CO functionalization of the tip leads to an decreased tip apex that increases resolution. Modified from[44].

Figure 2.6: Basic function of a typical Q-plus AFM sensor. (a) Sketch of tip-sample interaction together with force-distance graph. The CO functionalization of the metallic AFM tip is shown in (b)

gain information on the sample is either the feedback loop to keep the tip at the same absolute position or directly the deflection of the cantilever.

2. **Intermittend contact mode (tapping) mode:** While the contact mode has some disadvantages when scanning samples with an adsorbat layer (tip sticks to surface when close enough to measure short-range forces) another mode has established. Hereby the tip oscillates with amplitudes in the 100 nm to 200 nm regime and is not dragged the whole way across the sample. The intermittent forces acting on the tip when reaching the sample are measured. The change in amplitude when in close vicinity to the surface is a sign of the actual height.
 3. **Non-contact mode:** The cantilever is driven at its resonance frequency with amplitudes smaller than 10 nm and at a certain distance to the sample. Long-range forces like van-der-waals and others change the resonance frequency of the cantilever. This change is a indication of the acting force between cantilever and sample. This mode is used within the scope of this work.
- AFM produces a true height-profile of the sample (and not a mix of electronic and geometric information projected onto a 2D-map like in STM)
 - It has limited resolution especially when scanning features steeper than the tip apex

Its advantages are the comparable large image size of many hundred nm compared to only some dozen nm in the case of STM. Scan speeds are typically some orders of magnitude larger than those in STM so that image acquisition is much faster.

To increase the resolution the tip can be functionalized with CO (see figure 2.6(b)). This method is widely used⁷ to investigate not only geometric features that are not accessible in STM, but also chemical differences on the sample[wang_exploration_20170].

⁷Only a few examples from the recent years can be found here [45, 47–52]

3 Experimental setup and sample preparation

To conduct experiments in the most controlled environment possible, sample preparation is done in ultrahigh vacuum (UHV) chambers. With a base pressure of $\approx 5 \times 10^{-10}$ mbar these stainless steel chambers are almost free of contaminants. After cleaning the metallic substrates, ad-layers and molecular species are deposited and investigated. Experiments were done at different experimental chambers: (1) A LT-STM chamber. The technical aspects of the preparation and experimental chamber are discussed elsewhere [53–55] and shortly summarized here. (2) A RT-STM with XPS capabilities. The technical aspects and build details are given in [54]. (3) The NIM-XPS chamber. (4) A LT-AFM machine offers a complementary investigation method for geometric information. Its setup details can be found in [43].

3.1 Experimental setup

Since all used UHV chambers have many common part, a typical setup is described with the LT-STM setup. Here the most experiments were carried out.

Vacuum system

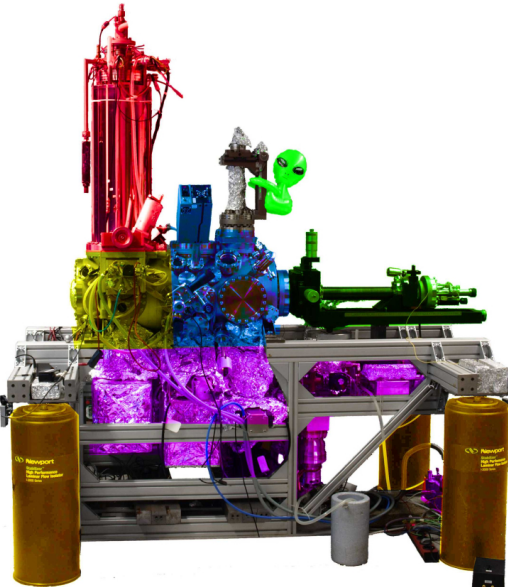
Cooling system While low temperature (LT) STMs may be operated with solely helium, it is more resource-saving to cool the direct proximity of the sample and the STM with He, but to suppress the heat flow out of the He-cryostat with a second surrounding nitrogen cryostat (boiling point: 77K, compare figure 3.1(b)). This diminishes consumption of globally limited and rather expensive He. To maintain a temperature of 5K to 7K, one to two liters of liquid helium are required a day, plus an additional amount of three to four liters liquid nitrogen. Evaporated helium is reclaimed in a closed circuit with a system of purifying and storage/cooling steps so that only a small amount of helium escapes the circuit and is lost.

Sample temperatures down to 5K to 7K allow for observations not possible at elevated (room) temperature. Cooling not only reduces thermal drift in the piezo elements that are used to control the tip's position on the sample. Thermal energy at low temperature is not high enough for atoms or molecules to move on most substrates. Species mobile at room temperature (and therefore not representable at room temperature in the sub-ML regime) become immobile and accessible for ST microscopy and spectroscopy. STS spectra resolution is better at low temperatures as discussed in 6.

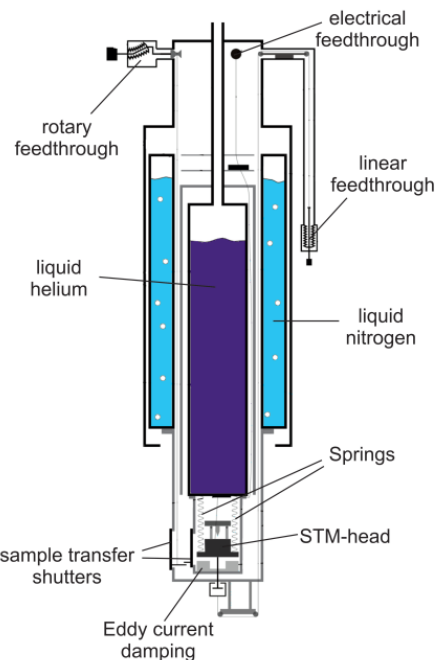
Damping stages Two damping stages are used, one for the chamber and a separate one for the STM.

- The whole UHV system is placed on air pressurized legs. These can be elevated on demand, so that the chamber floats on four dampers and external vibrations/shocks are damped.
- A second stage decouples the sensitive STM from the rest of the setup. First the complete STM stage hangs on springs to further limit the direct influence of vibrations. Second the remaining oscillation amplitude is damped by a eddy current damping. It is made of three magnets in close proximity to the surrounding support so that eddy currents are induced for each minute movement. The eddy current is typically larger at cryogenic temperatures, that results in a damping that works best at low temperatures. The kinetic energy of the oscillating system is

transferred by the eddy currents into heat within the surrounding conductor. The heat is then mitigated by the external cooling of the cryostat.



(a) LT-STM setup mainly used in this work. Different functional groups are colored in different colors. A low base pressure is achieved with a combined pumping system comprised of ion pumps and turbo molecular pumps (cyan). The liquid helium/nitrogen bath cryostat (red) is used to maintain low temperatures. Sample holders are operated with a rote able, variable temperature manipulator. Sample preparation is done in a chamber (blue). After transfer to the LT-STM chamber (yellow) a gate valve is used to seal the LT-STM from remaining residual gas that may be present in the preparation chamber. Vibration isolation of the frame is achieved with legs floating on pressurized cylinders.



(b) Scheme of a STM liquid bath cryostat. While in the inner measurement stage a temperature of $\approx 5\text{ K}$ to 7 K is achieved with a liquid helium reservoir, an outer liquid nitrogen cryostat is used to isolate the evacuated inner cryostat from the surrounding room temperature.

Figure 3.1: Typical setup for low temperature measurements. A vibration isolated UHV chamber is used to prepare samples and investigate them in a separable chamber with either STM or AFM. A liquid bath cryostat is used to maintain low temperatures. Images stem from diss-knud

3.2 Substrates and ad-layers

Molecular adsorption experiments are done with single crystalline substrates of copper and silver, terminated at (111) and (100) surfaces. Polycrystalline copper foils and gold evaporated on mica are used as well. Some experiments are done to investigate molecules on *h*-BN/Cu(111) and *h*-BN/Cu(foil).

The following sections will describe the relevant physical properties of the various substrates and will introduce a method to prepare polycrystalline copper foils to grow *h*-BN on. An example for chemical vapor deposition of borazine on a transition metal surface is given. The geometric properties of the resulting lattice mismatched system are discussed briefly. The molecules used for experiments are introduced at the end of the chapter.

3.2.1 Single crystal substrates

Single crystals show a nicely ordered, clean surface - two properties important for reliable and reproducible experiments. We have chosen both silver and copper as bulk crystalline substrates. Both form fcc lattices and their surface termination can be chosen by precise cutting along a symmetry plane of choice. For the course of this thesis, experiments are conducted mainly on (111) and (100) terminated surfaces.¹ Commercially available, single crystals guarantee a high precision in facet orientation and purity (99.999 %) [57]. Remaining contaminations in copper (Ag: 0.8 ppm, Pb: 0.3 ppm, Bi: 0.8 ppm) and silver (Cu: 2 ppm, Fe: 2 ppm, Au: 0.8 ppm, Ni: 0.8 ppm) are removed by repeated sputter² and anneal cycles³ in UHV. Typical cool down temperatures $\leq 5 \frac{K}{s}$ result in a smooth, atomically flat surface with large terrace size.

The lattice constants at room temperatures for cite! Cu(3.61 Å), Ag(4.09 Å) and Au(4.07 Å) are related to the environment temperatures by their expansion coefficients. Coefficients of $16.5 \times 10^{-6} \text{ K}^{-1}$ (Cu), $18.9 \times 10^{-6} \text{ K}^{-1}$ (Ag) and $14.2 \times 10^{-6} \text{ K}^{-1}$ (Au) make the substrate lattice shrink by $\approx 0.5\%$ when it is cooled down from RT to low temperature measurement conditions in STM/AFM (5 K to 7 K). While rather negligible for bulk materials that are not heated and cooled over larger temperature ranges, the small change in substrate lattice size may introduce strain in grown ad layers since these are grown via CVD typically at elevated temperatures and may have partially negative thermal expansion coefficients[58].

The surface free energy increases from the (111) surface with increasing angle of the (hkl) planes of interest with

$$\cos(\phi) = \frac{h + k + l}{\sqrt{3(h^2 + k^2 + l^2)}}$$

[59]. Thus, the (111) surface is the one with lowest energy, followed by (110) and (100).

3.2.2 Dislocation lines and crystal orientation

Due to the fact, that dislocation lines move within the crystal in a well defined manner, one can determine the crystals orientation when the orientation of a dislocation is known. For fcc crystals the orientation of dislocation lines occurs in the 111 plane in <110> direction. Its Burgers vector is $\frac{a}{2}[110]$ [60]. ADD INFO FOR 100!!!

Dense packed rows in fcc(111) are the following directions: < $\bar{1}01$ >, < $01\bar{1}$ >, < $1\bar{1}0$ >. The diagonals are found in the < $\bar{1}\bar{1}2$ > and < $1\bar{2}1$ > directions. ADD INFO FOR 100!!!

¹See [56] and appendix section 1 Crystal facets for another examples of vicinal metal surfaces (531), (532), (221), (311), (211).

² $U_{\text{accel}} = 800 \text{ V to } 1000 \text{ V}$, $T_{\text{sample}} \approx 300 \text{ K}$

³Cu: $T_{\text{sample}} = 750^\circ\text{C}$, Ag: $T_{\text{sample}} = 450^\circ\text{C}$, AuMica: $T_{\text{sample}} = \underline{\text{get value: 450?}}$

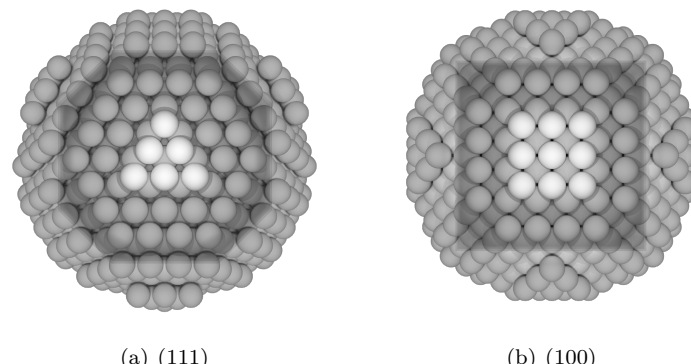


Figure 3.2: Identical crystalline balls in fcc lattice configuration. The surface termination is determined by the direction of the intersecting plane (parallel to the paper plane) relative to the lattice.

3.2.3 Au(111)/Mica

Au(111) substrates can be used either as single crystal or as thin evaporated layers on Mica. Here only the uppermost crystal layers (≈ 150 nm) are gold that is supported by a mica substrate. Au(111) is known to reconstruct its surface to a herringbone shaped $2\bar{2} \times \sqrt{3}$ [61]. This leads to the surface atoms being divided in regions with different registry (fcc/hcp) to the "bulk" atoms. When imaged in STM, these regions can be distinguished by their width, where fcc regions are wider than hcp regions which are separated by lines of higher lying, thus bright appearing, surface atoms. The two different surface terminations lead to chemically differing substrate regions, leading to a site-preferring adsorption of atoms and molecules [62, 63].

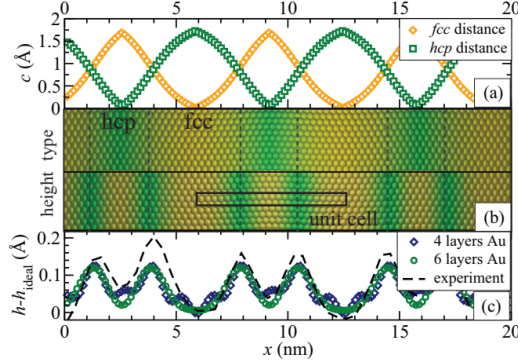
3.2.4 Polycrystalline substrates

As was mentioned before, clean, highly ordered surfaces are desirable to perform experiments on. Effort is done to clean the surfaces before every experiment to ensure a reproducible environment and interpretable results. This lead to a detailed understanding of the physics and chemistry behind a lot of systems. In case a systems order and functionality does not heavily depend on the substrates symmetry, single crystals loose most of their unique selling point. Instead of choosing a expensive bulk single crystal, thin copper foils can catch up in production environments. The mass produced foils still show some inconvenient properties. Although pure copper foils ($\geq 99.999\%$) are available, their surface was never meant to be atomically flat. A representation of a copper surface before electro polishing can be seen in figure 3.3. Here the layered structure of the (mechanically polished) foil is apparent and shows different sizes of grains and annealing twins at the surface. Small subgrains constitute the uppermost layers, while deeper lying layers consist of larger grains with grain boundaries becoming more and more diffuse with increasing distance to the surface.

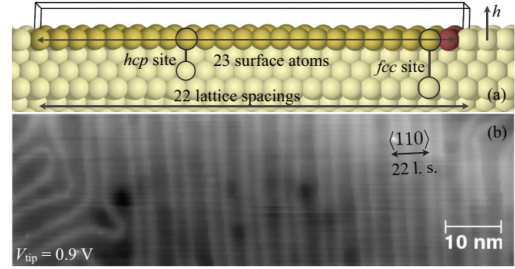
The surface termination is not homogeneous and is made of several domains with different facet orientation thus showing different step heights as indicated in table 1.

Electropolishing

But growing high quality ad-layers on polycrystalline copper foils requires a smooth surface. As-ordered Cu foils exhibit a root-mean-square (RMS) surface roughness of about 218 nm[65]. Striations - a fabrication remnant due to the cold rolled foils - are observed on the surface[66]. Also some



(a) Calculated structure of the reconstructed Au(111) surface, using the vdWDF/PBE density functional. (a) Site character c : distance from the ideal fcc and hcp site for each atom in the top layer, as discussed in the text. (b) Structure of the top layer. The color coding in the top half denotes the atom type, with yellow atoms being of fcc and green atoms being of hcp type. On the bottom half, the color indicates atomic height, with yellow atoms being the closest to the ideal fcc lattice continuation from below. (c) Calculated top-layer height with respect to the ideal fcc lattice and an experimental line scan.



(b) Schematic representation of the Au(111)/ $22 \times \sqrt{3}$ reconstruction, showing how 23 surface atoms fit into 22 lattice sites by compressing the top layer of the surface with the additional atoms colored dark red. The positions corresponding to lined-up fcc and hcp sites are indicated by the vertical lines. STM image of the Au(111) herringbone reconstruction ($V_{tip} = 0.9\text{eV}$, $I_{set} = 1\text{nA}$).

manufacturers apply a thin layer of chromium oxide for corrosion protection[65]. A common procedure to reduce the roughness of a material is to electrochemical polish the surface.

A comprehensive overview of electrochemical polishing of Cu surfaces with different etchants can be found in [67]. The following gives a short introduction in chemical polishing as used for preparation of thin copper foils.⁴

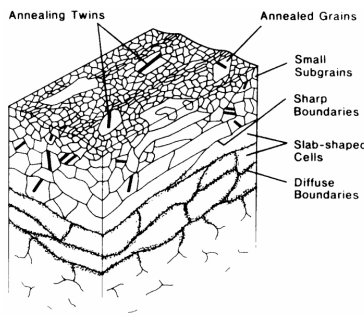


Figure 3.3: Proposed bulk structure of a OFHC copper foil after abrasion with P1200 silicon carbide paper. Adopted from [64]

solution of anode atoms in aqueous cell medium Electrons and atoms at the solid surface have higher energy states. Thus some of the atoms on the metal surface may lose electrons to form ions. These ions may also recombine with electrons and become atoms at another moment. Depending on the electronic structures, some metals (such as sodium) are easier than others (such as platinum) to ionize. Copper is relatively stable. Still, some of the surface atoms may be expected to ionize at a moment. The ionization process may be promoted when the metal is in touch with aqueous solution because:

- Metal ions can not move in the metal electrode but can move through the solution, producing electric current in solution with an applied potential
- Electrons can move freely in metal solid (electric current in a metal) but can not survive in solution and will quickly recombine with positive ions

⁴For a broader view on the topic, the reader is pointed to references [68–70].

- Water dipoles and negative ions in solution may drag the surface metal ions into the solution

chemical reaction “The electrode connected to the positive pole of the power supply is called anode. And the one connected to the negative pole of the power supply is called cathode. When the applied voltage is high enough, electrons in the anode may be pumped out and the metal atoms on the anode surface will be oxidized (e.g., $Cu - 2e = Cu^{2+}$) and dissolved into the electrolyte solution. Under electrical field, the positive ions (cations) move towards cathode and negative ions (anions) move towards anode. The cations may get electrons and be reduced to neutral atoms (e.g., $Cu^{2-} + 2e = Cu$) again at the cathode surface. Therefore, charge transfer between the two electrodes is carried out via the ion drift in the electrolyte and electron conduction in metal wire. When the working electrode is set to be anode, dissolution is processed at certain potential. Likewise, when the working electrode is set to be cathode, it can result in deposition. For electropolishing of copper, the copper part to be polished is set to be anode while the cathode can be any conductive material (e.g., copper).

The critical potential at which the oxidation / reduction starts to occur is related to the standard redox potential for a specific anode material. The redox potential E_O is a measure (in volts) of the affinity of a substance for electrons - its electronegativity - compared with hydrogen (which is set at 0). Substances more strongly electronegative (i.e., capable of oxidizing or accepting electrons) than hydrogen have positive redox potentials (e.g., Cu/CU^{2+} : $E_O = 0.34$ V). Substances less electronegative (i.e., capable of reducing or giving up electrons) than hydrogen have negative redox potentials (e.g., Cr^{3+}/Cr^{2+} : $E_O = -1.07$ V)[67]

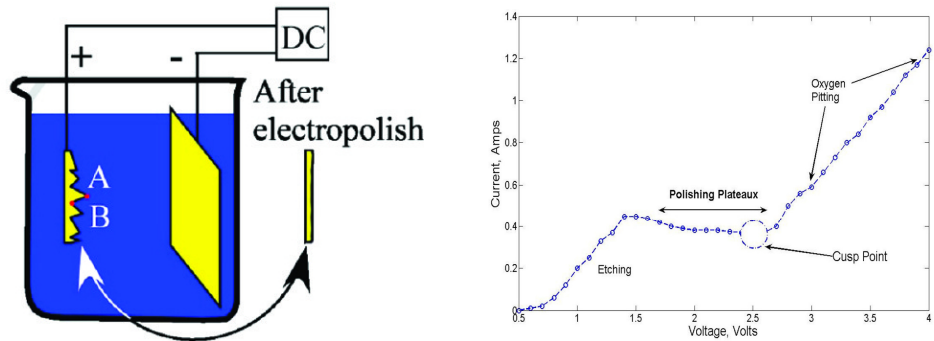
Removed mass from working electrode “The current flow of every two electrons results in one copper atom dissolved on the anode and deposited on the cathode. Since $1A = 1Cs$, the charge of one electron $e = 1.60218 \times 10^{16} C$, so the number of electrons (per second) in 1 A current is $N_e = \frac{I}{e}$; the number of copper atoms being oxidized or reduced $N_a = \frac{1}{2}N_e = \frac{I}{2e}$, the number of moles $N_m = \frac{N_a}{N_A} = \frac{I}{2eN_A} = \frac{I}{2F}$ where Avogadro’s number $N_A = 6.02214 \times 10^{23} mol^{-1}$. The weight of N_m mole copper $W = N_m M = \frac{IM}{2F}$ where M is the molecular weight of copper. Thus a volume, $V = W/d = \frac{IM}{2Fd}$ where d is the density of copper. Thus a current I produces a dissolution/deposition rate in thickness ($cm s^{-1}$)

$$R_d = \frac{M}{2FdA} I \quad (3.1)$$

where A is the area of the electrode surface. [67, p. 34]

Voltage-current-characteristic or polarization curve

- On a polycrystalline metal surface there are sites, such as defects and grain boundaries, where atoms are at higher energy states. In addition, due to arbitrary crystal orientation, there are different crystalline planes with different energy states of atoms on the electrode surface. Therefore, atoms at all these different sites and planes have different standard redox potential E_O , and as a result, have different dissolution rate according to eq. 3.1. Such an anodic dissolution will not lead to polishing. Instead, a crystallographic etching is produced (reference [9, 33-35] within [67]). This is true at lower current (or applied potential). This refers to the "etching" regime in figure 3.4(b) with $U < 1.5$ V.
- The plateau where the current remains almost constant with increasing voltage is referred to as "**polishing plateau**". Overall, the values of iL and EL of the limiting current plateau and the shape of a polarization curve depends on electrolyte solution, anode material, disk rotating speed, solution circulation, temperature, and the distance between anode and cathode. Of all the factors, electrolyte is the most important one determining the polarization curve.



(a) Sketch of a typical setup used for electro polishing. A beaker is used to hold the aqueous cell medium. The copper foil and a counter electrode are immersed and connected a the + and - connections of a DC power supply. Image reproduced from [71]

(b) Current-voltage characteristic indicating different phases in the etching and polishing process. While at low voltage etching is the dominant process, a polishing plateau is formed at intermediate voltages. Exceeding a threshold leads to increased formation of excess oxygen in the oxygen pitting regime. [72]

Figure 3.4: Experimental setup and voltage characteristic used for electrochemical polishing. 3.4(a) In the process the foil is connected as working electrode (+) and opposed by a counter electrode (-). Material is then transported from the working to the counter electrode resulting in a polished foil surface. 3.4(b) Choosing proper voltage and current values in the polishing plateau is important for good results.

- With continuing increase of applied potential, other reactions than Cu oxidation and reduction may occur and contribute to the increasing current. These reactions produce H_2 and O_2 bubbles, which occur at or reach the anode surface. This is known as "**oxygen pitting**".

gas bubbling Gas (oxygen or hydrogen) bubbles may block Cu^{2+} ion transport and therefore terminate the electrochemical dissolution process on the area inside the bubbles. However, the residual solution on the surface area inside the bubbles may react with Cu atom and result in chemical etching. Depending on the chemical property of the electrolyte solution and the value of current density at which the electrochemical dissolution is occurring, the etching speed can be higher than the rate of electrochemical dissolution. In this case, pits will be produced on the anode and produce a rough surface. If etching does not occur inside the bubbles, or if its speed is slower than that of electrochemical dissolution process, the area inside the bubbles will remain and appears as protruding particles after the electrochemical dissolution process. In either case, a rough surface is produced. Approaches to reduce the effect of oxygen bubbling are done by altering the etching solution with different additives.

Etching solutions in literature To find the most adequate polishing recipe, the most common ones have been reviewed and will be shown in the following. Many etching processes of Cu foils base of phosphoric acid that is referred to as ortho-phosphoric-acid, too. Liquid phosphoric acid is an 85% aqueous solution. [73]

Here (table 3.1), some of the etching recipes are given as reported in literature. They all have been used to electrochemically polish the Cu foil prior to graphene or boron nitride growth. We will discuss the used recipes in the following with focus on the additives used.

Different additives to the acid are used to gain a better control of the etching process. A typical one

Table 3.1: Table with some of the found etching recipes.

	unit	[72]	[71]	[65]
H_3PO_4	[mL]	300	100	50
H_2O	[mL]	—	—	100
2-Propanol	[mL]	—	—	10
Ethanol	[mL]	—	—	50
Butanol	[mL]	—	—	—
Urea	[g]	—	—	1
(P)EG	[mL]	100	0.1	—

is PEG.⁵

One may add PEG for reduced oxygen bubbling during the process (compare fig. 3.4(b))[71, 74]. It was shown that a concentration of 1000 ppm PEG decreases the amount of oxygen pits. A comparison between electro polished foils with and without PEG are shown in figure 3.5. After etching with purely phosphoric acid the surface remains rough and covered with pits. After adding PEG to the polishing solution the resulting foil shows a smoothed surface with little oxygen pits left.

A detailed investigation on polishing solutions based on phosphoric acid can be found in [67]. It was found that adding EG into phosphoric acid solutions decreases the limiting current. The more EG added the lower the limiting current. This is true for both undiluted and diluted (with deionized water) phosphoric acid solution. Diluting phosphoric acid - EG solutions with water (25%, curve 2 in Fig. 3-10 within [67]) increases limiting current as shown in table 3.2. Further diluting phosphoric acid - EG solutions with water (50%, curve 3 in Fig. 3-10 (within [67])) decreases limiting current. Limiting current plateau disappears at 12.5 % phosphoric acid + 37.5 %EG + 50 % water. As the etching times are quiet long, efforts have been made to reduce the polishing time by varying the polishing solution. Results with a more complicated etching recipe [65] are depicted in figure 3.6. Here the etching was performed with a large copper plate used as cathode. Alligator clamps are used to apply a voltage of 3 V to 6 V between the foil and the plate. The foil is used as anode (+). After 1 min the foil is taken out and rinsed with deionized water, further washed with ethanol, and then dried with compressed nitrogen gas.

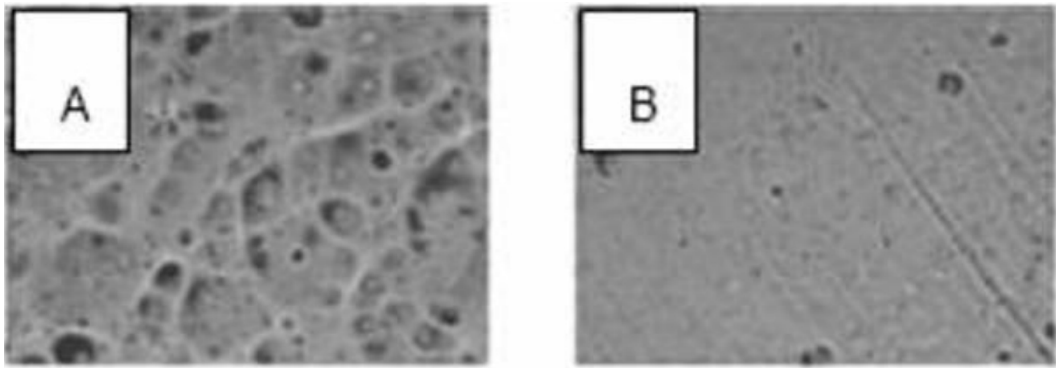
The height profile of the copper foil surface before and after treatment indicate diminishing striation height and overall roughness from $\approx 218 \text{ nm}$ to 64 nm within a very short period of time. Although the surface is still rather irregular, a dominant orientation of the remaining grains is observed in the (001) direction and helps the subsequent growth of graphene with toluene to form rectangular flakes.

Experimental setup

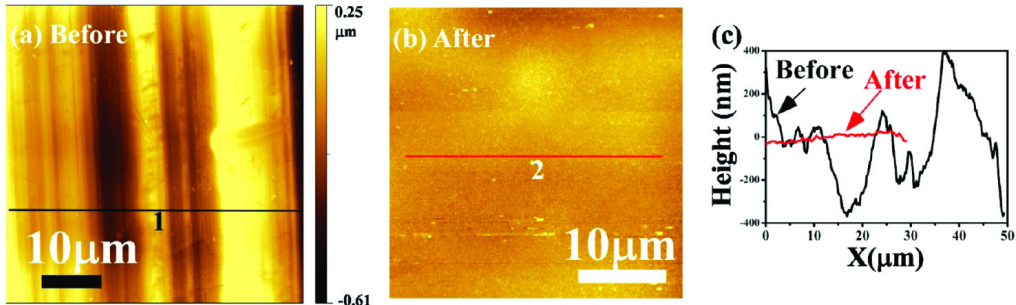
Used solution Within this work, Cu-foil polishing will be done with recipe I broken down in Table 3.3. It has several advantages. Since the main goal is to achieve a virtually flat surface, the resulting roughness of the surface is the most important parameter. In contrast to etching recipes without PEG (where oxygen pitting is an issue) and more complex etching recipes (to reduce etching time on exchange on surface roughness) a simple etching solution is chosen.

The etching process The etching process relies on the fact that the current density (and thus the etching rate) is higher in protruding regions of the copper foil (Ohmic leveling). As a result the

⁵Further additives are used in etching solutions. Isopropanol and Ethanol are introduced for a more stable current density. HEDP increases the critical current density in phosphoric acid solutions[67] and therefore the reaction rate. Citric acid is also used at low concentrations 1000 ppm [74]



(a) Surface characterization with an interferometer. Oxygen pits are clearly visible in (A) while after adding 1000 ppm PEG to the polishing solution greatly reduced their amount and smoothes the surface (B). See [71]

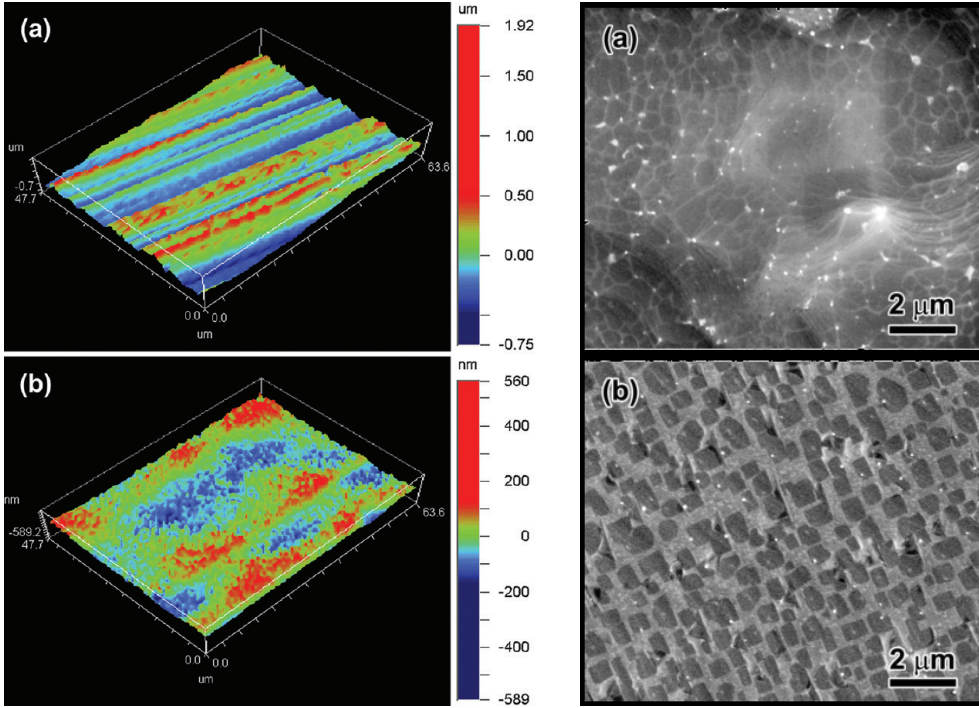


(b) (a-b) Copper foil before and after etching with 1 V to 2 V for 0.5 h following recipe [72]. Corresponding height profiles are shown in (c). Adopted from [72]

Figure 3.5: Effect of adding PEG to the etching solution. Interferometric and AFM topography images before and after polishing.

Table 3.2: Used etching solutions (compare [67, p. 130]). Note the change in the removal rate due to higher limiting currents in the solution after adding ethylene-glycol to the solution.

	I	II
85 % H_3PO_4	70	100
Ethylene-glycol	5	0
Deionized water	25	0
Potential [V]		1.2
Current [mA]	46	12
Roughness [nm]		5
Removal rate [$\mu\text{m min}^{-1}$]	1.0	0.26



(a) Noncontact optical profilometer scans in VSI mode of unpolished (top) and polished (bottom) Cu-foil surface.

(b) SEM images after graphene growth with a toluene precursor at 550 °C

Figure 3.6: Height profiles and SEM images before and after 1 min electro polishing with a solution reported in [65]. The linear striations, caused by mechanical processing of the copper foil, and the overall roughness of the surface decrease after polishing. Graphene coverage is increased under the same growth conditions, solely through better substrate conditions.

Table 3.3: Volume and mass fractions for copper foil etching solution.

	unit	H_3PO_4 (85%)	EG	H_2O
Dichte ρ	[g/cm^3]	1.87	1.11	1.00
$1/\rho_{H_3PO_4}$	[cm^3/g]	0.54	0.90	1.00
Anteil	%	70	5	25
Menge gesamt	[cm^3]	150		
Menge anteilig	[cm^3]	105.00	7.50	37.50
Gewicht	[g]	196.35	8.33	37.50

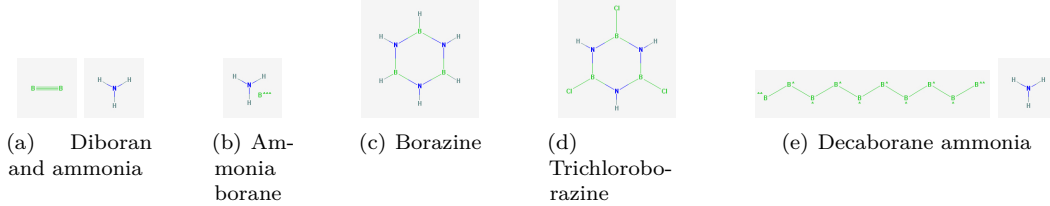


Figure 3.7: Precursor molecules for *h*-BN growth. (a) A mixture of ammonia and diborane, (b) ammonia borane, (c) borazine and (d) B-Trichloroborazine, (e) a mixture of decaborane and ammonia. Images reproduced from [75]

surface of the copper foil will be smoothed [72]. Compare with migration smoothing and diffusion smoothing[67].

3.2.5 Growing atomically thin ad layers with Chemical Vapor Deposition

There are many ways to grow ad layers with controlled stoichiometry in UHV. Here we will only focus on the most used method for sub mono layer and mono layer growth - the chemical vapor deposition (CVD).

When a gaseous precursor comes in contact with a hot transition metal surface, the precursor is split by pyrolysis into fragments. These then distribute across the surface and form new structures in a self-organized process. Choosing the right growth parameters like temperature, precursor partial pressure and time, high quality layers can be grown, whose stoichiometry is determined by the chemical structure of the precursor. Using carbon rich gases like ethylene (C_2H_4) [76, 77] and coronene ($C_{24}H_{12}$) [77] as precursor and a transition metal as substrate results in a graphene layer to be formed. Using boron and nitrogen containing molecules (see Figure 3.7)⁶ as precursor will result in *h*-BN to be formed. Hereby either single crystals⁷ or polycrystalline foils⁸ are used as substrates. These play a key role in interaction strength with the ad layer. Their lattice constant determines the mismatch with the ad layer. For some of these systems, DFT calculation back up experimental results [97].

self-limitation The precursors decomposes on contact with the hot substrate surface and its fragments form the ad layer. As time goes by, the ad layer grows in coverage and less free hot surface area is available for decomposing new “building blocks” for mono layer formation. If a mono layer is formed, no additional second layer is formed because of missing building blocks which only arise on contact with the uncovered substrate surface. Therefore this process is called self-limited. It is observed [78, 99, 100] for various substrates in combination with a borazine precursor.

⁶*h*-BN CVD precursor:
Borazine [52, 78–88]
B-Trichloroborazine ($ClBNH_3$) [89, 90]
Ammonia borane (borazane) [66, 91, 92]
Diborane and ammonia [93]
Reaction of ammonia with decaborane [94]
Triethylborane and ammonia [95]

⁷Single crystals used as growth substrate for *h*-BN:
(111): Ag [78], Cu [52, 79–81, 95], Ni [81, 82, 89, 96], Rh [84, 85], Pd [83, 96], Pt [84, 90, 96],
others: Cu(100) [91], Ru(0001) [84, 86]

⁸Polycrystalline foils used as substrate:
Cu: [66, 87, 88, 91–94]
Ni: [93, 94]

The growth by itself is well investigated on transition metal surfaces [83, 97], on the copper and nickel surfaces [79, 81]. Even more complicated samples can be created with this technique [101] and the following gives a short introduction in the occurring growth processes.

Some growth mechanics can be seen best in figure 3.8 that shows a XPS spectrum of borazine adsorbed on a Iridium surface held at 170 K and after several annealing steps.

At the graphics' bottom one can see the clean Ir surface with no borazine adsorbed (no B1s signal). There are two contributions in the Ir-peak. While the low energy (Ir_s) peak stems from the surface atoms of the substrate, Ir_b denotes the contribution from the atoms in the bulk. Upon borazine adsorption (1) a broad $B1s$ emerges accompanied with a new contribution in the Ir-peak (Ir_i) which is a result of borazine-Ir interaction decreasing the area of I_b and I_s . Upon annealing ((2)-(6)) Ir_i loses in intensity while the I_b and I_s recover to their initial position. Interesting changes happen to the $B1s$ peak. While at lower temperatures, several peak contributions can be distinguished, denoted as B_{mol} for entire molecules and B_{ad} for molecular fragments. With increasing temperature, B_{mol} decreases for a increase in the B_0 peaks. At lower temperature (1), B_{mol} decreases and B_{ad} slightly increases.

When exceeding 620K ($\approx 350^\circ\text{C}$, (3)) a new peak emerges and develops into B_1 when increasing temperatures. When temperature is high enough the only peaks left are B_0 and B_1 - the two contributions of boron atoms stem from boron atoms interact with the Iridium substrate with different strength due to different registry to the substrate.

While the growth temperature and partial pressures used to grow defect free *h*-BN layers varies, the basic principle remains the same on all substrates.

The exact growth of mono- and multi layers [93] is prone to discussion.

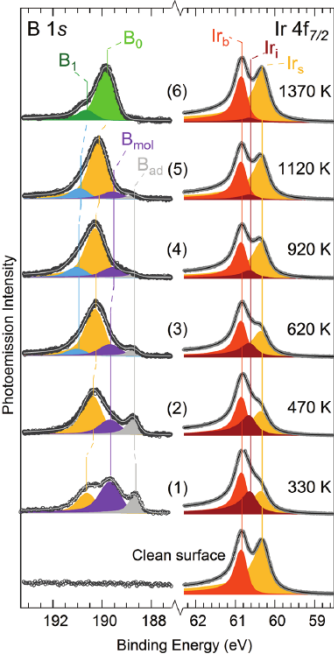
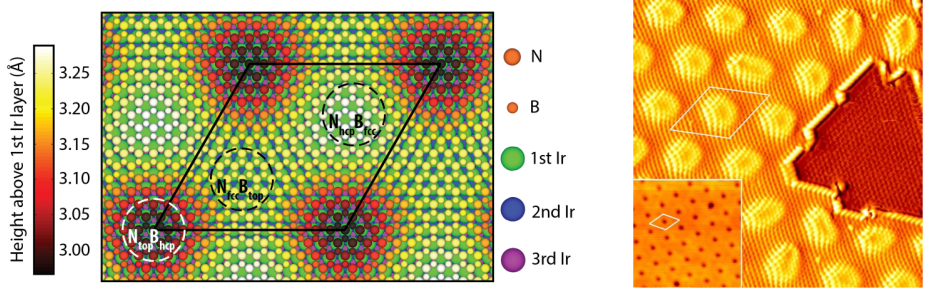


Figure 3.8: RT XPS spectra (B1s and $\text{Ir}4f\frac{7}{2}$) of borazine adsorbed on a Iridium surface held at 170 K and after stepwise annealing to 1370 K. Adopted from [98]



(a) DFT simulation of *h*-BN on Ir(111). The moiré unit cell as well as regions where B and N atoms occupy high-symmetry positions w.r.t. the Ir lattice are indicated. The change in adsorption height is caused by the changing registry of substrate (Ir) and ad layer atoms (B,N). Adopted from [103]

(b) STM image of *h*-BN grown with CVD on Ir(111) [58]

Figure 3.10: DFT calculation and STM images of *h*-BN/Ir(111). While being aligned, a lattice mismatch creates a moiré superstructure. It is well visible in adsorption height calculations 3.10(a) and as apparent height differences in STM images 3.10(b).

3.2.6 Geometric effects in ad-layers

The properties of various moiré superstructure are well described in literature and Hermann gives a comprehensive overview in his paper [102]. One can conclude the following:

If lattice constants are equal like in the case of a graphene bilayer, the needed lattice mismatch occurs due to a rotation of the two layers. A moiré is always present if an over layer shows a lattice mismatch with respect to the substrate.

For **isotropically scaled over layers** (refer to figure 3.9(a)) one can calculate the scaling factor

$$p = \frac{R'_{O1}}{R_{O1}}$$

which gives the size of the over layer lattice in units of the substrate lattice. The moiré pattern shows the same Bravais lattice type than the substrate[102, p. 10]. If moiré and ad layer lattice are aligned ($\alpha = 0^\circ$) the direction of moiré and substrate is aligned. If the over layer is isotropically scaled and not rotated, the period of the moiré calculates to

$$a_{\text{moiré}} = \underbrace{\frac{p}{|p - 1|}}_{\kappa} a_{\text{substrate}}$$

. With $a_{\text{moiré}}$ and $a_{\text{substrate}}$ are experimentally available, the ad layer lattice can be calculated with high precision (usually one order of magnitude more accurate than direction measurement of its period).

For a **scaled and rotated over layer** (figure 3.9(b)), the angle between substrate and moiré (γ [rad]) scales with the angle between over layer and substrate (α [rad]) as $\alpha = (1 - p)\gamma$.

For rotated and isotropically scaled over layers, one can determine the α and p from experimental observables γ (moiré angle to substrate) and κ (scaling factor) through relations $\tan(\alpha) = \frac{\sin(\gamma)}{\cos(\gamma) + \kappa}$ $p = \frac{\kappa}{\sqrt{1 + \kappa^2 + 2\kappa \cos(\gamma)}}$

When a scaled over layers over grows a step edge, the moiré pattern is altered. While period and orientation remain the same, a lateral shift in the superstructure is observed that interrupts the regular pattern and shifts subsequent moiré features by a vector \vec{V} .

Periodic change in work function A direct result of the lattice mismatch between *h*-BN and substrate is the alternating registry of ad layer atoms and substrate. The periodic modulation of B/N registry to the substrate atoms results in regions of stronger and weaker interaction between *h*-BN and substrate and is the reason for the nano templating effect of *h*-BN on many substrates. In the following some resulting effects are discussed that lay the foundation for a nano patterning effect of *h*-BN and its influence on the electronic structure of adsorbates.

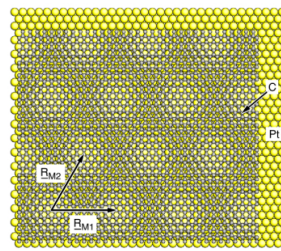
After growth of *h*-BN the substrates work function is reduced [Rh: 5.01 eV to 3.07 eV [97]. Therefore a dipole moment μ pointing from the bulk to the surface is necessary [104], rather likely created by a negative charge transfer from the bulk into the ad layer.

Free standing *h*-BN is investigated with *ab-initio* calculations [105–108]. Together with experiments [109] a crystal lattice constant of $a_{h-BN,RT} = 2.504 \text{ \AA}$ is derived. Depending on the substrates used, different lattice mismatches can be achieved as listed in Table 3.4. While substrates exist where the lattice constant are virtually identical ($\Delta \leq 1\%$), other substrates like Ag(111) show large mismatches.

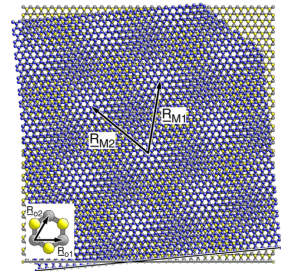
While a first report in 2004 [85], pointed to the formation of a complicated two layer structure, later experiments [80, 101] including ours [52, 79] and others *h*-BN/Cu(111) proposed a single layer of B & N atoms in a regular hexagonal lattice. It evolved as well investigated system to perform experiments on. It could be shown that after CVD growth it adsorbs on Cu(111) as a flat layer. Due to its lattice mismatch, "hill" regions (corresponding to a $N_{top}B_{fcc}$ registry) and "valleys" (corresponding to a $N_{fcc}B_{hcp}$ registry) are formed. In these regions the work function is altered in opposite directions. While larger at the hill/pore regions, the work function reduces continuously to its lowest value in the valley/wire regions⁹.

With changing work function, a lateral electronic field emerges, pointing from _____. It can be used to trap adsorbates with dipole moment along the field lines. This was shown for FePc and pentacene molecules on a graphene/Ru(0001) substrate. Here FePc molecules adsorb first on regions with high lateral dipole along top-fcc direction, followed by regions with lower lateral dipole. Pentacene molecules are trapped along the top-fcc direction [110]. This general adsorption mechanism is applicable for other systems with periodic modulation of the work function. Figure 3.11 depicts the work function change measured with STM (Field emission resonances) indicating a similar modulation of the work function. In this thesis TBP molecules ?? and helicene molecules in ?? are used as sample molecules for specific adsorption site or orientation alignment.

As mentioned in subsection 3.2.6 the orientation of the moiré superstructure is determined by its rotation alone, while its period is determined by lattice mismatch, too. This results in a variety of moiré superstructure orientations and periods.



(a) Isotropically scaled and aligned overlayer (gr/Pt(111); $p = 0.89$)



(b) Isotropically scaled overlayer with rotation of 5.4° (gr/h-BN; $p = 0.98$)

Figure 3.9: Adopted from [102]

⁹Please note that the notation is not uniform throughout the literature. Sometimes hills are referred to as pores and valley regions are denoted as wire regions.

Table 3.4: Lattice mismatches between *h*-BN and several transition metal surfaces. The mismatch is given to describe the relative size of the *h*-BN layer compared to the substrate, e.g. negative values indicate a larger lattice constant in the substrate bulk.

Substrate	Mismatch [%]
Ni(111)	0.4 %
Cu(111)	-1.9 %
Rh(111)	-7 %
Pd(111)	-9 %
Ag(111)	-13 %
Ir(111)	%

3.3 Used molecules

The following molecules have been used to conduct experiments. Images show the molecules in a $4\text{ nm} \times 4\text{ nm}$ area in an orthographic projection. Since all of them feature distinct properties, all of them are introduced in the following subsections. We will utilize porphyrine derivatives (subsection 3.3.1), functionalized pyrene molecules (subsection 3.3.2), helicene species (subsection 3.3.3) and coronene (wo central borazine functionalization, see subsection 3.3.4).

All the depicted molecules are modeled in Hyperchem[111] and calculated for optimized geometry with the AM1+ method. Afterwards their positions are exported and remodeled in blender. Note that this does not change their geometry. It is only for better control of the output (faster and more accurate model building especially in 3D) and for some aesthetic reasons.

3.3.1 Porphine: [di-[tert-butyl]-phenyl]-porphyrin derivatives

Tetrapyrroles like porphyrins and phthalocyanines play important roles in biological systems [112]. Both species are able to incorporate metal atoms that control the function. Not only are they interesting model systems to study interaction towards a (metallic) substrate[113–115]. Their use in metal-organic frameworks highlights the use of scientific knowledge to design "real world" sensor applications[116].

Tert-butyl functionals have been used in a variety of molecules [117]. Due to their bulky nature, they electronically decouple the porphyrin's de-localized p-orbital system from the metallic surface just by lifting the molecule. They may undergo heavy conformational deformation when outer influences (like metalization of the central porphine core) act on the molecule [118]. Switching capabilities are well investigated [119] and it is possible to switch them with the STM tip [120]. Experiments with similar molecules investigate the heat-induced formation of 1D and 2D conglomerates on a Au(111) surface.[63]

- Free base nitrophenyl - 5,10,15 Tri [di-[tert-butyl]-phenyl]-porphyrin has 3(2) di-tert-butyl-phenyl groups attached to the porphine macro cycle at the meso-positions of the molecule. The free meso-positions are occupied with nitrophenyl groups as shown in Figure 3.12(a) If more than one functional group is present, one can distinguish between trans (Figure 3.12(b)) and cis configuration (Figure 3.12(c)), whether the two functional groups are opposite or neighboring.
- The appearance of STM data is correlated to the molecular configuration according to [121] meaning that the lobes consisting of (3,5-di-tert-butylphenyl) are imaged as bright protrusions, while the functional nitro group is imaged fainter. This holds true for cis- and trans-substituted molecules[122].
- Tert-butyl groups can rotate and form flexible legs. Interaction with the substrate results in adsorption-induced conformational changes.[123]

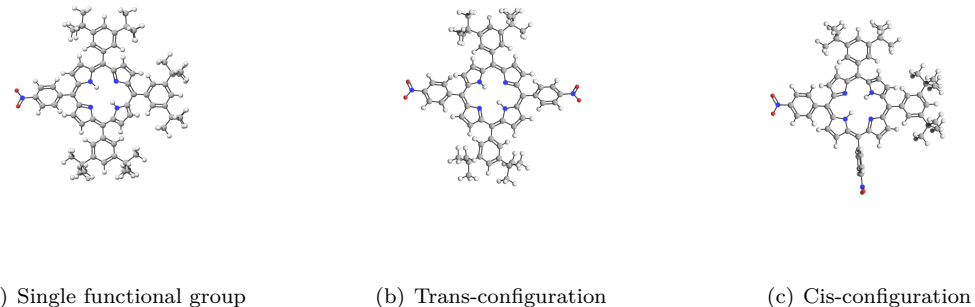


Figure 3.12: Functionalized tert-butyl-phenyl-porphines. (a) shows a single functionalized porphine molecules. An additional function may be added in (c) cis- and (b) position.

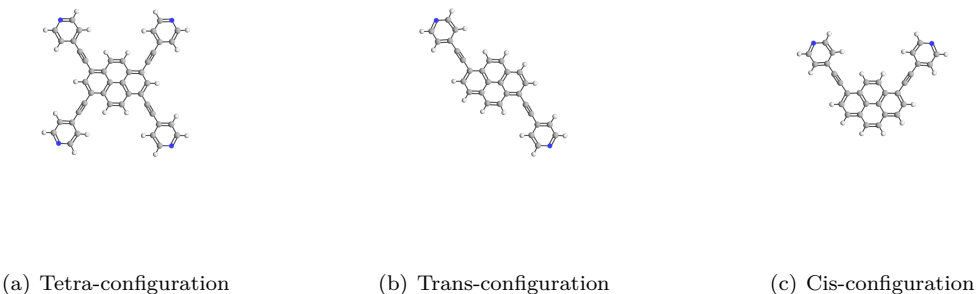


Figure 3.13: Pyridyl-Pyrene molecules in trans- (b) and cis- (c) and tetra- (a) configuration

Drawings for various functional groups and molecules can be found in [124]

one-leg: 5,10,15-Tri(3,5-di-tert-butylphenyl)- 20-(Nitrophenyl)porphyrine

two-leg cis: 5,10-Bis(3,5-di-tert-butylphenyl)-15,20-Bis(Nitrophenyl)porphyrine

two-leg trans: 5,15-Bis(3,5-di-tert-butylphenyl)-10,20-Bis(Nitrophenyl)porphyrine

3.3.2 Pyrene: Pyridylethynyl functionalized pyrenes

tetra-pyrene: 1,3,6,8-Tetra(4-Pyridylethynyl)pyrene

cis-pyrene: 1,8-Bis(4-Pyridylethynyl)pyrene

trans-pyrene: 1,6-Bis(4-Pyridylethynyl)pyrene

3 Experimental setup and sample preparation

Table 3.5: Evaporation and degas temperatures used for different molecules.

Name	Configuration	Degas [°C]	Evaporate [°C]
TPCN	—	—	490
TBP	single	4 h @ 200 °C	390
	cis	—	400 °C
	trans	4 h @ 200 °C + 1 h @ 270 °C	370 °C
pyrene	cis	2 h @ 180 °C	
		+ 1 h @ 200 °C + 10 min @ 235 °C + 1 h @ 220 °C	250
	trans	1 h @ 230 °C	265 °C
DCDB	—	1 h @ 100 °C to 150 °C	
		+10 min @ 170 °C + 25 min @ 200 °C + 40 min @ 220 °C	220 °C to 240 °C

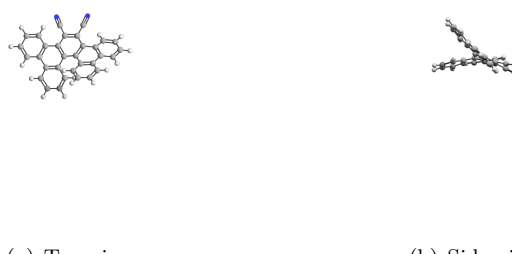
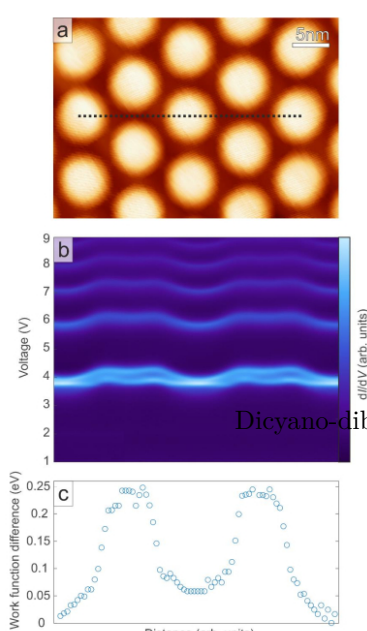


Figure 3.14: DCDB on copper surface. (a) Top view, (b) side view



³⁴Figure 3.11: Work function variation along *h*-BN/Cu(111) moiré.
(a) STM image showing the *h*-BN moiré with a periodicity of 8.4 nm. Scan parameter:
 $U_b = 4.0V, I_t = 40pA$. (b) Field

Pyrene molecules, first investigated in 1973 [125], are 4 ortho-fused carbon rings to result in a rhombic structure. As many other π conjugated systems they show interesting optoelectronic properties like [126–130] and assembly was investigated [62, 131–133]. Here they are used to investigate the influence of the number and position of functional groups on these properties. The very same species have been investigated on Cu(111) albeit data adsorbed on *h*-BN/Cu(111) was lacking up to this point. The nano-patterning effect of the *h*-BN substrate is used here to modulate the wide band gap of the species and therefor their optical properties.

3.3.3 Helicene: Cyano functionalization of helicenes

Helicenes were first synthesised 1950's [134]. They consist of ortho condensed carbon rings that form a spiral due to overcrowding in their center. While they first drew attention due to their fluorescence properties [135], helicenes are interesting molecules because of their

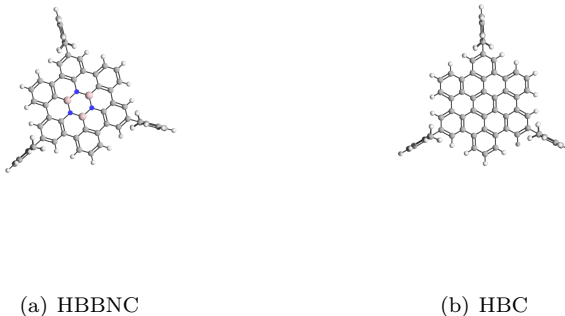


Figure 3.15: (a) HBBNC and (b) HBC

chiral feature. Two different turn directions exist, left and right. The molecules investigated in this work are functionalized with two benzene rings at positions ____ and two cyano groups at positions seven and eight. For more information, please refer to ??.

3.3.4 Coronene: HBBNC and HBC

HBBNC: 2,8,14-triptyl-hexaphenyl borazinocoronene

HBC: 2,8,14-triptyl-hexabenzocoronene

While in 2015[136] and 2016 [137] hexy-peri-Hexabenzoborazio coronene (HBBNC) was synthesized, its bad solubility prohibited experiments. In 2017 the synthesis [138] of a soluble, BN-doped coronene derivative by substitution of the central carbon ring was successful. By using HBBNC the HOMO-LUMO band gap could be widened and shows blue-shifted emission properties[138] compared to its all-carbon counterpart. Investigations with STM are performed on Au(111) [136]. Here the central $(BN)_3$ core is oriented to point all nitrogen atoms towards the leg functionalization. Due to the different electro negativity of the atomic species adsorption of gases in the central part can be interesting effects to look out for. In this thesis we focused on the geometric properties of this molecule first. Please refer to ?? for detailed information.

4 Epitaxial hexagonal boron nitride on copper foils

- Challenges in mass production (example)

Ease of use

Costs

How to overcome (example)

For this reason, we focused on the use of cheap substrates to achieve the very same functionality as on expensive single crystals. In this chapter copper foils are first chemically polished and prepared for investigation in AFM (p. 39), SEM (p. 38) and STM (p. 39). After CVD growth of *h*-BN with borazine, foils are investigated in XPS (compare Figure 4.9) - (discussion of peaks can be found inside the text. Comparable experiments are performed by [71, p. 8]). A comparison to bought *h*-BN foils is found at the end of the chapter.

4.1 Pre-treatment of Cu-foils: Polishing

Experiment realization The first attempt to etch the Cu-foil was performed with the 5%_{vol} EG, 25%_{vol} H₂O filled up with phosphoric acid. The etching was performed in a 200 ml beaker, filled with 150 ml etching solution. The setup is as depicted in Figure 3.4(a). The potential was adjusted to be 1.2 V after some minutes. The current through the solution changes and is typically highest when the etching process started.

After some minutes, the foil starts to change. The reflectivity changes, making the foil - shiny before etching - a little dull. After some additional time the foil begins to reflect light better again. This is the moment where the etching process is interrupted. The time inside the etching solution depends on the handling (like shaking the beaker or moving the foil in the solution - but was usually ≥ 2 h.¹

ADD IMAGE from actual setup

One has to be careful if reproducible results are needed. During the etching process (as more and more copper settles on the counter electrode), the current and therefore the etching rate decrease continuously. When the beaker is moved, some of the debris on the electrode changes (the electrode's) surrounding and the etching rate (limiting current) increases again. Front- and backside of the foil are suspect to different etching rates. The back side is generally more flat, the side facing the counter-electrode always shows some additional protrusions.

ADD IMAGE from polished foils

After etching treatment The foil is taken out and cleaned from remaining etchants with purified water first and isopropanol afterwards. Foils are stored in isopropanol to avoid oxidation.²

¹Since the perfect voltage/current to perform polishing varies in time a automated etching process has been developed [139]

²To further improve the quality of the foil, one can follow the documented recipe for annealing the foil in a H₂ atmosphere (10 sscm, 1000 °C, 30min)[88] to increase the copper grain size and further smoothen the surface. We decided to further prepare the foils within the UHV chamber and skipped this step.

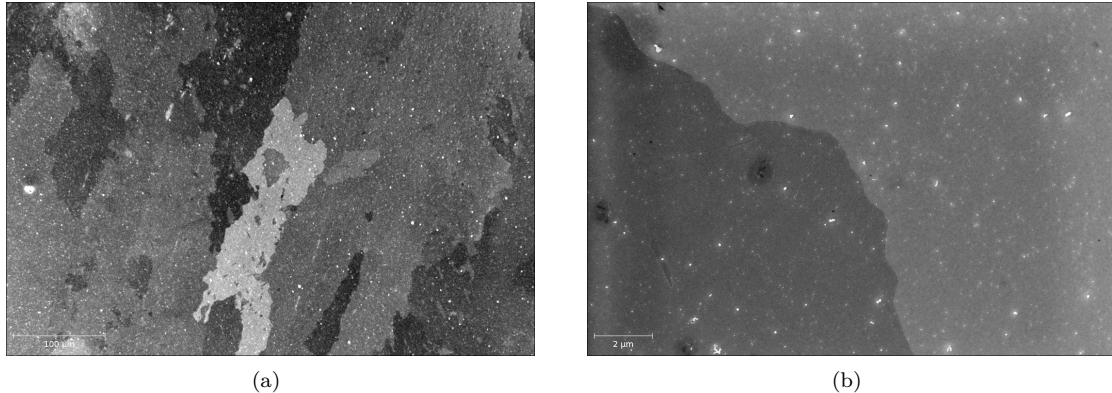


Figure 4.1: SEM image of etched copper foil. Different contrast suggests different grain-orientation within the surface. (a) Larger ($570\text{ }\mu\text{m} \times 380\text{ }\mu\text{m}$) image showing the contrast of different grains in the copper-foil, (b) zoom ($18\text{ }\mu\text{m} \times 12\text{ }\mu\text{m}$) to a area with two different contrasts and their border.

SEM Invented in the 1930's by Manfred von Ardenne[140], Scanning electron microscopy (SEM) is another versatile tool for the experimentalist. In contrast to (LT-)STM and AFM, SEM is capable of imaging huge areas of the sample within a very short time, which allows for a vast overview as well as good statistics. Magnifications reach up to 500k and above, illustrating even features in the order of 1 nm.

As the name already discloses, SEM scans the surface with electrons. Their interaction with the material are diverse and some of them are explained in the following. While all effects are present in every measurement, not every microscope features detectors for all of these. While detectors for secondary electrons are standard equipment others may be not.

The primary electrons are created with a filament. These often consist of tungsten (metal, high melting point, low work function). Alternatives are lanthanum hexaboride (LB_6) - often used in LEED setups, too - or zirconium oxide. Electrons are accelerated (typical energies are within 1 keV to 40 keV) and focused on the specimen surface in a spot with few nm diameter with condenser lenses. Scanning the surface is achieved with coils that deflect the electron beam and therefore the actual scanning spot.

When the electrons hit the surface, they interact with the specimen in a small volume. The volume depends on the electron's energy, the atomic number Z of the specimen and the specimen's density. It is typically in the order of $0.1\text{ }\mu\text{m}$ to $5\text{ }\mu\text{m}$.

Drawbacks:

- Sample has to be mounted → no in-situ measurement, surface alteration in between
- Rather "dirty" vacuum → surface alteration while measuring
- Measurement destroys sample → adsorbate build-up due to chemical reaction below e-beam

One can see in Figure 4.1 that the surface imaged in different intensities which correspond to the different orientation of the copper grains within the foil[141]. The grain size may range from just a few μm to several hundred μm and in some cases even mm. The grains are separated by grain boundaries. Large grains are preferred for growing graphene on copper foils because grain boundaries are subject to inhomogeneities within the graphene layer and provide a route for unwanted surface chemistry (copper oxidation for example). These effect can be also be used to highlight grain boundaries as shown in [141].

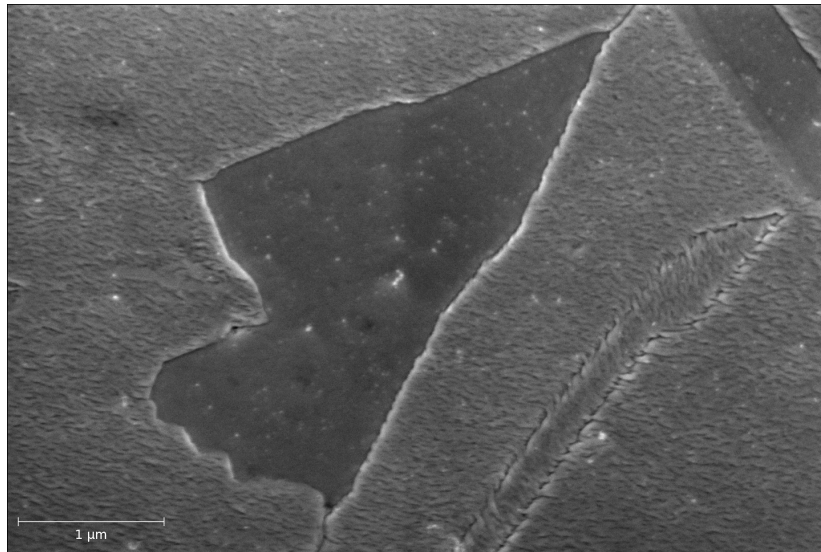


Figure 4.2: SEM image that shows different surface morphologies (5.6 $\mu\text{m} \times 3.7 \mu\text{m}$)

Although not very rough, the copper foil shows surface variation. While some areas of the sample show some wavy surface, whereas other are much flatter and appear in a different intensity (Figure 4.2).

Neither estimation on the grainsize nor guesses for their absolute orientation have been done due to the lack of EBSD-data in the SEM setup.

AFM Figure 4.3 shows the striations that stem from the production process (from top to bottom). After etching ($U = 1.2V, I=120\text{ mA to } 250\text{ mA}$) for 5 h in a solution (shown in table 3.3) the striations have gone and the RMS value decreased by 30 % to 45 % and an increase in foil quality is obvious even with bare eyes. Figure 4.3 and 4.4 show AFM images in the same size and contrast - before and after etching. The circular hole is an effect of bubbles in the etching process where the bubble affects the rate of etching. The over all structure changes from a heterogenous sample height to a flat height contribution with only a little amount of defects. Those are sufficiently separated in space to exhibit flat regions where the h-BN may grow unperturbed.

not done yet - maybe future? Some foil has been mechanically polished with 4k paper and several hours of Syton polishing. The roughness of these samples has been investigated also in AFM. These are comparable to the chemically polished ones, but are always slightly higher by $\approx 10\%$. Sometimes unwanted new scratches appear after mechanical polish.

STM The bought and chemically polished foils are mounted on a sample holder and loaded into the load lock. It is evacuated for 2 h to 3 h, afterwards the valve is opened to the chamber. During transfer, no noteable increase in the base pressure is noted. The sample is put on the parking slot.

The sample was initially degassed with slowly increasing temperatures to remove adsorbates like CO , CO_2 and H_2O .

After some time of degassing, the sample was prepared with repeated sputter and anneal cycles. The annealing temperatures were increased up to 800°C . After that procedure, the sample was cooled down and observed in STM.

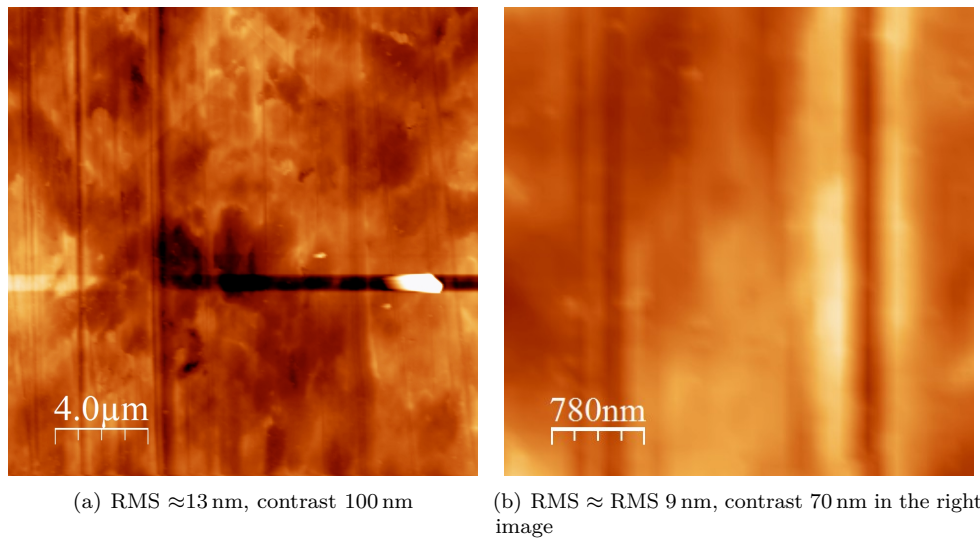


Figure 4.3: AFM image of the 0.25 mm copper foil as bought from alfa aesar.

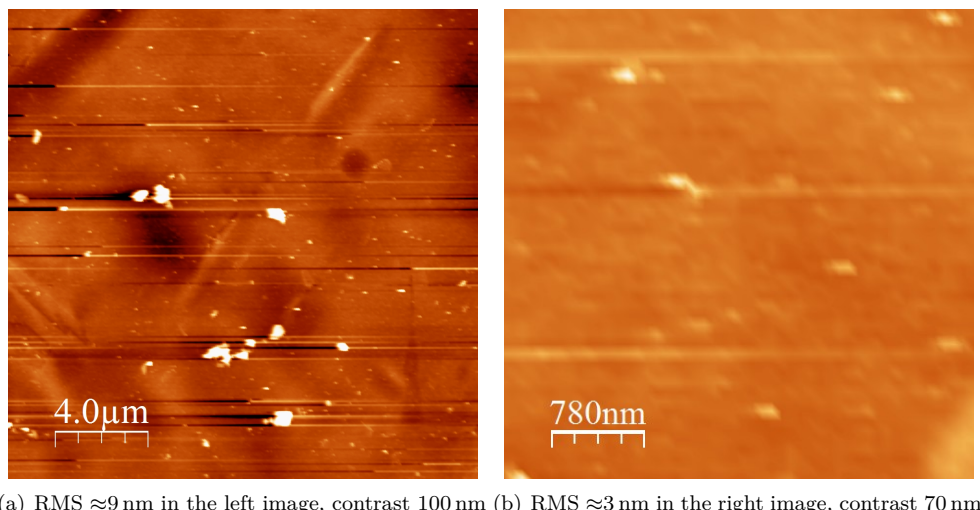


Figure 4.4: AFM image of a copper foil polished 5h (according to table 3.3)

4.2 Characterization: SEM & STM of *h*-BN on Cu-foil

Further experiments were carried out to increase the cleanliness of the *h*-BN on the polycrystalline copper foil. To reduce the amount of elements coming from the body of the foil, it is repeatedly sputtered and annealed to temperatures as high as 800 °C. This may have also an improving influence on the grain size and amount of corrugation. Several attempts have been made which are described in summary below.

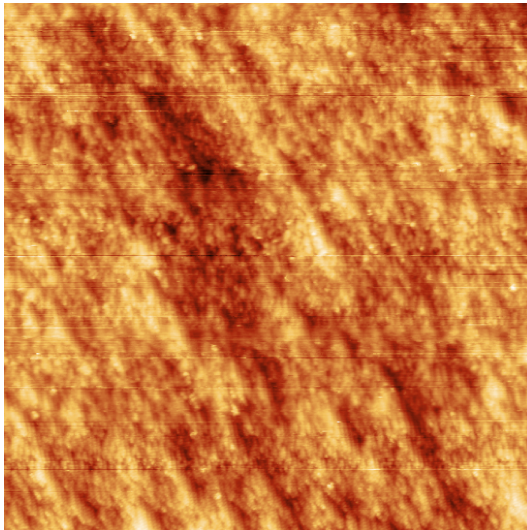
- After cleaning, the sample is investigated in STM. The foil shows a inhomogeneous topography, with parts of the sample showing very flat regions while others still remain heavily corrugated and not scan able in STM. A first look onto the quite heterogeneous surface reveals flat areas with a typical roughness of ≈ 70 pm exist (Figure 4.5(a)). Areas with very large corrugations ≥ 100 nm are hard to scan in STM and bad places for *h*-BN growth. Although being flat, the polycrystalline foil shows a lot of unordered substrate steps and a dirty surface, covered with adsorbates imaged as small bright dots.
- The sample was sputtered and annealed several times to temperatures of 800 °C. Before the dosage it was held 5 minutes at 750 °C. Borazine was dosed with the same pressure as before (1×10^{-7} mbar) but for 1min and at a lower temperature of 750 °C. After the preparation the sample was kept at 750 °C for another 1 minute. It was cooled down slowly (shown in Figure 4.5(b) and Figure 4.7(a)).
- The foil was sputtered and annealed 4 times with temperatures of 800 °C. Borazine was dosed at 2×10^{-7} mbar for 2.5 min. The sample was kept at 750 °C for another 5 minutes after dosing. The sample was cooled down slowly. Figure 4.7(a) shows some of the grown islands. The copper surface changes upon *h*-BN growth and the terrace width increases below the *h*-BN flakes. The typical faceting of the surface vanishes or can at least not be depicted because of the overgrowing *h*-BN (Figure 4.7(b)).

points to point out:

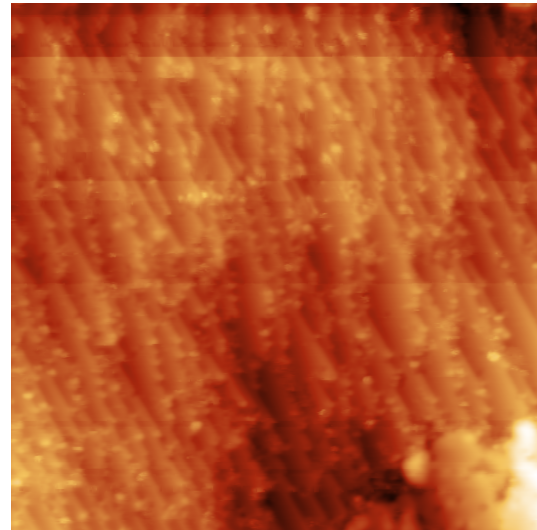
- Look at Messzeit-April.ppt power point presentation
- Stufenhöhe
- Beschaffenheit der stufen/facetts → material transport mechanism/strength differs uner the *h*-BN compared to the bare cu-foil surface.
- Wechselwirkung BN-Wachstum und Facettenbildung

surface structure of *h*-BN on Cu-foil During experiments some “new” structure appeared (compare figure 4.8). The apparent height change between the both terraces is 130 pm separated by a slim trench that is slightly lower than the right terrace (50 pm). The parallel stripes have an apparent corrugation of 25 pm and are separated 70 pm from each other and cover the whole image.

The adsorbed TPCN molecules show different apparent heights in their molecular center. Some fragmented and heavily deformed molecules are visible.



(a) A flat area of the cleaned copper foil with no larger corrugation is shown before *h*-BN growth. The roughness is 70 pm.



(b) STM image after 4.5 L of borazine dosage on a 750 °C hot copper foil surface. A small *h*-BN island can be seen (lower right) on a largely uncovered copper foil background.

Figure 4.5: Cu-foil after repeated sputtering and annealing cycles (a) and after CVD growth of a sub-ML *h*-BN (b). Imaging parameters: (a) 3.6 V, 0.1 nA, color scale 0 pm to 600 pm, Image width: 88.6 nm, (b) 1 V, 0.37 nA, color scale 0 pm to 900 pm, Image width: 44.3 nm.

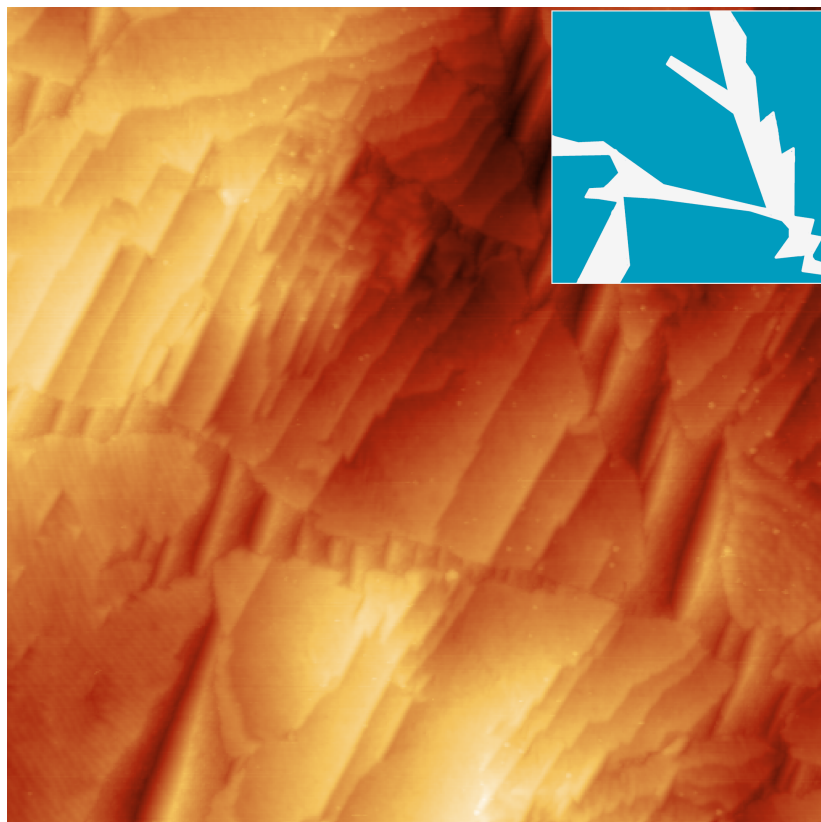


Figure 4.6: STM image of 22 L borazine dosed on a 800 °C hot copper-foil surface. Several large islands can be seen that grow over Cu-foil step edges. Inset shows coverage with *h*-BN ad layer in blue. Imaging parameters: 4.7 V, 0.2 nA, color scale 0 nm to 7 nm, Image width: 295 nm.

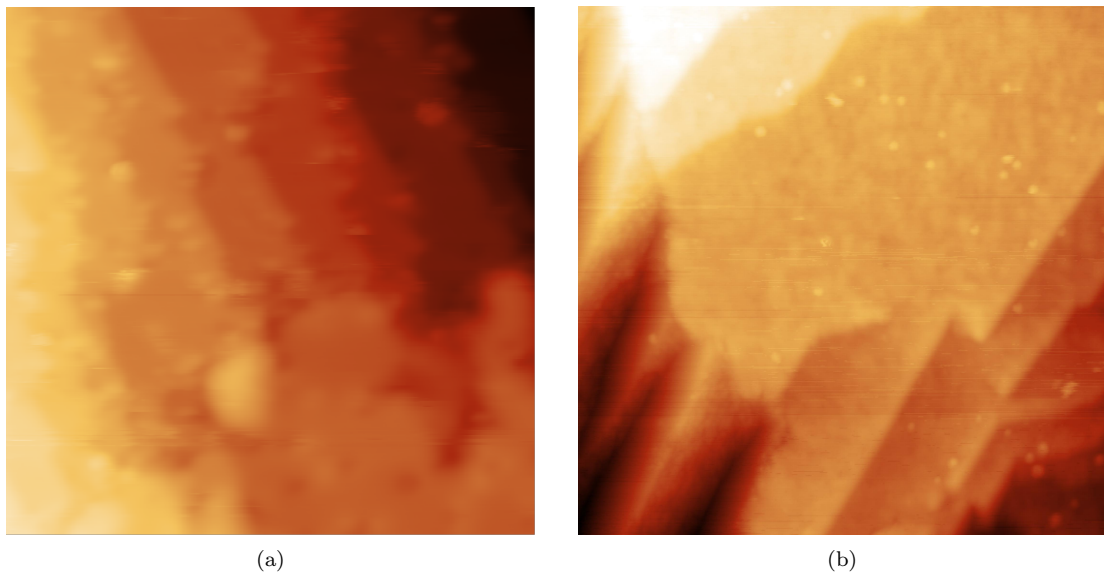
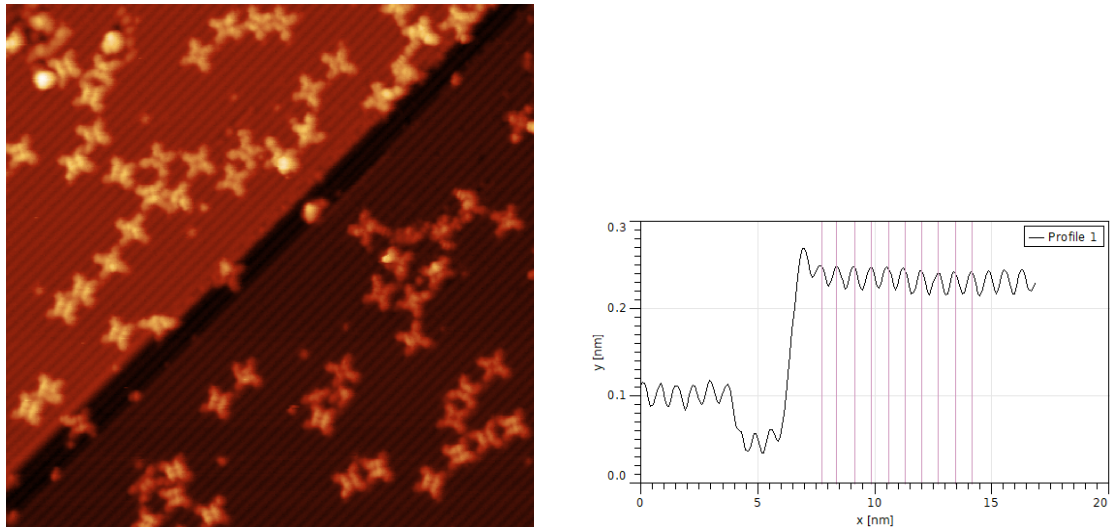


Figure 4.7: STM topographies of *h*-BN islands that overgrow Cu-foil facets. Imaging parameters: (a) 1 V, 0.37 nA, color scale 0 nm to 1.5 nm, Image width: 18 nm, (b) 3.5 V, 0.5 nA, color scale 0 nm to 4 nm, Image width: 73.8 nm.



(a) Molecules on copper foil surface - supposed to be covered with *h*-BN, maybe just free (maybe faceted) copper. Stripes not visible on the lower terrace, although present in the same orientation.

(b) Line spectrum across the step shown in (a) perpendicular to the trench. No molecules were crossed.

Figure 4.8: Surface structure of copper foil after deposition of TPCN molecules. Two terraces are visible, both covered with linear stripes - oxygen over layer (2x1)? - cu reconstruction? - maybe some very small (0.75 nm) linear moire on a Cu(100) facet? Noise can be excluded due to the fact that the stripes do not occur on the molecules, but only on the substrate. Adsorbed TPCN molecules appear as cross shaped protrusions. Many deformed molecular cores visible throughout the image → strong substrate interaction → no *h*-BN! Line spectrum shown in (b) indicating a period of 70 pm. Imaging parameters: (a) 1.26 V, 0.04 nA, color scale 0 nm to 0.8 nm, Image width: 40 nm

4.3 Characterization: XPS of self-grown *h*-BN/Cu-foils

Copper foils with 0.25 mm were bought and repeatedly sputtered/annealed. Several grow cycles of *h*-BN via CVD of borazine were done. The sample is transferred to the XPS-STM chamber and again sputtered/annealed several times to clean it properly.

The needed dosage of borazine to assemble a full monolayer of *h*-BN is derived via a combined STM/XPS measurement. Several preparations were done to understand the growth behaviour of *h*-BN on the copper foil. Coverages are measured in STM while the chemical composition of the sample was assessed with XPS.

Table 4.1: Determination of the full monolayer borazine dosage. First a certainly saturated sample was prepared (I) and measured in XPS/STM. A sub-monolayer (II) was grown and compared to the monolayer STM and XPS results.

	Prep.	Position	Area [arb.u.] [eV]	FWHM [eV]	Anode Element	Dosage [L]	Coverage (STM)
B1s	I	191.1	3776	1.35	Mg	4736	100 %
	II	191.1	1994	1.35	Mg	789	53 %
N1s	I	398.7	5875	1.45	Al	4736	100 %
	II	398.6	3183	1.43	Al	789	54 %

When comparing the resulting coverage (STM coverage/XPS signal) (II) to the (saturated) monolayer (I) one can derive the minimal amount of borazine needed to process a monolayer of *h*-BN on the copper foil. Comparing the coverages of a sample grown with CVD, 7×10^{-6} mbar for 15min (I) and one grown with CVD, 3.5×10^{-6} mbar for 5min (II), shows that reducing the dosage by a factor of 6 does not reduce the coverage by a factor of 6, but just by a factor of 2. Therefore (I) features a full monolayer and (II) only half of it. It follows that a full monolayer may be achieved by dosing 1500 L borazine on a 800 °C hot copper foil surface. Because the growth rate may certainly not be linear (less and less free copper surface to decompose borazine into building fragments while the layer assembles) the given dosage is a minimum estimation to achieve the monolayer.

Even though a much larger amount for borazine (4736 L) than needed for a monolayer (1500 L) has been dosed, the maximum coverage did not exceed the XPS signal of a monolayer. So the growth of *h*-BN on copper foil is self-limited (as in the case of many *h*-BN/metal systems) to a full monolayer. It is not possible to achieve layer growth with this type of preparation.

T and t dependence is not subject to investigation because the growth is supposed to follow the same mechanisms as on the single-crystal case. Quite some investigation has been done, [84, 98] to understand this process and literature has matured.

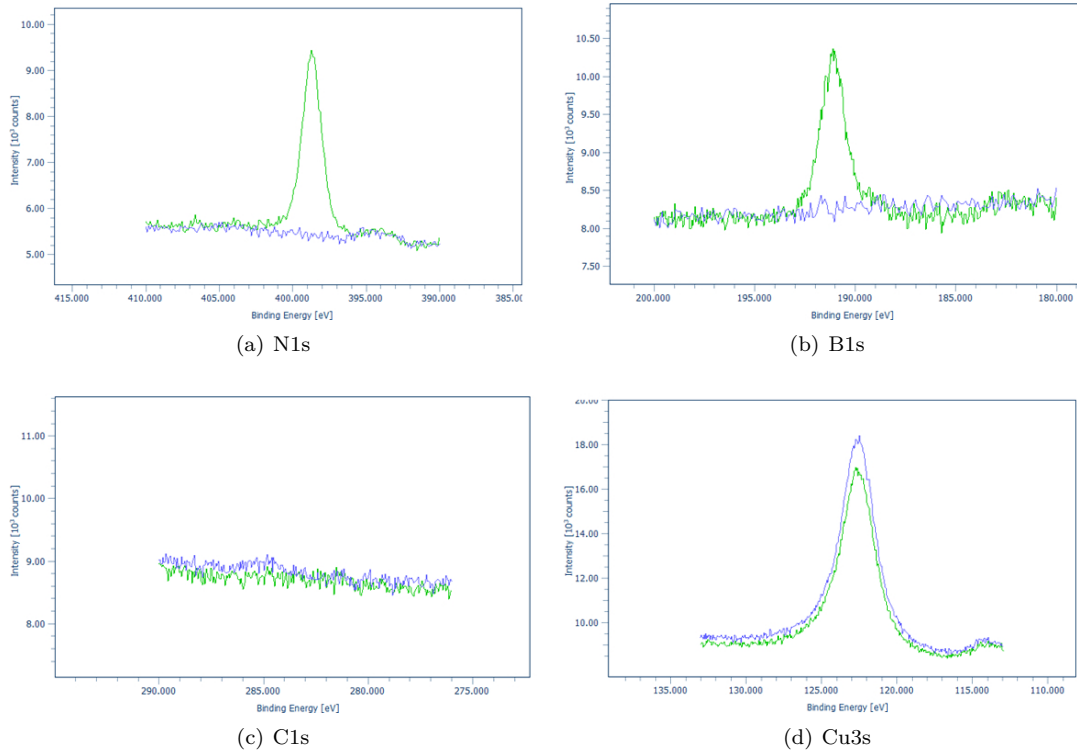


Figure 4.9: **REDO! Axis too small!! Check layout with other XPS measurements!!** XPS spectra for ML *h*-BN/Cu-foil. The peaks are at their expected positions[87] and show no additional features. No remnants of sulfur or remaining oxygen could be found.

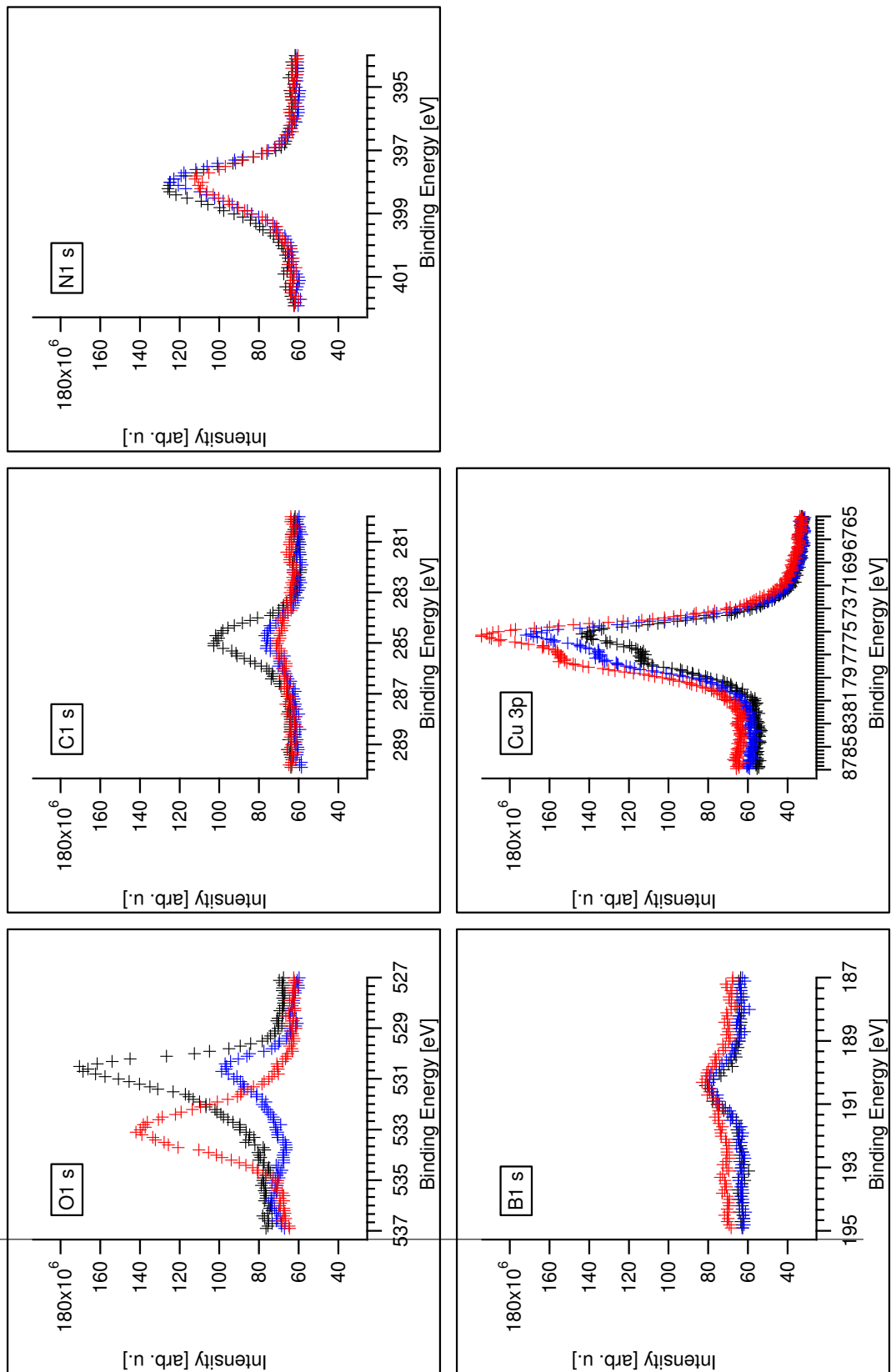
4.4 Characterization: XPS of bought *h*-BN/Cu-foils

The quality of the as-bought *h*-BN on copper foils[142] is examined in XPS. The XPS spectra shows contribution of different atomic species. There are peaks for the O-atoms (1s: 529 eV to 535 eV), C-atoms (1s \approx 285 eV), N-atoms (1s \approx 398 eV), B-atoms (1s \approx 190 eV) and Cu-atoms ($3p_{1/2,3/2}$: 70 eV to 80 eV)). One would expect the shape of the 1s-peaks to be singlet-like (one peak, gauss shaped) and the 3p-peak to be a doublet (two close lying peaks with area-ratio 1/2:3/2=1:2).

O1s Position varies with temperature. The signal at room temperature(black) stems from adsorbed water and CO. These desorp with increasing temperature(blue). When going to higher temperatures(red) this peak increases again and shifts to higher binding energies. Not present in self-grown *h*-BN (figure 4.9)

C1s The C1s Peak decreases with increasing temperature and retains its position. This has the same reason as for the O1s peak (desorption of CO due to the heating). Some of the carbon remains on the surface - even at temperatures as high as 970 K.

N1s/B1s The nitrogen/boron peaks show some temperature related changes. There is little change upon annealing to 630 K, both peaks shrink, but stay almost constant in their position in binding



energy (slightly shifted to lower binding energies by about 0.2 eV). Position is [N1s: 398.1 eV | B1s: 190.2 eV]

Cu3p The copper peak exhibits an increase in area when increasing the temperature. This is because some of the water and CO adsorbate desorb and more and more copper is contributing to the signal. This peak is a doublet, so both signals come from the same chemical copper surrounding.

The $Cu(OH)_2$ O1s peak is expected to be at 531.3 eV to 531.7 eV[39] which may explain the shoulder of the O1s peak to higher binding energies (O1s metal: 531 eV). Nitrates (NO_3) have binding energies in the range from 532.5 eV to 533.5 eV[40, p. 45]. This would imply either an replacement of nitrogen with oxygen, or some kind of oxygen on top or below the nitrogen in the BN. As proven by Simonov et al. in [143] the (!atomic!) oxygen tends to replace the nitrogen in the *h*-BN/Ir(111) system when it is annealed to 600 °C (compare figure eight therein). Thus it forms $B_xN_yO_{1-x-y}$ over-layers. The longer the oxidation time the higher the amount of replaced nitrogen (figure two therein). If this effect is responsible for the O1s peak at high temperatures is questionable, since the oxygen has to be cracked somehow - where no process can be thought of (no catalytic cracking at metal surface possible - full ML, thermal energy to low to reach binding energies of O_2 (no citation here, nothing found - just a guess)).

An exchange of O with B or N would be easily visible in XPS (due to changed N/B surroundings. Not sure if the signal of oxygen is large enough for that. Check DATA - confirm maybe

4.5 Application: Molecular functionalization with TPCN

The Cu(111) support for the h-BN growth is replaced by a polycrystalline copper foil. The goal is to achieve the same ordering of molecules on the h-BN surface. The h-BN layer has been prepared by a dose of 5×10^{-7} mbar borazine for 20min (4500 L). During dosage the foil has been kept at 820 °C.

When a h-BN spacer layer is introduced, the molecules decouple from the substrate, lowering their interaction with the afore-mentioned. This can be seen in a change of the molecules' footprint (rectangular → square).

They do not form ordered networks (like chains or squares) and lie rather loosely on the h-BN layer (compare 150807.142226.dat). They can easily be moved with the STM tip (1V, 10nA). In some areas, denser TPCN islands form. Here they lie right next to each other, each slightly shifted to match the neighbouring molecules and to achieve the dense packed regions. The same motiv was already investigated in the same system [144].

During scanning ($I=0.1$ nA, 0.9 V $< U < 1.3$ V) of a group of molecules, a single molecules could be pushed out of the group (compare figure 4.11. While the chain initially consisted of 3 molecules in a row, after scanning one of the molecular units moved to the left while the remaining two stay at their positions. A closer look to the moved molecule's geometry reveals deformation of the legs.

It was shown that the imminic nitrogen species within a 2H-TPP molecule strongly interact a Cu(111) surface, thus orient along high symmetry directions. [145–150] Rotation and diffusion are limited.

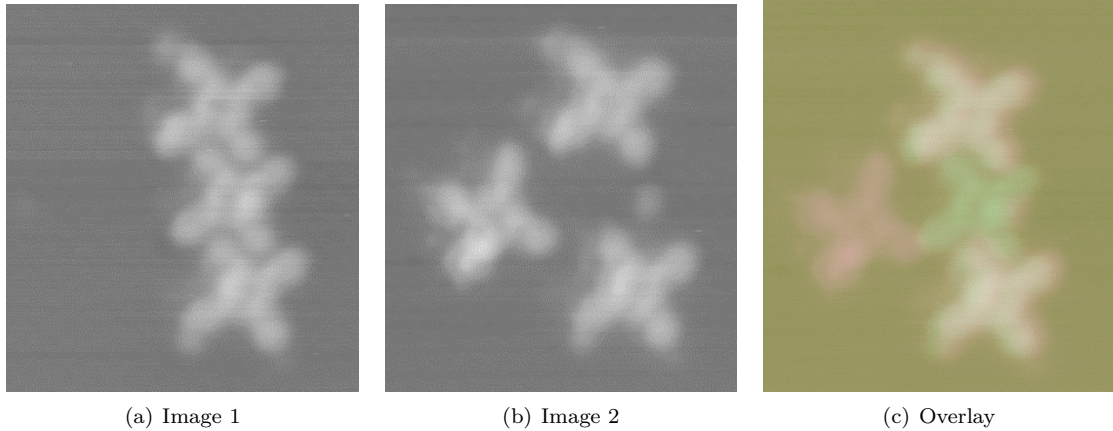
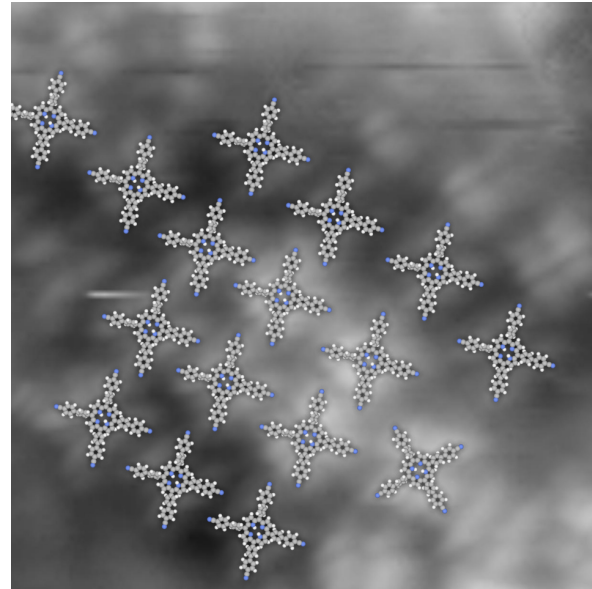
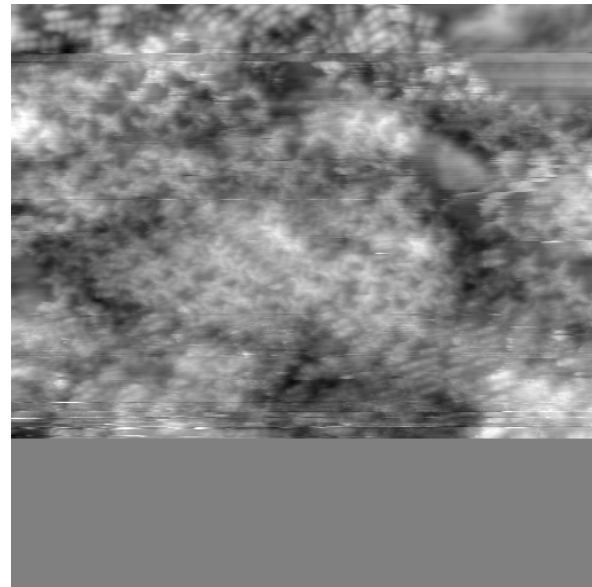


Figure 4.11: Position change of TPCN group members. Central molecule is manipulated, color indicates its initial (a, green hue in c) and final (b, red hue in c) position. Image (c) is created via an overlay of two sequential images. The upper and lower molecules do not shift thus sharing the same color.

TPCN without added cobald form similar pattern on the h-BN/Cu-foil system (compare fig. 2b in [144]). Although the ordered areas were quite rare, an ordered region has been found. Here the molecules are not strictly equi-distant or -rotated which makes it difficult to give an accurate unit cell for this type of motiv.



(a) Loosely ordered molecules on the h-BN/Cu-foil surface.

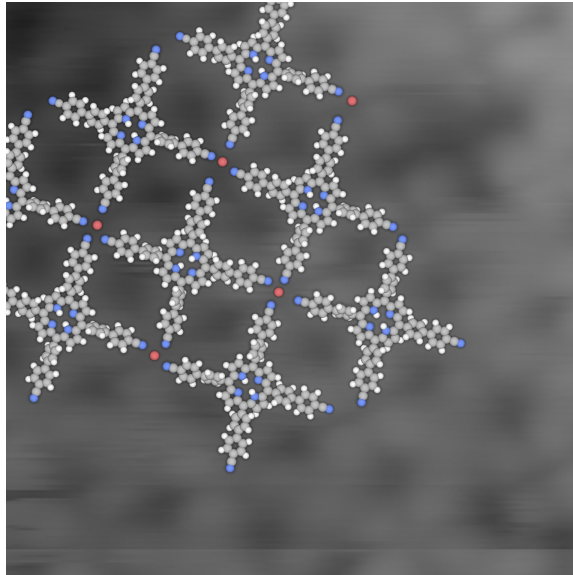


(b) Molecules do not always show ordering but in dense areas they do.

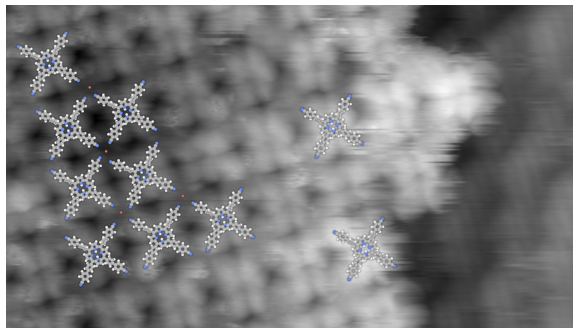
Figure 4.12: There they form a motif like in figure 4.11a).

Adding Co Introducing some cobald (15min, 90 °C) in the system, this self-assembly changes. The molecules now form a 2D network, too, but are further apart. Their only connection point to the other molecules is the tip of their legs pointing to the adjacent leg of the neighbouring molecule.

No sign for metallation (brighter center of porphine core) or cobald adatoms (bright spots in between the molecules) is observed. Because this type of binding is already reported [144], similar binding



(a) Zoomed view ($10 \times 10 \text{ nm}^2$)



(b) Zoomed view ($20 \times 35 \text{ nm}^2$)

Figure 4.13: Self-Assembled monolayer for TPCN on h-BN/Cu-foil. The cobalt atoms sit right in between the molecules and facilitate a regular, ordered arrangement of the TPCN.

mechanisms are derived for this system.

Molecules arrange periodically with center-center distances of about 2.3 nm. This leaves a little void space in between 4 TPCN molecule's legs, space where a Co atom may be located. This would result in a distance of 1.5 Å between the end of a TPCN leg (its N-center) and the center of the cobalt atom. Typical binding distances for Co-NC are reported [151, 152] and in good agreement.

4.6 Conclusion

5 Tert-Butyl-Phenyl Porphine

Within this section, TBP molecules with are investigated. The number (1-2) and position (single-, cis-, trans-configuration) of the very same functional group is changed. Although first the results on metal surfaces are presented, one of the ideas of the following experiments is to use the dipole moment of the single functionalized molecule to orient it along the work function change of a *h*-BN/Cu(111) sample. Please refer to section 3.3 for detailed information on these molecules.

Preparations with the single nitro functionalized species are done at RT on Cu(111), *h*-BN/Cu-foil and Ag(100). The Ag(100) preparation was heated to 170 °C.

Preparations with the trans functionalization are performed at RT on Ag(100) and Cu(111) where the last was heated to 120 °C.

Evaporation of the cis functionalization were not performed, although tried intensively no molecules were sublimated in the OMSE and found on the sample. This indicates strong intermolecular interaction within the crucible like cluster formation or polymerization, which have to happen before the molecules sublimate.

Similar molecules have been investigated on a reconstructed Au(111) surface [122].

5.1 Single leg functionalization

5.1.1 on Cu(111)

When adsorbed at room temperature, TBP distributes equally on the surface, forms unordered islands and decorates step edges. Molecules orient their main axis (connecting line from one di-tert-butyl-phenyl ring across the center to the nitrophenyl ring) along the dense packed substrate rows most often, less are 15° of ((Refer to image?)). Several binding motifs (as shown in Figure 5.2) are observed, namely

- A dimer, where molecules lie “head-to-head”, functional groups (NO_2) pointing at each other
- A “triangle”, where molecules are rotated 120° and functional groups point towards a shared center. Although this motif does not occur very often (or at least under very flexible angles), it is given as an example where the functional groups point to each other. Similar motifs (like 3 molecules in 90° are observed together with other orientations.
- Chains with different length appear, where the nitro group of molecule 1 points to the di-tert-butyl group of molecule 2 (“head-to-tail”). At the connection points, molecules appear brighter, promoting a physical overlap of the two molecules.

Center-center distances are typically 1.78 nm (for the head-to-tail) and 1.5 nm for the head-to-head connection.

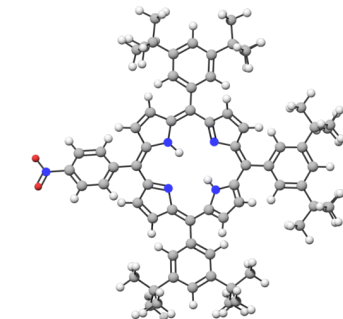


Figure 5.1: TBP with three di-tert-butyl and a single nitro phenyl group added at the meso position.

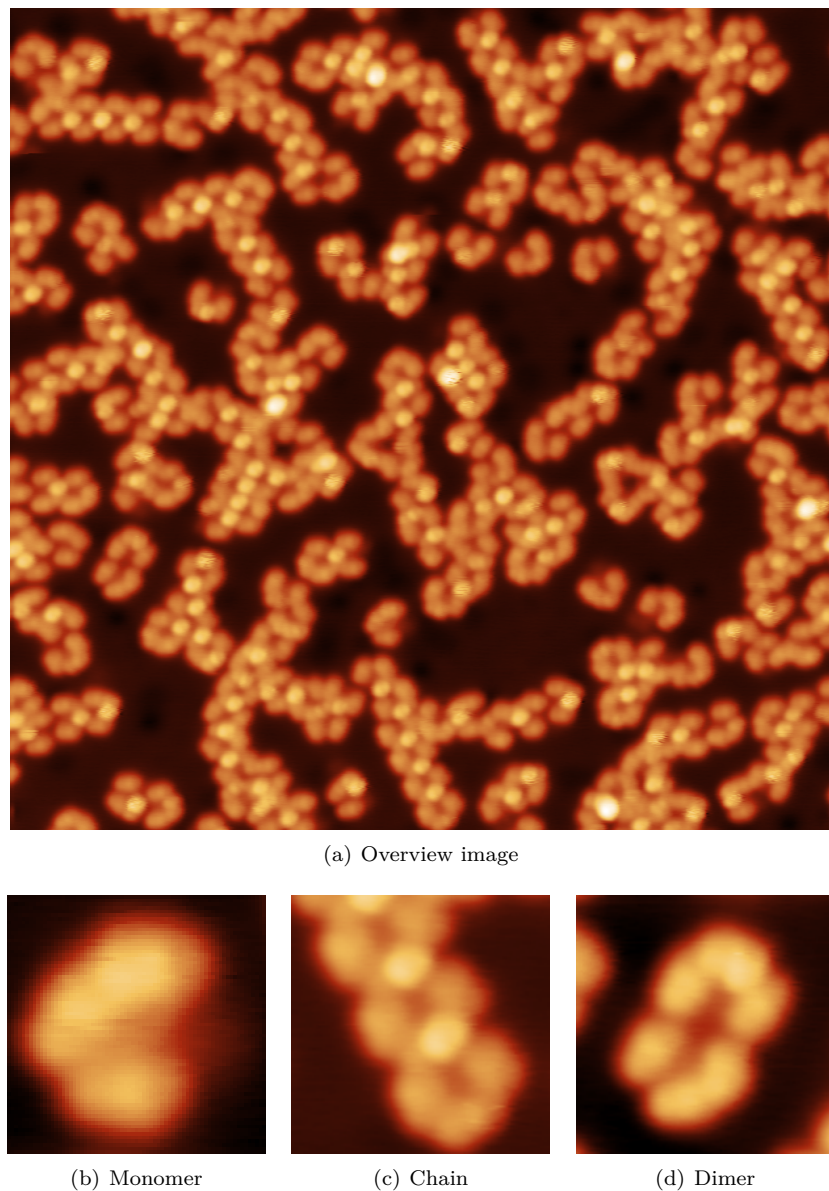


Figure 5.2: RT adsorbed single nitro functionalized TBP on Cu(111) and their most abundant binding motifs. (a) Each of the binding motif can be found as well in the overview STM data, as well as in the enlarged images (b-d). All images recorded with -500 mV , 0.1 nA , color scale 0 pm to 300 pm. Image width: (a) 44 nm, (b) 3 nm, (c) & (d) 5 nm

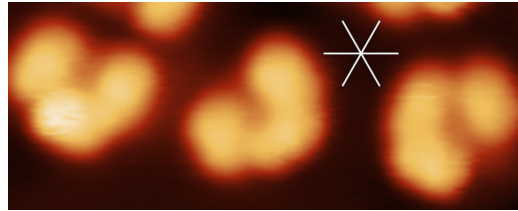


Figure 5.3: Different appearances of TBP on Cu(111). While most of monomers (center in image above) show even heights with their tert-butyl functions, some (left) do possess an elevated tert-butyl group. The orientation of the tert-butyl groups is aligned with the high symmetry crystal direction (indicated by white lines) most often. Image recorded with -500 mV , 0.1 nA . Image width: 10 nm

“head-to-head” To model the occurring binding motifs, deformations of the molecules have to be taken into account. Because nitro groups face each other in the “head-to-head” connection, their distance would be too small to facilitate a similar binding mechanism like for the TPCN on copper (where copper surface ad atoms promote binding between nitrogens), so no free space between the facing nitro groups is observed. Because the distance is so small, the phenyl ring (with attached nitro group) rotates by 45° , to make the phenyl ring stand upright. When the second molecule does the same, both match each other with negligible lateral shift, reproducing the STM images best. Similar binding motifs are reported in [153] for non-covalent cross linking of dicarboxylic acids in hydrogels. Although the situation on a metal-surface may change considerably (only 2D - no 3D, metal present - will change chemistry), the observed binding motif matches very well.

“head-to-tail” The chain motif “head-to-tail” is reconstructed using the unique contrast of the TBP molecule. When the center-center distance is measured, molecules are modeled that distance away from each other. These models show a physical overlap between molecules, which is not possible because of steric hindrance. To solve the problem, the nitro-group (head) of one molecule is rotated by 35° out of the plane (like pulling the nitro-group upwards, not rotating the group left/right).

Flexible tert-butyl-groups Another interesting fact is that butyl groups of TBP seem to orient them self (as far as steric hindrance allows for) along the dense packed rows of the copper substrate. Again, one has to be careful when reconstructing geometrical information from STM images. Like the distortion of legs in the TPCN molecule, this rotation can be explained by a rotation of single butyl groups. Although the phenyl ring remains at the same position/rotation, tert-butyl groups are allowed to rotate such that they appear in different heights. Because STM (constant current) follows equipotential lines, the whole phenyl-di-tert-butyl-complex looks rotated in plane, although it may not be. This is confirmed in literature[154, 155].

5.1.2 on Ag(100)

Molecules are adsorbed on Ag(100) at RT. The resulting conglomerates are shown in Figure 5.4(a). The very most surface area is covered with unregular patterns. The step edges are covered, assuming a sufficient large mobility at RT to move from the terrace to the nearest step edge. The only free step edges observed are due to tip formings on the sample surface since these are created after the molecules are stuck on the surface because of the low temperatures during measurement.

Annealing The RT adsorption is annealed to 170°C for 10 min and investigated in LT-STM again (Figure 5.4(b)). No big changes are visible, neither in the formation of new assemblies nor in the

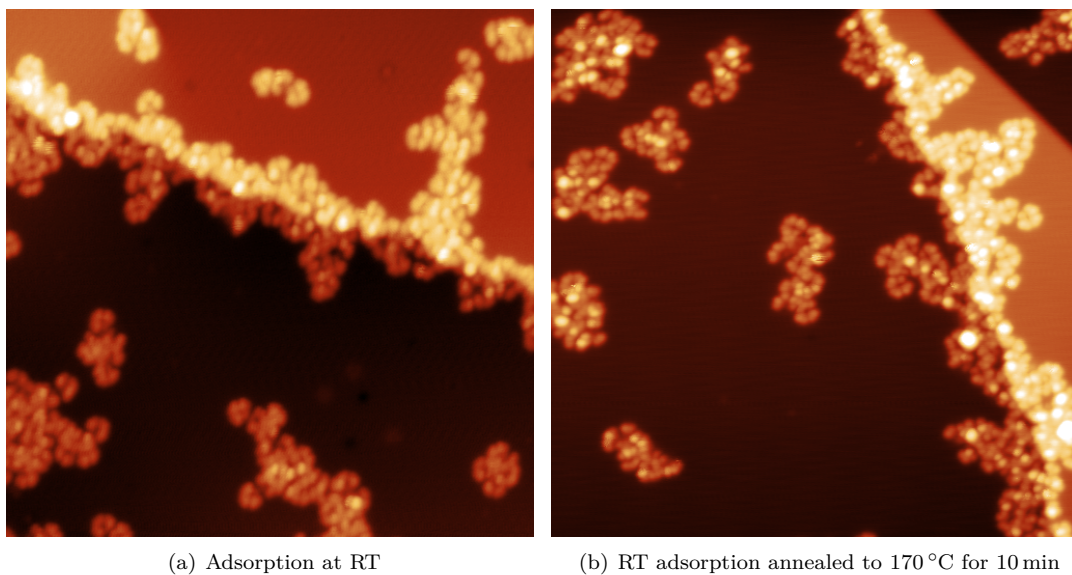


Figure 5.4: Annealing after RT adsorption of molecules on Ag(100). (a) STM data of molecules adsorbed at RT (Scan parameters: $U_b = 1$ V, $I_t = 0.03$ nA), (b) After annealing for 10 min to 170 °C (Scan parameters: $U_b = 1$ V, $I_t = 0.1$ nA). Color scale 0 pm to 600 pm. Image width: 44 nm.

distribution of molecules at terraces or at step edges. No chain formation could be observed.

Assembly Since no regular self-assembled islands are present on the surface, more detail is put on the only repeating binding motifs on this surface. One of this configurations resembles a cross (??), while the second one is a variation of the dimer motif (Figure 5.5).

While on copper, two molecules may form a dimer in head-to-head or head-to-tail configuration, on silver some form tetramers from two parallel merged dimers. While one dimer looks like two “U”’s with facing open ends ($\in \ni$), the other dimer is shifted to closely match the first dimer best and lies parallel.

Another motif looks like a cross and shown in Figure 5.5(f). Build out of four molecules, where each is rotated by 90° with respect to its preliminary neighbor. One can distinguish four di-tert-butyl groups from the central cross. Although there is no atom directly in the center, the cross looks bright in its center (in STM), which is somehow counterintuitive.

Flexible Tert-Butyl-Functions Figure 5.5(b) shows an interesting feature of the tert-butyl functions.

- Butyl groups within TBP feature different contrasts (look rotated), while the orientation of the butyl-groups doesn’t follow the close packed substrate rows. ————— find image and explain
- TBP molecules have been heated on silver substrate for 10 min at 170 °C. The resulting sample did not feature chain-formation or improved ordering.

Spectroscopy Some spectroscopy could be achieved that shows different typical features for different areas in the molecule. Note that the spectra were done for molecules sitting on a Ag(100) surface. There is a clear indication, that the macrocycle of the molecule contributes to the broad peak in the dI/dV data at around 1 V, while the nitro groups

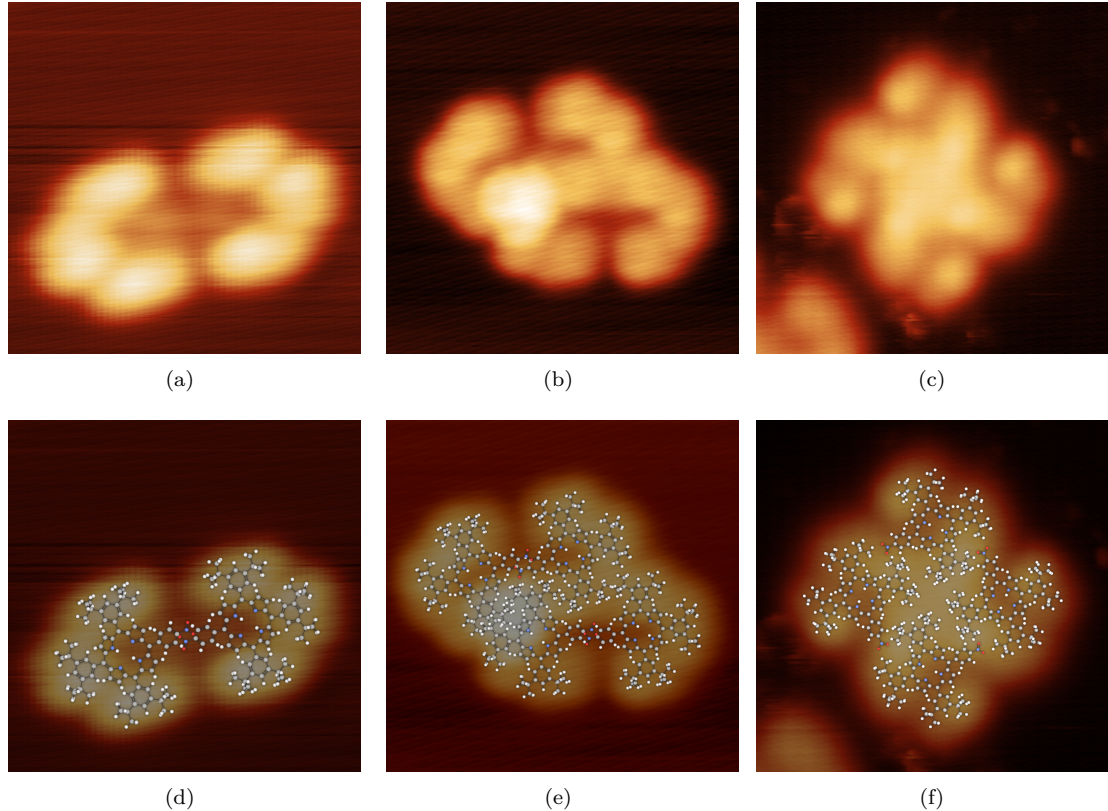


Figure 5.5: Different observed binding configurations of TBP adsorbed on Ag(100) at RT. (a) STM data of dimer configuration. Scan parameters: $U_b = 0.328$ V, $I_t = 0.035$ nA, Image width: 5 nm. (d) Model representation. (b) STM data of two coalescent dimers. Scan parameters: $U_b = 0.097$ V, $I_t = 0.035$ nA, Image width: 6 nm. (e) Model representation. (c) A cross consisting of four TBP molecules. Scan parameters: $U_b = 2.3$ V, $I_t = 0.035$ nA, Image width: 10 nm. (f) Model representation. Color scale in all STM images 0 pm to 300 pm

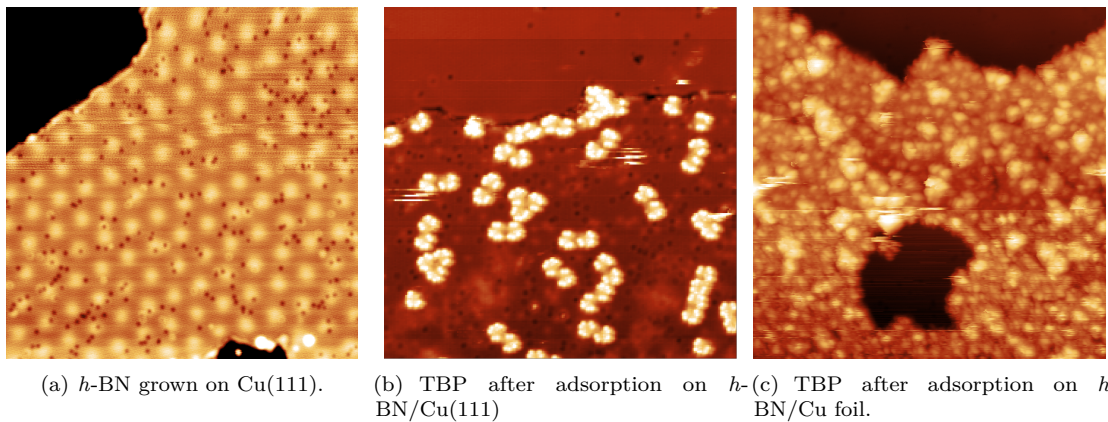


Figure 5.6: STM topographs of *h*-BN grown on copper with subsequent molecular adsorption. (a) shows a *h*-BN layer grown on Cu(111) by CVD. (b) shows the sample after evaporating TBP molecules at RT. (c) shows empty *h*-BN islands grown on the polycrystalline copper foil and molecules on a copper terrace. Scan parameters: (a) $U_b = 2.273$ V, $I_t = 0.048$ nA, color scale 0 pm to 100 pm. (b) $U_b = 1.074$ V, $I_t = 0.033$ nA, color scale 0 pm to 300 pm. (c) $U_b = 2.585$ V, $I_t = 0.032$ nA, color scale 0 pm to 1500 pm. All images are 40 nm wide.

dominate the spectra at around 600 mV. Look at the corresponding .pptx file for the spectra and the corresponding IGOR-files dimer/quatermer1-2 for the spectra.

5.1.3 on *h*-BN

***h*-BN grown on Cu(111)** Further experiments have been done to investigate the behavior of TBP on *h*-BN. When adsorbed on *h*-BN/Cu(111), molecules show a high mobility that makes the molecules move away from the *h*-BN islands. Some molecules could be resolved at defects or close to the perimeter of the *h*-BN islands. This is in line with other observations for adsorbates ((CITATION)). Adsorption temperatures as low as -170°C have been used to lower the molecules' energy pool, but diffusion to free metal areas occurs and no molecules remain on the *h*-BN surface.

***h*-BN grown on Cu-foil** Molecules adsorb on the BN surface and STM imaging is hard due to molecules that can be moved on the rather 'slippy' surface of the insulating BN. Nevertheless some agglomerations of the molecules leave free BN spots where no molecules are. As the preparation of the BN should result in a closed BN layer on top of the Cu-foil no movement of molecules to free Cu areas should be observed, making these free regions BN regions. Why the molecules are not distributed homogenously on the BN remains topic to speculation. Spectroscopy has been tried intensively but without reproducible results. Unlike the adsorption on Ag(100) and Cu(111) no formation of di- and quaterners has been observed.

5.1.4 Conclusion

The driving force for orienting the whole molecule on the surface remains speculative. On Ag(100), neither an orientation of the molecules main axis with respect to the substrate, nor a orientation of butyl-groups along the dense packed substrate rows can be

seen - which again favors Cu-substrate interactions as dominant role. When the copper is exchanged with silver to act as substrate, TBP behaves quite different. Although the distribution is homogeneous on the surface, the interaction between molecules look different. While on copper the most abundant binding motif is the head-to-head dimer, this motif does not appear on silver as often as on copper. Two other motifs emerge on silver. The interaction between the butyl-phenyl groups is considered to be van der Waals like [156], stabilizing the conglomerate.

5.2 Double leg functionalization

5.2.1 on Cu(111)

When depositing trans-TBP on Cu(111) at room temperature no long range ordering can be achieved. The molecules arrange rather arbitrarily as can be seen in Figure 5.7(a).

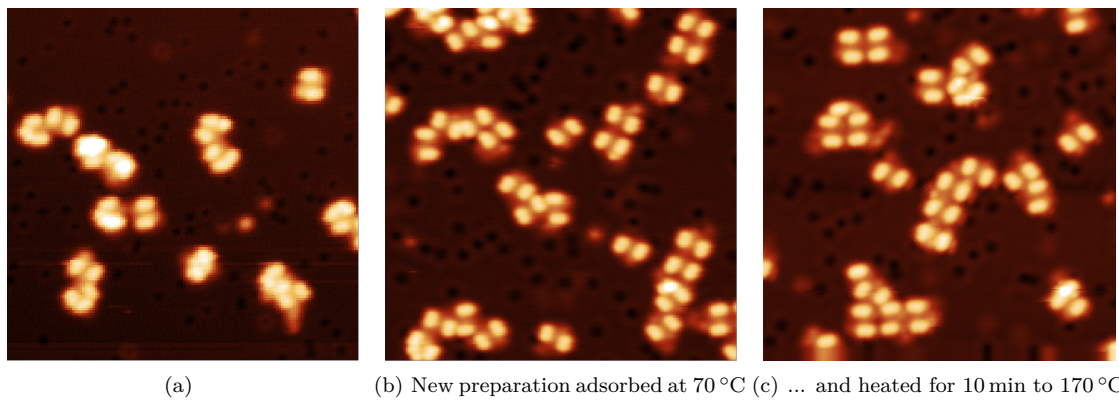


Figure 5.7: Molecules adsorbed on Cu(111) at RT and subsequently annealed to different temperatures. (a) Adsorption at room temperature did not show extended long range order. (b) Adsorption at 70 °C and (c) annealing to 170 °C for 10 min improves the chain length slightly. All images are 40 nm wide. Scan parameters: (a) $U_b = 1.2 \text{ V}$, $I_t = 0.041 \text{ nA}$, (b) $U_b = 0.5 \text{ V}$, $I_t = 0.038 \text{ nA}$, (c) $U_b = 0.522 \text{ V}$, $I_t = 0.021 \text{ nA}$

The molecules tend to connect in a defined angle to its next neighbor, forming different binding motifs. These are predominantly different kind of chain formation (see figure 5.8).

- The molecules are ordered such that they form a straight chain (Figure 5.9(a)).
- The molecules arrange in chains, but each molecule has an offset of about a half of its width to the next neighbor or the molecules attach in chains, but show a kink. Figure 5.8(b)

During modeling Figure 5.9 several points became clear.

- First consider the even apparent height of the di-tert-butyl groups. It indicates that both groups in a legs have comparable heights and it is likely that the phenyl ring bearing these groups is rotated for an even alignment of the tert-butyl groups with regard to the substrate level.
- Orientation of di-tert-butyl phenyl groups is the same within a single molecule but alternates (by $\approx 10^\circ$) in neighboring molecules in a chain. This is indicated by blue and green lines in Figure 5.9(a), each representing a common orientation.

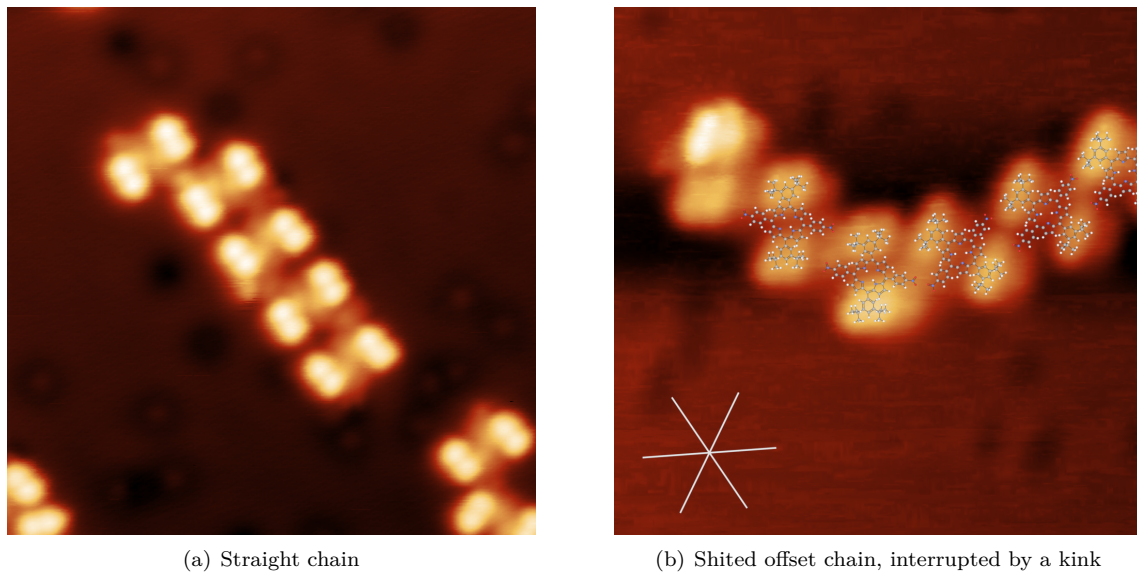


Figure 5.8: All motifs exist at every temperature, although the chain length increases with temperature. It also looks like the chains are getting more offset- and kinked-like chains than at lower temperatures.

- Second the minor contrast variations in the central porphine core change as the orientation of the di-tert-butyl-groups. Free base porphine core is likely to adsorb with its axis - formed by opposing nitrogens in the core - aligned parallel to the dense packed crystal direction[157]. In the present case, the molecule is lifted from the substrate by the bulky di-tert-butyl groups. Hence the porphine core interaction with the crystal substrate is considerably lower than in the 2H-P case. Still, every second molecule has the same orientation, while neighboring molecules are rotated by 30°.
- The gap between di-tert-butyl-phenyl groups of neighboring molecules is larger on one side of the chain than on the other and shows a larger apparent height (white arrows in Figure 5.9(a)). Although identification of surface ad-atoms is not straightforward with an STM, they are believed to originate from the copper surface.

The best fitting model consists of molecules with a center-center distance of 1.9(1) nm

Having a closer look to the nitro groups, one recognizes a close proximity of these to each other. Also note the light protrusions in between two adjacent molecules' butyl groups (adatom?). If the legs are rotated by just 15°, the nitro groups would point to these protrusions. This rotation costs not much energy and is about 25 kJ/permol ((please cite something, value is for rotated phenyl ring at a porphine core I guess)). Considering these protrusions as Cu-ad atoms (already occurred in chapter ?? as protrusions in between TPCN chains which may change their position in discrete position in the molecule.) This Cu-ad atom may direct the binding of the nitro groups towards it, making them bend outwards. The position of the copper atom itself may rely on its registry to the substrate - preferring a threefold coordination site as known for copper ((citation)).

The second motif is a chain motif, too. Orientation of molecular axis and dense packed substrate atom rows are the same and again the di-tert-butyl groups orient along them. The difference is a lateral offset between the molecules to shift each of them by half a molecule's width. The center-center distances are 1.9(1) nm. It is harder to quantify a possible orientation of the nitro-phenyl groups, since

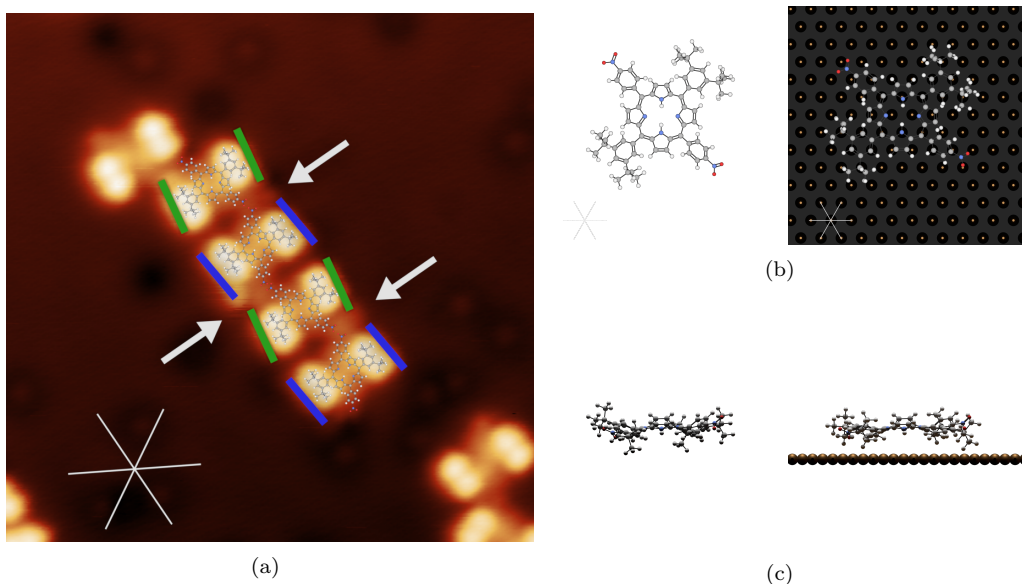


Figure 5.9: Straight chain binding motif on Cu(111). (a) shows an STM image together with the dense packed row indication of the substrate (white lines). Colored bars indicate the rotation of the di-tert-butyl-groups. Arrows point at places where ad-atoms are considered. (b) Top views (6 nm wide) showing the molecules geometry in gas-phase (left) and after adsorption and assembly (right). Although the exact adsorption site is not known, it is considered to be on a bridge site as for 2H-P/Cu(111). (c) Side views of above shown configurations.

as well straight as well as bended configurations match the assembly. In this binding motif, stable connections between molecules are most likely due to nitro-phenyl groups pointing to di-tert-butyl groups and therefore stabilizing the assembly.

5.2.2 on Ag(100)

Unit cell When adsorbed on a square (100) silver surface, the molecules interestingly arrange in a trihexagonal tiling (see figure 5.10). The molecules at the perimeter of this island are nicely distinguishable and continuing their regular pattern to the center of the island results in an accurate description of the assembly. The unit cell is determined to be _____ and the hexagonal unit cell is shown in Figure 5.10(b), bearing three molecules.¹

Molecular orientation The molecules are arranged so that each molecule has one of its di-tert-butyl-groups in one hexagonal pores and the other in the neighboring one. Each pore is made up of six molecules arranged on a hexagon with _____ long edges. Each vertex is occupied by a single molecule, neighboring molecules on the hexagon are rotated by 60°. The pores are created by free space where the di-tert-butyl-groups point towards each other. The nitro-phenyl groups point towards the intermediate space where smaller triangular openings are formed. At their edges the nitro-phenyl groups connect to the neighboring di-tert-butyl groups.

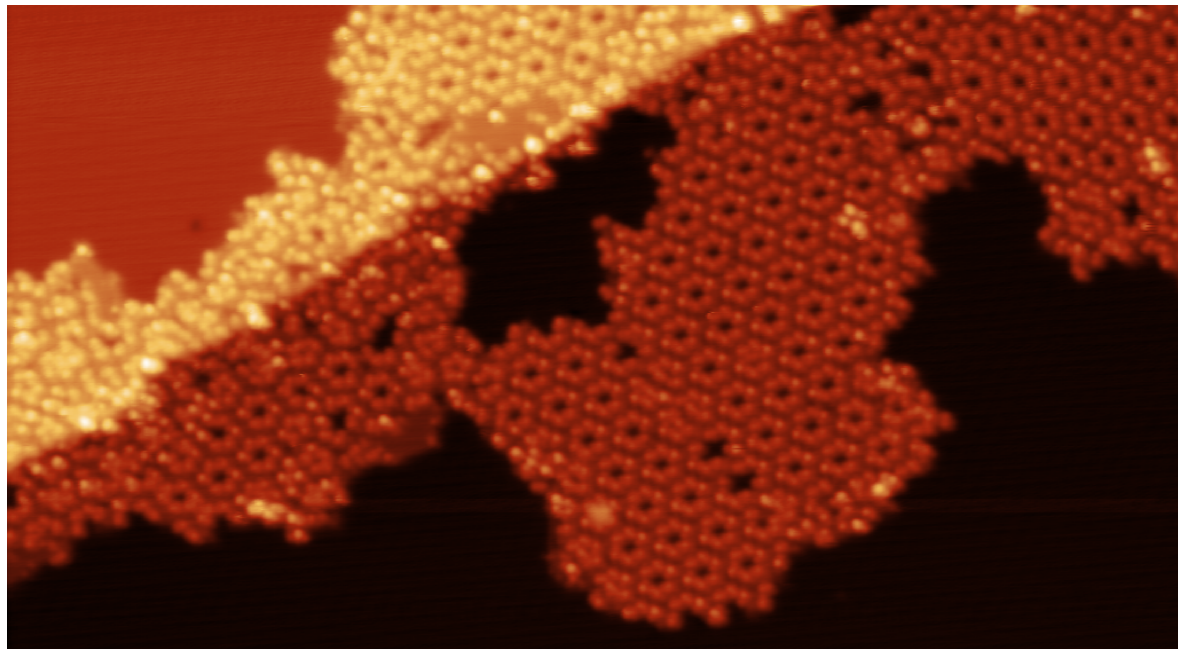
Considering a former orientation calibration on Ag(100) where the direction of the dense packed crystal direction was determined, the orientation with regard to the substrate is given as white lines

¹Similar open porous network can be created, e.g. cyano functionalized triarylaminies on Au(111) [158].

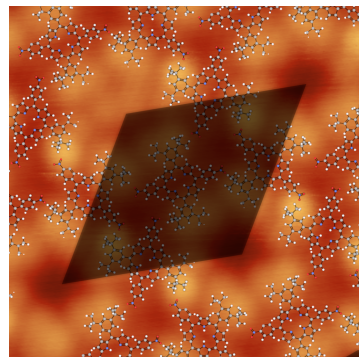
in Figure 5.10(b): The long and short axis of the unit cell (marked as green cross in (b)) is almost collinear, just differing by less than 10°. Since the calibration was done with another preparation the angle calibration may not be 100 % accurate because the sample was moved in the meantime. That may result in a little angle uncertainty. Please see Figure 8 in section 4 Ordered areas of TBP for a detailed image.

Contrast within single molecule A closer look to the geometries in high resolution STM data gives clue to the rotation of the di-tert-butyl-groups and is visualized in Figure 5.10(c). Focusing on the STM contrast of a single molecule, one can see that it is dominated by the di-tert-butyl-groups on both sides of the molecule. These look like small triangles in the STM with a single brighter protrusion enclosed by the footprint. The bright protrusion is never on the same side of the triangular footprint thus the di-tert-butyl-groups are believed to be rotated in two different directions - lifting opposite parts of the functional group.

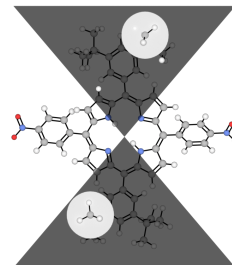
Domain boundaries The observed domain boundaries are imaged in Figure 5.11. On both sides the regular tiling is proceeded, but both are shifted with respect to each other by _____. This offset results in the wrong alignment of molecules from one domain with respect to the other domain and a discontinued growth. The resulting free area at the domain boundary is occupied by molecules from one domain that bear the wrong orientation the proceed the growth of the second domain and vice versa. This can be nicely seen in Figure 5.11(c), where the misalignment of one domain (left) with respect to the other (right) causes two cavities to open up between the two (lower image part). While these two are unoccupied and reveal the substrate, another type of cavity can be formed directly seen on top of the two aforementioned. Here the cavity is filled with a single molecule so that both di-tert-butyl groups interlock with the open cavity. Please note that some of the assembly pores are filled, too. Here the space of the pore prohibits a complete molecule to fit in, the observed adsorbates in the pores are most likely molecular fragments like tert-butyl-groups that were incorporated by the assembly during the island growth.



(a) STM topography of several islands grown next to a step edge. Areas with trihexagonal tiling as well as some domain boundaries are visible.



(b) Hexagonal unit cell with overlaid molecular models.



(c) Enlarged view on the molecules rotated di-tert-butyl-group and highest elements enclosed by brighter circles..

Figure 5.10: Trans-TBP adsorbed on Ag(100) at room temperature. (a) shows a large overview of the assembled molecules. The unit cell constituents are enlarged in (b) where parts of (a) are shown with molecular models overlaid. (c) shows a single molecule crossing a horizontal plain to emphasize high lying part in the molecule that are marked with white circles and will appear brighter in STM. All images recorded with 437 mV, 0.1 nA, color scale 0 pm to 650 pm

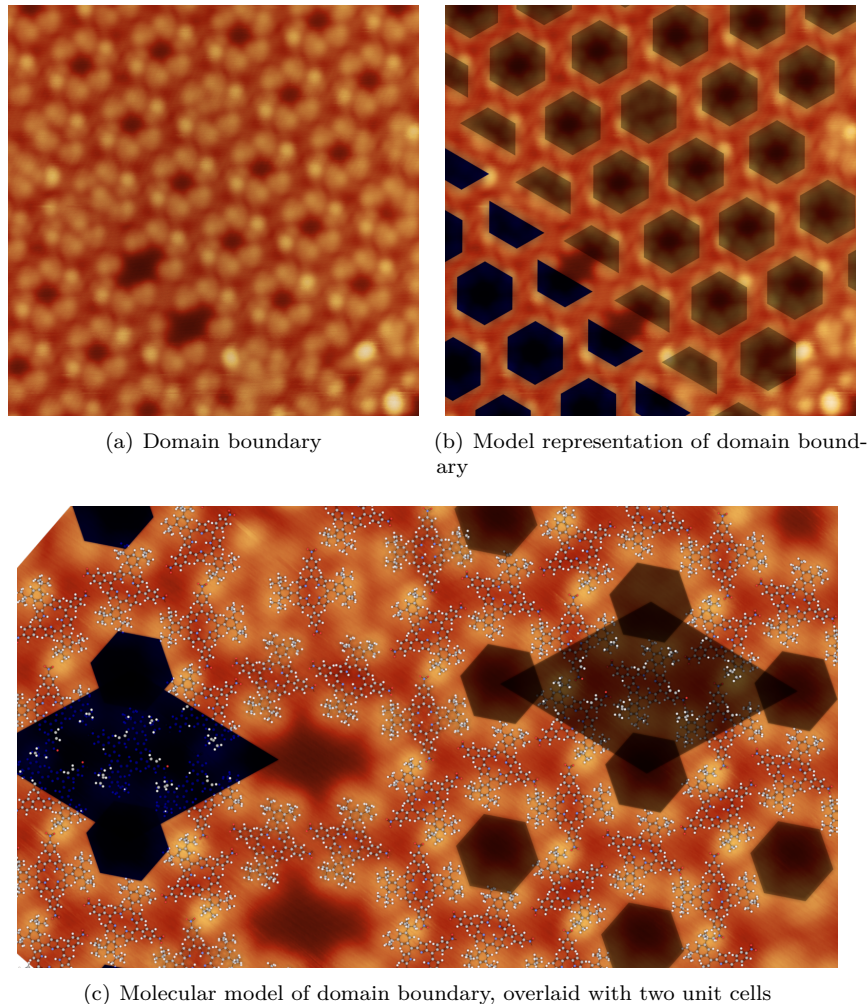


Figure 5.11: Domain boundary of trans-TBP adsorbed on Ag(100) at RT. (a) shows an overview of the domain boundary together with its model representation in (b). The assembly close by is modeled in (c) where parts of (a) are shown and molecular models overlaid. All images recorded with 1.3 V, 0.1 nA, color scale 0 pm to 650 pm

6 Borazine functionalized coronene

Coronene ($C_{24}H_{12}$, known as [6]circulene or superbenzene) is a polycyclic aromatic hydrocarbon made of six carbon rings to form a molecule reminiscent of a small graphene flake. It belongs to the family of circulenes where a central polygon is enclosed by different numbers of fused benzenoids. For example [5]circulene (corannulene), [6]circulene (coronene), [7]circulene,[2][3][4][5] and higher orders could be synthesized and show different conformation. While species with [5] or [7] benzene rings are bowl shaped, coronene is flat.

6.1 Find a nice title!

HBC and HBBNC are modifications of coronene. First, for both species six benzo groups are added to form a larger molecular backbone. For both species three 2,6-Dimethylphenyl groups are added to extend the molecule that now resembles a triangular footprint. While HBC features a central carbon ring, HBBNC is functionalized with a central borazine ring instead. Both species have the same number of atoms and molecular weight. The difference between both becomes apparent when electronic properties are compared (in gas phase).

The regular covalent sp^2 hybridization results in an evenly distributed electron density in HBC where the central region of the molecule shows considerable depletion. Changing the central carbon ring to a borazine ring changes the electron density. Now electrons are redistributed from the coronene parts towards the central borazine ring. Because the bond between B and N shows an added ionic character the aromacity is interrupted and the extended electron pi system is altered. Comparable to the difference between graphene (perfect C-C bonds, conductor) and h-BN (Ionic B-N bonds, insulator) the band gap present for HBC is 0.4 eV smaller than for HBBNC, changing its optoelectronic properties.

The present functionalization of the coronene molecule is twofold. Di-Methylphenyl groups are added to guide the formation of self-assembled islands of the molecule on the surface. The functionalized core of the molecule is used to create an adsorption platform for polar molecules.

After RT adsorption of HBBNC on Ag(111) different assemblies are found. For low coverage the dominating pattern is a hexagon made up of six molecules in two different orientations with respect to the substrate. Although the molecule is not chiral in gas phase, adsorption on the Ag(111) surface leads to the formation an mirror image and therefore a second type of hexagon. The internal structure of these hexamers can be revealed to lateral manipulation of a hexamer with the STM tip. Three things can be concluded: 1. A hexagon is made up of six intact molecules with alternating orientations, 2. The bright features between two neighboring molecules can be attributed to rotated dimethylphenyl rings. This only occurred when two molecules are close to each other and show the right rotation, 3. Molecules not incorporated in a hexamer appear flat with no pronounced apparent height above the legs.

From the observation of smaller hexamer fragments, it seems like the growth mechanism of the hexamers is already fixed in an early state of the assembly and depends on the adsorption site of the

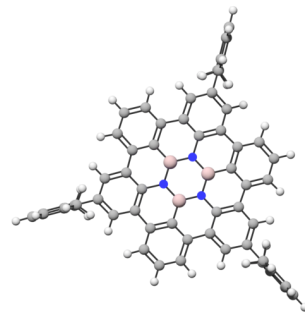


Figure 6.1: HBBNC

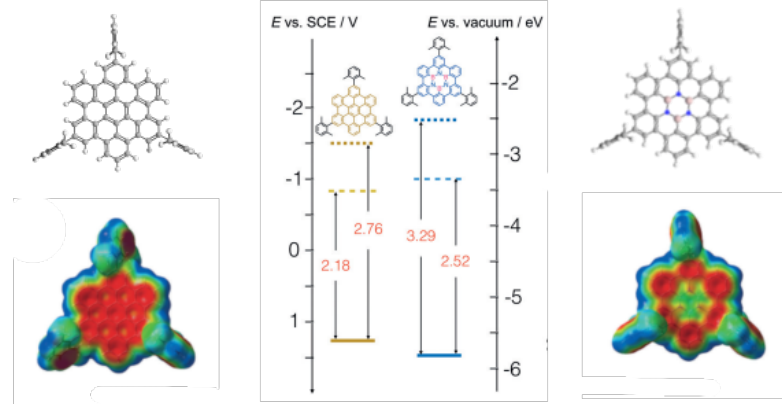


Figure 6.2: Taken from [138]

second molecule attaching to the first. Two neighboring molecules never show the same orientation and connect to each other with parallel edges, slightly shifted. Molecule by molecule than arranges to match the steric restrictions from the already formed hexamer. This efficient guiding mechanism leads to most molecules finish hexamer assemblies. Besides the dominant motif monomers, dimers and smaller agglomerations are observed, too.

The electronic structure of single HBBNC molecules is investigated with STS after disassembly of a hexamer into its comprising single molecules. There is a pronounced electronic feature around 650 mV on the molecular center, features at 1200 mV and 1600 mV can be attributed to the leg and edge positions respectively. The surface state of the substrate (-50mV next to the molecule) vanishes/shifts below the molecule. The calculated band gap of 2.52 eV is not observed directly because ... The fact that the band gap is not symmetric around the Fermi energy is because.... Charge transfer between molecule and substrate is possible? What would be the result? Calculate! Why/how does the surface state shift?

Increasing the coverage leads to a new assembly being formed. Besides hexamers alongside their chiral counterpart form on the surface (solid and dashed blue circle), chains of dimers assemble in islands. Within these, dimer chains exist in two different orientations (solid and dashed green boxes) and are separated by single molecules (see supporting information). These chains are oriented along the high symmetry directions of the substrate and 30° off. Molecular orientation within the chains is slightly different than in the hexamer assemblies. Here molecules attach with a smaller lateral shift to form linear chains. Tell about binding distances and unit cell. The protrusions between two neighboring molecules can be attributed to a rotation of the leg functionalization to avoid steric hindrance and to stabilize the assembly. A second new binding motif is observed (white square). It is made up of four molecules, whose close proximity in the center form pattern reminiscent of a clover-leaf. It can be seen that (in contrast to hexamers) molecules can attach to the rims and evolve into more extended structures.

Further increasing the coverage results in dense regions being formed. The dominating pattern is the clover-leaf rarely observed in the medium coverage phase. It is present here in two different

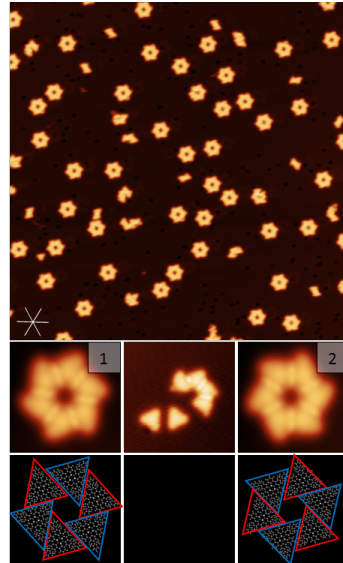


Figure 6.3

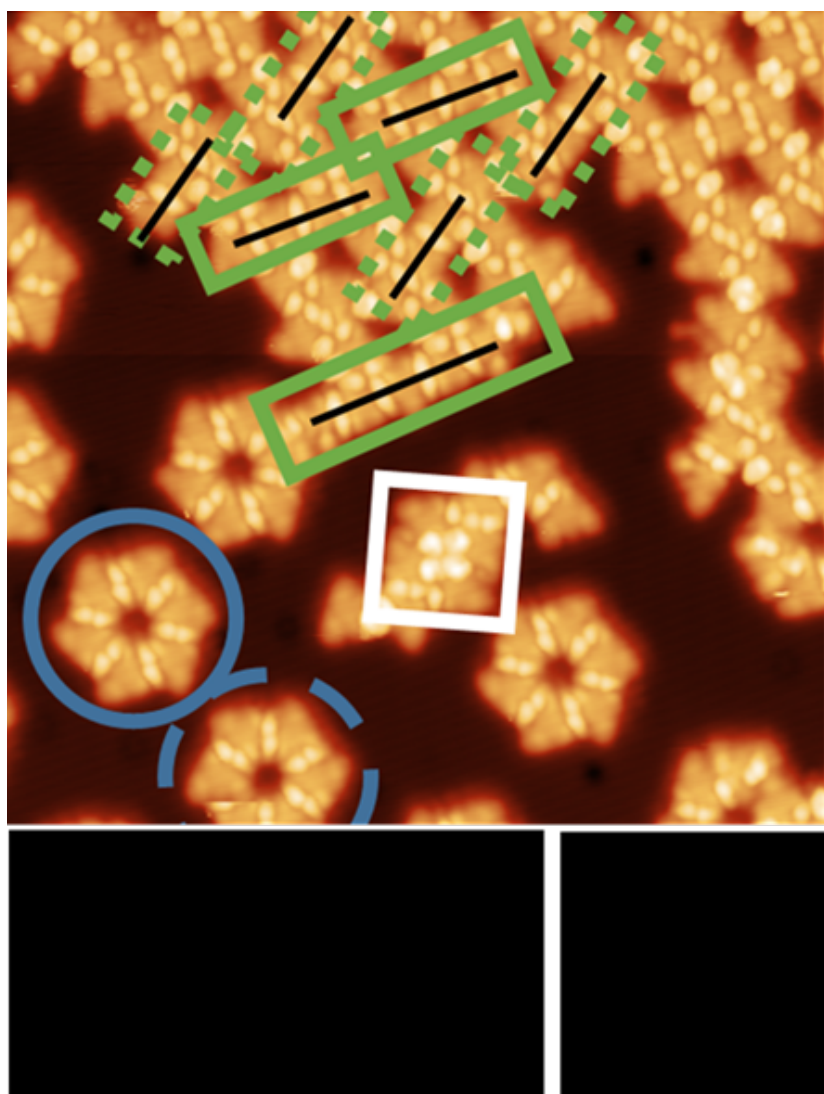


Figure 6.5

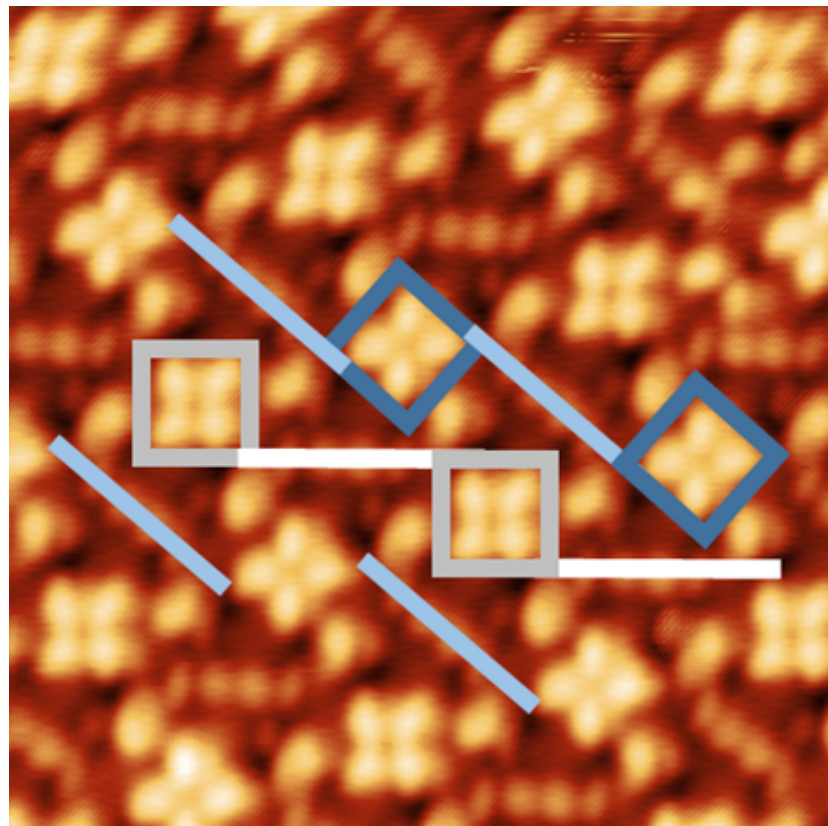


Figure 6.6

orientations (white and blue box) and distributed such that neighboring squares do not show the same orientation. Two squares with the same orientation (white/blue) are separated by lines made up of four bright spots aligned parallel to the square edge. Squares with different rotations do not show these connections between them, but a single protrusion with larger apparent height. Binding motif, binding distances.

A sample prepared at RT has been annealed to 350 °C and 420 °C.

After the sample is annealed to 350°C only monomers and few random agglomerates are imaged on the surface. Although the molecules undergo the same temperature range where hexamers are formed (from RT to 5K) no regular assembly is imaged. Because the assembly is guided by the presence of the dimethylphenyl group a closer look to the molecular conformation is taken. Three different types can be distinguished. 1: Flat molecules, 2: Molecules with a single protrusion close to the leg position, 3: Molecules with a leg missing. The unstable imaging conditions above some of the molecules legs indicate their flexibility while the others seem to be rigidly connected to the molecular backbone and therefore imaged stable. The vanishing hexagon binding motif - observed for the un-annealed sample - underpins the importance for the molecules leg to adopt the assembly. This flexibility of all legs is not present any more after annealing to 350°C and hexamer formation is suppressed. Molecular orientation? Increasing the annealing temperature to 420°C results in a percolated network where monomers present at 350°C coalesce and connect via their legs. Lateral manipulation attempts have been done, showing a stiff connection between neighboring molecules. Opposing to the previous preparations, the assembly could not be divided into single monomers. This rigid connection indicates a covalent coupling of the molecules. Molecular orientation?

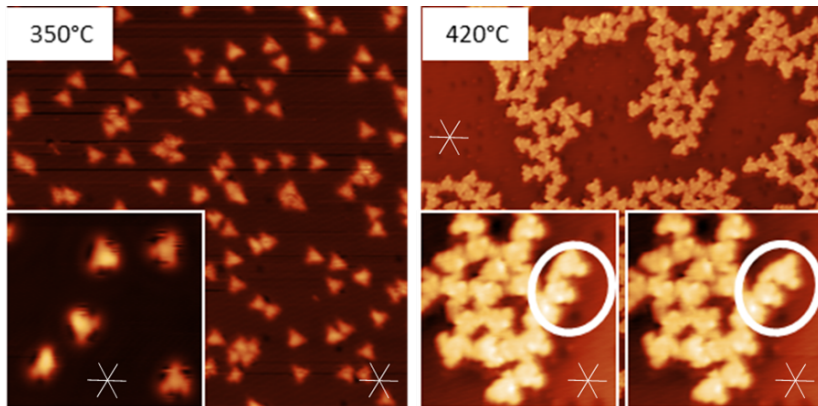


Figure 6.7

Since the formation of a new bond is expected to change the core levels of participating elements (Carbon, C 1s), XPS measurements are done and presented in the following.

Preparations have been done to further investigate the connection between molecules annealed to 420°C. Sub-ML as well as multilayer preparations have been annealed to 420°C to quantify the change in binding energy. After RT deposition of a sub-ML HBBNC on Ag(111) a single C 1s peak is observed that grows with increasing coverage but maintains its position. Is there no shift after adsorption of a multilayer? After annealing a multilayer preparation the C 1s position shifts to lower binding energies by (~1eV), a behavior typical for cyclodehydrogenation and ring closure reactions of e.g. porphins (CITATION). What are other mechanisms for a shift towards lower binding energies => screening should change in monolayer/multilayer regimes? The area below the peak drops to a sub-ML coverage, a clear indication for desorption of the second and third layer. A covalently coupled layer would not desorb, so coupling in the lowest layer takes place after multilayer desorption. It can be concluded that annealing HBBNC on a Ag(111) surface leads to the formation of a covalent network stabilized via covalent bonds formed across the legs.

To further check the conformational changes in the molecule after annealing, AFM measurements are done. nc-AFM has the big advantage over STM that it is less sensible to electronic changes in the molecule – more closely resembling the true geometric shape.

Nc-AFM measurements are a complementary method to investigate the molecules before and after annealing to 420°C.

Before annealing Before annealing the adsorption geometry of monomers is investigated. By scanning the same molecule in different heights, elevated parts of the molecule can be easily distinguished by their larger interaction force with the tip (the involved larger frequency shift is shown as protrusion in nc-AFM images). In contrast to STM measurement where no obvious change in apparent height was observed at RT between legs, AFM measurements show that the dimethylphenyl legs of a monomer do not lie flat on the surface but have an elevated and lower lying part. While the initial orientation on the surface is likely determined at adsorption, the legs are able to rotate under the influence of the

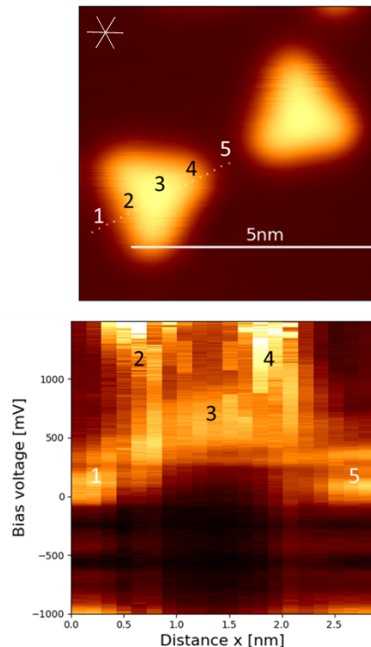


Figure 6.4

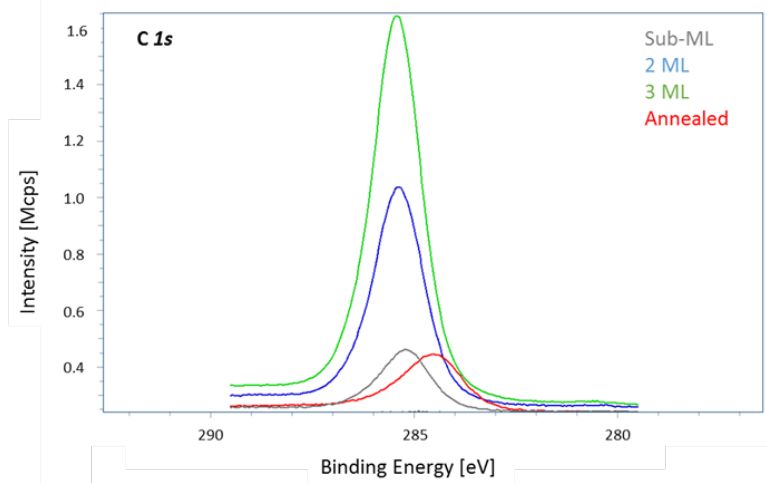


Figure 6.8

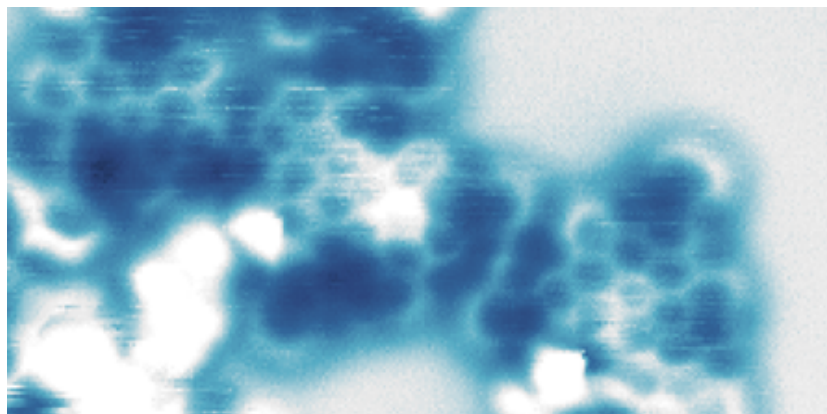


Figure 6.9

AFM tip (see SI).

After annealing IS that a bond? What does the contrast mean? CITE; CITE, CITE The triangular molecules that appeared flat in STM (after annealing to 420°C) reveal their interesting geometric properties when investigated by means of nc-AFM. It is observed that many of the molecules appear to have their dimethylphenyl groups aligned planar to the surface. A behavior expected for a ring closure reaction between the hexabenzol groups and dimethylphenyl legs. EXAMPLES for AFM showing that in other systems. In the present case, almost all molecules showed some defined contrast in the connection region. DISCUSS distances, directions and excess of carbon rings. When the legs rotate parallel to the surface, the molecular backbone comes closer to the metal => charge transfer/screening and such things!!

To have the molecule adsorbed more even on the surface, another substrate is chosen. Silver is known to have a larger impact on adsorption geometries than Au(111) has (bowl shape of PAH on Ag(111) => CITE!).

In contrast to adsorption on Ag(111) where almost all molecules are incorporated into hexamers, molecules separate into monomers on Au(111). Molecules follow the herringbone reconstruction visible

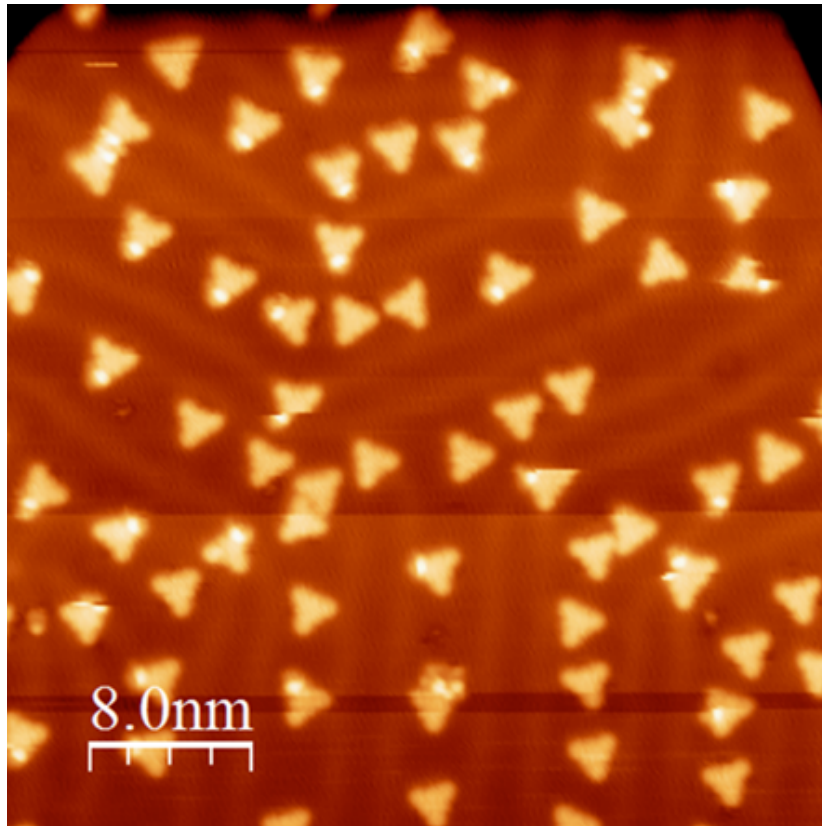


Figure 6.10

as bright stipes in the STM image. (These divide the surface into regions of fcc and hcp reconstruction. Which one is broad, which one is small) Molecules show two different appearances. While some appear to adsorb flat in STM, others already show a protrusion above one of their legs. This protrusion is not caused by parts of the herringbone reconstruction, two molecules on very similar adsorption sites within the reconstruction show different appearances. What are conformational changes here?

HBC It is reported that for HBC, no stable second layer of molecules can be found for a strong electron donor like HBC [159].

7 Summary

This is intentionally for all nice little things which does not certainly make it into this work: [32]

Bibliography

- [1] Gerd Binnig et al. “7x7 reconstruction on Si (111) resolved in real space”. In: *Physical review letters* 50.2 (1983), p. 120. URL: <http://journals.aps.org/prl/abstract/10.1103/PhysRevLett.50.120> (visited on 07/16/2015).
- [2] *The Bartynski Group*. 2006. URL: <http://www.physics.rutgers.edu/Bartgroup/STM.htm> (visited on 08/10/2018).
- [3] Manuela Garnica. “Electron acceptor molecules deposited on epitaxial graphene studied by means of low temperature scanning tunneling microscopy / spectroscopy”. PhD thesis. Madrid: Universidad Autonoma de Madrid, July 1, 2013. 138 pp.
- [4] Michael Schunack. “Scanning Tunneling Microscopy Studies of Organic Molecules on Metal Surfaces”. PhD thesis. Denmark: University of Aarhus. 180 pp.
- [5] Samir Lounis. “Theory of Scanning Tunneling Microscopy”. In: *arXiv:1404.0961 [cond-mat]* (Apr. 3, 2014). arXiv: 1404.0961. URL: <http://arxiv.org/abs/1404.0961> (visited on 08/09/2018).
- [6] Daniel Wortmann. “Interpretation of Scanning Tunneling Microscopy and Spectroscopy of Magnetic Metal Surfaces by Electron Theory”. PhD thesis. Dortmund: Universit\at Dortmund, 2000. 100 pp. URL: www.fz-juelich.de/SharedDocs/Downloads/PGI/PGI-1/EN/Wortmann.dipl_pdf.pdf?__blob=publicationFile (visited on 08/23/2018).
- [7] Dawn A. Bonnell, ed. *Scanning tunneling microscopy and spectroscopy: theory, techniques, and applications*. New York, N.Y: VCH, 1993. 436 pp. ISBN: 978-0-89573-768-7.
- [8] Gregor Wentzel. “Eine Verallgemeinerung der Quantenbedingungen für die Zwecke der Wellenmechanik”. In: *Zeitschrift für Physik* 38.6 (June 1926), pp. 518–529. ISSN: 1434-6001, 1434-601X. DOI: 10.1007/BF01397171. URL: <http://link.springer.com/10.1007/BF01397171> (visited on 08/23/2018).
- [9] H. A. Kramers. “Wellenmechanik und halbzahlige Quantisierung”. In: *Zeitschrift für Physik* 39.10 (Oct. 1926), pp. 828–840. ISSN: 1434-6001, 1434-601X. DOI: 10.1007/BF01451751. URL: <http://link.springer.com/10.1007/BF01451751> (visited on 08/23/2018).
- [10] Léon Brillouin. “La mécanique ondulatoire de Schrödinger: une méthode générale de resolution par approximations successives”. In: *Comptes Rendus de l'Académie des Sciences* 183 (1926), pp. 24–26.
- [11] P. Sautet and C. Joachim. “Interpretation of STM images: copper-phthalocyanine on copper”. In: *Surface Science* 271.3 (Jan. 1992), pp. 387–394. ISSN: 00396028. DOI: 10.1016/0039-6028(92)90902-I. URL: <http://linkinghub.elsevier.com/retrieve/pii/003960289290902I> (visited on 07/13/2015).
- [12] J. Tersoff and D. R. Hamann. “Theory of the scanning tunneling microscope”. In: *Physical Review B* 31.2 (Jan. 15, 1985), pp. 805–813. ISSN: 0163-1829. DOI: 10.1103/PhysRevB.31.805. URL: <https://link.aps.org/doi/10.1103/PhysRevB.31.805> (visited on 08/23/2018).
- [13] N. D. Lang. “Theory of Single-Atom Imaging in the Scanning Tunneling Microscope”. In: *Physical Review Letters* 56.11 (Mar. 17, 1986), pp. 1164–1167. ISSN: 0031-9007. DOI: 10.1103/PhysRevLett.56.1164. URL: <https://link.aps.org/doi/10.1103/PhysRevLett.56.1164> (visited on 08/23/2018).

- [14] D. M. Eigler et al. “Imaging Xe with a low-temperature scanning tunneling microscope”. In: *Physical Review Letters* 66.9 (Mar. 4, 1991), pp. 1189–1192. ISSN: 0031-9007. DOI: 10.1103/PhysRevLett.66.1189. URL: <https://link.aps.org/doi/10.1103/PhysRevLett.66.1189> (visited on 08/23/2018).
- [15] R. M. Tromp, R. J. Hamers, and J. E. Demuth. “Atomic and electronic contributions to Si (111)-(7x7) scanning-tunneling-microscopy images”. In: *Physical Review B* 34.2 (1986), p. 1388. URL: <http://journals.aps.org/prb/abstract/10.1103/PhysRevB.34.1388> (visited on 07/16/2015).
- [16] R.M. Feenstra, Joseph A. Stroscio, and A.P. Fein. “Tunneling spectroscopy of the Si(111)2 Å“ 1 surface”. In: *Surface Science* 181.1 (Mar. 1987), pp. 295–306. ISSN: 00396028. DOI: 10.1016/0039-6028(87)90170-1. URL: <http://linkinghub.elsevier.com/retrieve/pii/0039602887901701> (visited on 07/17/2015).
- [17] R. S. Becker, J. A. Golovchenko, and B. S. Swartzentruber. “Electron interferometry at crystal surfaces”. In: *Physical review letters* 55.9 (1985), p. 987. URL: <http://journals.aps.org/prl/abstract/10.1103/PhysRevLett.55.987> (visited on 07/17/2015).
- [18] J. F. Jia et al. “Variation of the local work function at steps on metal surfaces studied with STM”. In: *Physical Review B* 58.3 (July 15, 1998), pp. 1193–1196. DOI: 10.1103/PhysRevB.58.1193. URL: <http://link.aps.org/doi/10.1103/PhysRevB.58.1193> (visited on 07/22/2015).
- [19] K. H. Gundlach. “Zur berechnung des tunnelstroms durch eine trapezförmige potentialstufe”. In: *Solid-State Electronics* 9.10 (Oct. 1966), pp. 949–957. ISSN: 0038-1101. DOI: 10.1016/0038-1101(66)90071-2. URL: <http://www.sciencedirect.com/science/article/pii/0038110166900712> (visited on 07/22/2015).
- [20] G. Binnig et al. “Tunneling Spectroscopy and Inverse Photoemission: Image and Field States”. In: *Physical Review Letters* 55.9 (Aug. 26, 1985), pp. 991–994. DOI: 10.1103/PhysRevLett.55.991. URL: <http://link.aps.org/doi/10.1103/PhysRevLett.55.991> (visited on 07/22/2015).
- [21] C. L. Lin et al. “Manifestation of Work Function Difference in High Order Gundlach Oscillation”. In: *Physical Review Letters* 99.21 (Nov. 20, 2007), p. 216103. DOI: 10.1103/PhysRevLett.99.216103. URL: <http://link.aps.org/doi/10.1103/PhysRevLett.99.216103> (visited on 07/22/2015).
- [22] E. Fermi. “Zur Quantelung des idealen einatomigen Gases”. In: *Zeitschrift für Physik* 36.11 (Nov. 1926), pp. 902–912. ISSN: 1434-6001, 1434-601X. DOI: 10.1007/BF01400221. URL: <http://link.springer.com/10.1007/BF01400221> (visited on 08/23/2018).
- [23] P. A. M. Dirac. “On the Theory of Quantum Mechanics”. In: *Proceedings of the Royal Society A: Mathematical, Physical and Engineering Sciences* 112.762 (Oct. 1, 1926), pp. 661–677. ISSN: 1364-5021, 1471-2946. DOI: 10.1098/rspa.1926.0133. URL: <http://rspa.royalsocietypublishing.org/cgi/doi/10.1098/rspa.1926.0133> (visited on 08/23/2018).
- [24] C. Julian Chen. *Introduction to scanning tunneling microscopy*. 2nd ed. Monographs on the physics and chemistry of materials 64. Oxford ; New York: Oxford University Press, 2008. 423 pp. ISBN: 978-0-19-921150-0.
- [25] Paul K. Hansma, ed. *Tunneling spectroscopy: capabilities, applications, and new techniques*. New York: Plenum Press, 1982. 493 pp. ISBN: 978-0-306-41070-3.
- [26] J. Tersoff. “Role of tip electronic structure in scanning tunneling microscope images”. In: *Physical Review B* 41.2 (1990), p. 1235. URL: <http://journals.aps.org/prb/abstract/10.1103/PhysRevB.41.1235> (visited on 07/17/2015).
- [27] S. Ciraci, A. Baratoff, and Inder P. Batra. “Tip-sample interaction effects in scanning-tunneling and atomic-force microscopy”. In: *Physical Review B* 41.5 (1990), p. 2763. URL: <http://journals.aps.org/prb/abstract/10.1103/PhysRevB.41.2763> (visited on 07/17/2015).

- [28] D. Lawunmi and M. C. Payne. “Theoretical investigation of the scanning tunnelling microscope image of graphite”. In: *Journal of Physics: Condensed Matter* 2.16 (1990), p. 3811. URL: <http://iopscience.iop.org/0953-8984/2/16/011> (visited on 07/17/2015).
- [29] Katsuyoshi Kobayashi. “Simulation of scanning tunneling microscope image based on electronic states of surface/tip system”. In: *Journal of Vacuum Science & Technology A: Vacuum, Surfaces, and Films* 8.1 (Jan. 1990), p. 170. ISSN: 07342101. DOI: 10.1116/1.577057. URL: <http://scitation.aip.org/content/avs/journal/jvsta/8/1/10.1116/1.577057> (visited on 07/17/2015).
- [30] J.C. Rivière. “Instrumentation”. In: *Auger and X-ray Photoelectron Spectroscopy*. Ed. by D. Briggs and M.P. Seah. Frankfurt am Main: Otto Salle Verlag GmbH & Co., 1990.
- [31] D. Briggs and M.P. Seah, eds. *Auger and X-ray Photoelectron Spectroscopy*. Frankfurt am Main: Otto Salle Verlag GmbH & Co., 1990.
- [32] H. Hertz. “Ueber einen Einfluss des ultravioletten Lichtes auf die electrische Entladung”. In: *Annalen der Physik* 267.8 (1887), pp. 983–1000. ISSN: 1521-3889. DOI: 10.1002/andp.18872670827. URL: <http://onlinelibrary.wiley.com/doi/10.1002/andp.18872670827/abstract> (visited on 01/12/2015).
- [33] *The Nobel Prize in Physics 1921*. Jan. 15, 2015. URL: http://www.nobelprize.org/nobel_prizes/physics/laureates/1921/index.html (visited on 01/12/2015).
- [34] *X-ray Generation in XPS*. Sept. 21, 2015. URL: http://xpssimplified.com/xray_generation.php (visited on 09/21/2015).
- [35] D. Briggs and J.C. Rivière. “Spectral Interpretation”. In: *Auger and X-ray Photoelectron Spectroscopy*. Ed. by D. Briggs and M.P. Seah. Frankfurt am Main: Otto Salle Verlag GmbH & Co., 1990.
- [36] Dmitry Y Zemlyanov et al. “Versatile technique for assessing thickness of 2D layered materials by XPS”. In: *Nanotechnology* 29.11 (Mar. 16, 2018), p. 115705. ISSN: 0957-4484, 1361-6528. DOI: 10.1088/1361-6528/aaa6ef. URL: <http://stacks.iop.org/0957-4484/29/i=11/a=115705?key=crossref.c55893e7cb47891c5800779a12eb31ed> (visited on 08/10/2018).
- [37] Carsten Busse et al. “Graphene on Ir(111): Physisorption with Chemical Modulation”. In: *Phys. Rev. Lett.* 107.3 (July 2011), p. 036101. DOI: 10.1103/PhysRevLett.107.036101. URL: <http://link.aps.org/doi/10.1103/PhysRevLett.107.036101>.
- [38] Elin Gränäs et al. “Oxygen Intercalation under Graphene on Ir(111): Energetics, Kinetics, and the Role of Graphene Edges”. In: *ACS Nano* 6.11 (Nov. 27, 2012), pp. 9951–9963. ISSN: 1936-0851, 1936-086X. DOI: 10.1021/nn303548z. URL: <http://pubs.acs.org/doi/abs/10.1021/nn303548z> (visited on 10/15/2014).
- [39] G. Deroubaix and P. Marcus. “X-ray photoelectron spectroscopy analysis of copper and zinc oxides and sulphides”. In: *Surface and Interface Analysis* 18.1 (1992), pp. 39–46. ISSN: 1096-9918. DOI: 10.1002/sia.740180107. URL: <http://onlinelibrary.wiley.com/doi/10.1002/sia.740180107/abstract> (visited on 12/15/2014).
- [40] C. D. Wanger et al. *Handbook of X-ray Photoelectron Spectroscopy*. Vol. 3. Perkin-Elmer Corp., 1979. 190 pp. URL: <http://onlinelibrary.wiley.com/doi/10.1002/sia.740030412/abstract> (visited on 12/15/2014).
- [41] B. L. Henke, E. M. Gullikson, and J. C. Davis. “X-Ray Interactions: Photoabsorption, Scattering, Transmission, and Reflection at $E = 50\text{--}30,000 \text{ eV}$, $Z = 1\text{--}92$ ”. In: *Atomic Data and Nuclear Data Tables* 54.2 (July 1993), pp. 181–342. ISSN: 0092-640X. DOI: 10.1006/adnd.1993.1013. URL: <http://www.sciencedirect.com/science/article/pii/S0092640X83710132> (visited on 12/05/2014).

- [42] Gerhard Ertl and J. Kuppers. *Low Energy Electrons and Surface Chemistry*. Auflage: 2 Sub. Weinheim, Federal Republic of Germany ; Deerfield Beach, FL, USA: Vch Pub, Mar. 1986. ISBN: 9780895730657.
- [43] Yuanqin He. “Bottom-up Construction and Direct Characterization of Porphyrin- and Graphene-based Nanostructures”. PhD thesis. München: Technische Universität München, June 19, 2017. 147 pp. URL: <http://nbn-resolving.de/urn/resolver.pl?urn:nbn:de:bvb:91-diss-20170720-1362063-1-5>.
- [44] *Schematic of qPlus sensor*. 2013. URL: https://en.wikipedia.org/wiki/Non-contact_atomic_force_microscopy#/media/File:QPlusSchematic.svg (visited on 08/10/2018).
- [45] Niko Pavliček and Leo Gross. “Generation, manipulation and characterization of molecules by atomic force microscopy”. In: *Nature Reviews Chemistry* 1 (Jan. 11, 2017), p. 0005. URL: <http://dx.doi.org/10.1038/s41570-016-0005>.
- [46] J. E. Jones. “On the Determination of Molecular Fields. II. From the Equation of State of a Gas”. In: *Proceedings of the Royal Society A: Mathematical, Physical and Engineering Sciences* 106.738 (Oct. 1, 1924), pp. 463–477. ISSN: 1364-5021, 1471-2946. DOI: 10.1098/rspa.1924.0082. URL: <http://rspa.royalsocietypublishing.org/cgi/doi/10.1098/rspa.1924.0082> (visited on 08/23/2018).
- [47] Florian Albrecht et al. “Direct Identification and Determination of Conformational Response in Adsorbed Individual Nonplanar Molecular Species Using Noncontact Atomic Force Microscopy”. In: *Nano Letters* 16.12 (Dec. 14, 2016), pp. 7703–7709. ISSN: 1530-6984, 1530-6992. DOI: 10.1021/acs.nanolett.6b03769. URL: <http://pubs.acs.org/doi/10.1021/acs.nanolett.6b03769> (visited on 08/23/2018).
- [48] Shigeki Kawai et al. “Multiple heteroatom substitution to graphene nanoribbon”. In: *Science Advances* 4.4 (Apr. 2018), eaar7181. ISSN: 2375-2548. DOI: 10.1126/sciadv.aar7181. URL: <http://advances.sciencemag.org/lookup/doi/10.1126/sciadv.aar7181> (visited on 05/28/2018).
- [49] Shigeki Kawai et al. “Atomically controlled substitutional boron-doping of graphene nanoribbons”. In: *Nature Communications* 6.1 (Dec. 2015). ISSN: 2041-1723. DOI: 10.1038/ncomms9098. URL: <http://www.nature.com/articles/ncomms9098> (visited on 05/28/2018).
- [50] Fabian Schulz et al. “Elemental Identification by Combining Atomic Force Microscopy and Kelvin Probe Force Microscopy”. In: *ACS Nano* (May 25, 2018). ISSN: 1936-0851, 1936-086X. DOI: 10.1021/acsnano.7b08997. URL: <http://pubs.acs.org/doi/10.1021/acsnano.7b08997> (visited on 06/01/2018).
- [51] L. Gross et al. “The Chemical Structure of a Molecule Resolved by Atomic Force Microscopy”. In: *Science* 325.5944 (Aug. 28, 2009), pp. 1110–1114. ISSN: 0036-8075, 1095-9203. DOI: 10.1126/science.1176210. URL: <http://www.sciencemag.org/cgi/doi/10.1126/science.1176210> (visited on 05/25/2018).
- [52] Martin Schwarz et al. “Corrugation in the Weakly Interacting Hexagonal-BN/Cu(111) System: Structure Determination by Combining Noncontact Atomic Force Microscopy and X-ray Standing Waves”. In: *ACS Nano* 11.9 (Sept. 26, 2017), pp. 9151–9161. ISSN: 1936-0851, 1936-086X. DOI: 10.1021/acsnano.7b04022. URL: <http://pubs.acs.org/doi/10.1021/acsnano.7b04022> (visited on 07/20/2018).
- [53] José Ignacio Urgel Tendero. “Two-dimensional lanthanide-directed metal-organic networks at surfaces”. PhD thesis. München: Technische Universität München, Dec. 17, 2015. 161 pp. URL: <http://nbn-resolving.de/urn/resolver.pl?urn:nbn:de:bvb:91-diss-20160311-1286634-1-7>.

- [54] Martin Schwarz. "Assembly and Characterization of Hybrid Nanomaterials on Noble Metal Surfaces". PhD thesis. München: Technische Universität München, June 12, 2018. 240 pp. URL: <https://mediatum.ub.tum.de/doc/1436091/1436091.pdf>.
- [55] Alissa Wiengarten. "Scanning tunneling microscopy investigation of structure and electronic properties of surface-confined tetrapyrrolic species". PhD thesis. München: Technische Universität München, July 21, 2015. 134 pp. URL: <http://nbn-resolving.de/urn/resolver.pl?urn=nbn:de:bvb:91-diss-20150723-1256606-1-5>.
- [56] Andreas Riemann. "Ionic Insulators on Vicinal Metal Surfaces". PhD thesis. Freie Universität Berlin, Freie Universität Berlin, Germany, 2002. URL: <https://refubium.fu-berlin.de/handle/fub188/624> (visited on 07/27/2015).
- [57] MaTecK. Aug. 10, 2018. URL: <https://mateck.com/info/metal-single-crystals.html> (visited on 08/10/2018).
- [58] Ferdinand H. Farwick zum Hagen et al. "Structure and Growth of Hexagonal Boron Nitride on Ir(111)". In: *ACS Nano* (Nov. 14, 2016). ISSN: 1936-0851. DOI: 10.1021/acsnano.6b05819. URL: <http://dx.doi.org/10.1021/acsnano.6b05819> (visited on 11/25/2016).
- [59] Zhang Jian-Min, Ma Fei, and Xu Ke-Wei. "Calculation of the surface energy of fcc metals with modified embedded-atom method". In: *Chinese Physics* 13.7 (2004), p. 1082. ISSN: 1009-1963. DOI: 10.1088/1009-1963/13/7/020. URL: <http://stacks.iop.org/1009-1963/13/i=7/a=020> (visited on 11/12/2015).
- [60] *Dislocation theory*. Oct. 27, 2015. URL: http://eng.sut.ac.th/metal/images/stories/pdf/05_Dislocation_theory.pdf (visited on 10/27/2015).
- [61] Felix Hanke and Jonas Björk. "Structure and local reactivity of the Au(111) surface reconstruction". In: *Phys. Rev. B* 87 (23 June 2013), p. 235422. DOI: 10.1103/PhysRevB.87.235422. URL: <https://link.aps.org/doi/10.1103/PhysRevB.87.235422>.
- [62] Tuan Anh Pham et al. "Self-assembly of pyrene derivatives on Au(111): substituent effects on intermolecular interactions". In: 50.91 (Oct. 21, 2014), pp. 14089–14092. ISSN: 1364-548X. DOI: 10.1039/C4CC02753A. URL: <http://pubs.rsc.org/en/content/articlelanding/2014/cc/c4cc02753a> (visited on 02/21/2017).
- [63] Tuan Anh Pham et al. "Heat-induced formation of one-dimensional coordination polymers on Au(111): an STM study". In: *Chemical Communications* 51.77 (2015), pp. 14473–14476. ISSN: 1359-7345, 1364-548X. DOI: 10.1039/C5CC04940G. URL: <http://xlink.rsc.org/?DOI=C5CC04940G> (visited on 08/21/2018).
- [64] D. M. Turley and L. E. Samuels. "The nature of mechanically polished surfaces of copper". In: *Metallography* 14.4 (1981), pp. 275–294. ISSN: 0026-0800. DOI: [https://doi.org/10.1016/0026-0800\(81\)90001-X](https://doi.org/10.1016/0026-0800(81)90001-X). URL: <http://www.sciencedirect.com/science/article/pii/002608008190001X>.
- [65] Wi Hyoung Lee Bin Zhang. "Low-temperature chemical vapor deposition growth of graphene from toluene on electropolished copper foils." In: *ACS nano* 6.3 (2012), pp. 2471–6. ISSN: 1936-086X. DOI: 10.1021/nm204827h.
- [66] Ki Kang Kim et al. "Synthesis of Monolayer Hexagonal Boron Nitride on Cu Foil Using Chemical Vapor Deposition". In: *Nano Letters* 12.1 (Jan. 11, 2012), pp. 161–166. ISSN: 1530-6984. DOI: 10.1021/nl203249a. URL: <http://dx.doi.org/10.1021/nl203249a> (visited on 11/10/2014).
- [67] Huo Jinshan. "Electrochemical planarization of copper for microelectronic applications". In: (2004). URL: <http://digitalcommons.ohsu.edu/cgi/viewcontent.cgi?article=1208&context=etd> (visited on 12/12/2014).

- [68] Claire Antoine et al. *Alternative Approaches for Nb Superconducting Cavities Surface Treatment (Invited paper)*. Jan. 1999.
- [69] L. Lilje et al. “Improved surface treatment of the superconducting TESLA cavities”. In: *Nuclear Instruments and Methods in Physics Research Section A: Accelerators, Spectrometers, Detectors and Associated Equipment* 516.2 (2004), pp. 213–227. ISSN: 0168-9002. DOI: <https://doi.org/10.1016/j.nima.2003.08.116>. URL: <http://www.sciencedirect.com/science/article/pii/S0168900203024318>.
- [70] E Schulz et al. “Engineering solutions for the electropolishing of multi-cell superconducting accelerator structures”. In: (Aug. 2018).
- [71] Matt Stables et al. “Report on the Current Surface Characterisation Research Project for the UKRF Cavity Development Programme”. In: (Aug. 2018). URL: https://www.researchgate.net/publication/237827266_Report_on_the_Current_Surface_Characterisation_Research_Project_for_the_UKRF_Cavity_Development_Programme.
- [72] Zhengtang Luo et al. “Effect of Substrate Roughness and Feedstock Concentration on Growth of Wafer-Scale Graphene at Atmospheric Pressure”. In: *Chemistry of Materials* 23.6 (Mar. 22, 2011), pp. 1441–1447. ISSN: 0897-4756, 1520-5002. DOI: <10.1021/cm1028854>. URL: <http://pubs.acs.org/doi/abs/10.1021/cm1028854> (visited on 12/09/2014).
- [73] *CAS DataBase | 7664-38-2*. Dec. 11, 2014. URL: http://www.chemicalbook.com/CASEN_7664-38-2.htm (visited on 12/11/2014).
- [74] Shih-Chieh Chang et al. “Superpolishing for Planarizing Copper Damascene Interconnects”. In: *Electrochemical and Solid-State Letters* 6.5 (Jan. 5, 2003), G72–G74. ISSN: 1099-0062, 1944-8775. DOI: <10.1149/1.1565853>. URL: <http://esl.ecsdl.org/content/6/5/G72> (visited on 12/11/2014).
- [75] “OPEN CHEMISTRY DATABASE”. Aug. 1, 2018. URL: <https://www.ncbi.nlm.nih.gov/pccompound> (visited on 08/01/2018).
- [76] Alpha T N'Diaye et al. “Structure of epitaxial graphene on Ir(111)”. In: *New Journal of Physics* 10.4 (Apr. 18, 2008), p. 043033. ISSN: 1367-2630. DOI: <10.1088/1367-2630/10/4/043033>. URL: <http://stacks.iop.org/1367-2630/10/i=4/a=043033?key=crossref.0e41254297199ed913e0eb6bd000151a> (visited on 10/15/2014).
- [77] Johann Coraux et al. “Growth of graphene on Ir(111)”. In: *New Journal of Physics* 11.2 (2009), p. 023006. URL: <http://stacks.iop.org/1367-2630/11/i=2/a=023006>.
- [78] Frank Müller et al. “Epitaxial growth of hexagonal boron nitride on Ag(111)”. In: *Phys. Rev. B* 82.11 (Sept. 2010), p. 113406. DOI: <10.1103/PhysRevB.82.113406>. URL: <http://link.aps.org/doi/10.1103/PhysRevB.82.113406>.
- [79] Sushobhan Joshi et al. “Boron Nitride on Cu(111): An Electronically Corrugated Monolayer”. In: *Nano Letters* 12.11 (2012), pp. 5821–5828. DOI: <10.1021/nl303170m>. URL: <http://pubs.acs.org/doi/abs/10.1021/nl303170m>.
- [80] Qiucheng Li et al. “Grain Boundary Structures and Electronic Properties of Hexagonal Boron Nitride on Cu(111)”. In: *Nano Letters* 15.9 (Sept. 9, 2015), pp. 5804–5810. ISSN: 1530-6984. DOI: <10.1021/acs.nanolett.5b01852>. URL: <http://dx.doi.org/10.1021/acs.nanolett.5b01852> (visited on 05/03/2017).
- [81] A.B. Preobrajenski, A.S. Vinogradov, and N. Mårtensson. “Monolayer of h-BN chemisorbed on Cu(111) and Ni(111): The role of the transition metal 3d states”. In: *Surface Science* 582.1 (May 2005), pp. 21–30. ISSN: 00396028. DOI: <10.1016/j.susc.2005.02.047>. URL: <http://linkinghub.elsevier.com/retrieve/pii/S0039602805002426> (visited on 10/28/2014).

- [82] W. Auwärter et al. “XPD and STM investigation of hexagonal boron nitride on Ni(111)”. In: *Surface Science* 429.1 (June 1999), pp. 229–236. ISSN: 00396028. DOI: 10.1016/S0039-6028(99)00381-7. URL: <http://linkinghub.elsevier.com/retrieve/pii/S0039602899003817> (visited on 10/23/2014).
- [83] M. Morscher et al. “Formation of single layer h-BN on Pd(111)”. In: *Surface Science* 600.16 (2006), pp. 3280–3284. ISSN: 0039-6028. DOI: <http://dx.doi.org/10.1016/j.susc.2006.06.016>. URL: <http://www.sciencedirect.com/science/article/pii/S0039602806007266>.
- [84] A. B. Preobrajenski et al. “Monolayer h-BN on lattice-mismatched metal surfaces: On the formation of the nanomesh”. In: *Chemical Physics Letters* 446.1 (2007), pp. 119–123. ISSN: 0009-2614. DOI: 10.1016/j.cplett.2007.08.028. URL: <http://www.sciencedirect.com/science/article/pii/S0009261407010998>.
- [85] Martina Corso et al. “Boron Nitride Nanomesh”. In: *Science* 303.5655 (2004), pp. 217–220. DOI: 10.1126/science.1091979. URL: <http://www.sciencemag.org/content/303/5655/217.abstract>.
- [86] Andrii Goriachko et al. “Self-Assembly of a Hexagonal Boron Nitride Nanomesh on Ru(0001)”. In: *Langmuir* 23.6 (2007). STM, pp. 2928–2931. DOI: 10.1021/la062990t. URL: <http://pubs.acs.org/doi/abs/10.1021/la062990t>.
- [87] Piran R. Kidambi et al. “In Situ Observations during Chemical Vapor Deposition of Hexagonal Boron Nitride on Polycrystalline Copper”. In: *Chemistry of Materials* 26.22 (2014), pp. 6380–6392. ISSN: 0897-4756. DOI: 10.1021/cm502603n. URL: <http://dx.doi.org/10.1021/cm502603n> (visited on 12/15/2014).
- [88] Ki Kang Kim et al. “Synthesis and Characterization of Hexagonal Boron Nitride Film as a Dielectric Layer for Graphene Devices”. In: *ACS Nano* 6.10 (Oct. 23, 2012), pp. 8583–8590. ISSN: 1936-0851, 1936-086X. DOI: 10.1021/nn301675f. URL: <http://pubs.acs.org/doi/abs/10.1021/nn301675f> (visited on 12/01/2014).
- [89] Willi Auwärter et al. “Synthesis of One Monolayer of Hexagonal Boron Nitride on Ni(111) from B-Trichloroborazine (ClBNH)₃”. In: *Chemistry of Materials* 16.2 (Jan. 2004), pp. 343–345. ISSN: 0897-4756, 1520-5002. DOI: 10.1021/cm034805s. URL: <http://pubs.acs.org/doi/abs/10.1021/cm034805s> (visited on 10/15/2014).
- [90] Frank Müller, Klaus Stöwe, and Hermann Sachdev. “Symmetry versus Commensurability: Epitaxial Growth of Hexagonal Boron Nitride on Pt(111) From B-Trichloroborazine (ClBNH)₃”. In: *Chemistry of Materials* 17.13 (2005), pp. 3464–3467. DOI: 10.1021/cm048629e. URL: <http://pubs.acs.org/doi/abs/10.1021/cm048629e>.
- [91] Ning Guo et al. “Controllable growth of triangular hexagonal boron nitride domains on copper foils by an improved low-pressure chemical vapor deposition method”. In: *Nanotechnology* 23.41 (Oct. 19, 2012), p. 415605. ISSN: 0957-4484, 1361-6528. DOI: 10.1088/0957-4484/23/41/415605. URL: <http://stacks.iop.org/0957-4484/23/i=41/a=415605?key=crossref.113b515178c834c75ca332235bf20bf1> (visited on 10/15/2014).
- [92] Kang Hyuck Lee et al. “Large-Scale Synthesis of High-Quality Hexagonal Boron Nitride Nanosheets for Large-Area Graphene Electronics”. In: *Nano Letters* 12.2 (Feb. 8, 2012), pp. 714–718. ISSN: 1530-6984. DOI: 10.1021/nl203635v. URL: <http://dx.doi.org/10.1021/nl203635v> (visited on 11/10/2014).
- [93] Ariel Ismach et al. “Toward the Controlled Synthesis of Hexagonal Boron Nitride Films”. In: *ACS Nano* 6.7 (July 24, 2012), pp. 6378–6385. ISSN: 1936-0851. DOI: 10.1021/nn301940k. URL: <http://dx.doi.org/10.1021/nn301940k> (visited on 11/10/2014).

- [94] Shahana Chatterjee et al. “Chemical Vapor Deposition of Boron Nitride Nanosheets on Metallic Substrates via Decaborane/Ammonia Reactions”. In: *Chemistry of Materials* 23.20 (Oct. 25, 2011), pp. 4414–4416. ISSN: 0897-4756. DOI: 10.1021/cm201955v. URL: <http://dx.doi.org/10.1021/cm201955v> (visited on 11/10/2014).
- [95] Gene Siegel et al. “Heterogeneous Pyrolysis: A Route for Epitaxial Growth of hBN Atomic Layers on Copper Using Separate Boron and Nitrogen Precursors”. In: *Nano Letters* 17.4 (Apr. 12, 2017), pp. 2404–2413. ISSN: 1530-6984, 1530-6992. DOI: 10.1021/acs.nanolett.6b05409. URL: <http://pubs.acs.org/doi/10.1021/acs.nanolett.6b05409> (visited on 08/14/2018).
- [96] A. Nagashima et al. “Electronic Structure of Monolayer Hexagonal Boron Nitride Physisorbed on Metal Surfaces”. In: *Phys. Rev. Lett.* 75.21 (Nov. 1995), pp. 3918–3921. DOI: 10.1103/PhysRevLett.75.3918. URL: <http://link.aps.org/doi/10.1103/PhysRevLett.75.3918>.
- [97] Jaime Gómez Díaz et al. “Hexagonal boron nitride on transition metal surfaces”. In: *Theoretical Chemistry Accounts* 132.4 (Apr. 2013). ISSN: 1432-881X, 1432-2234. DOI: 10.1007/s00214-013-1350-z. URL: <http://link.springer.com/10.1007/s00214-013-1350-z> (visited on 10/23/2014).
- [98] Fabrizio Orlando et al. “Epitaxial Growth of Hexagonal Boron Nitride on Ir(111)”. In: *The Journal of Physical Chemistry C* 116.1 (2012), pp. 157–164. DOI: 10.1021/jp207571n. URL: <http://pubs.acs.org/doi/abs/10.1021/jp207571n>.
- [99] Martina Corso, Thomas Greber, and Jürg Osterwalder. “h-BN on Pd(110): a tunable system for self-assembled nanostructures?” In: *Surface Science* 577.2 (Mar. 2005), pp. L78–L84. ISSN: 00396028. DOI: 10.1016/j.susc.2005.01.015. URL: <http://linkinghub.elsevier.com/retrieve/pii/S0039602805000531> (visited on 08/14/2018).
- [100] E. Ćavar et al. “A single h-BN layer on Pt(111)”. In: *Surface Science* 602.9 (May 2008), pp. 1722–1726. ISSN: 00396028. DOI: 10.1016/j.susc.2008.03.008. URL: <http://linkinghub.elsevier.com/retrieve/pii/S0039602808001672> (visited on 08/14/2018).
- [101] Silvan Roth et al. “Chemical Vapor Deposition and Characterization of Aligned and Incommensurate Graphene/Hexagonal Boron Nitride Heterostack on Cu(111)”. In: *Nano Letters* 13.6 (June 12, 2013), pp. 2668–2675. ISSN: 1530-6984, 1530-6992. DOI: 10.1021/nl400815w. URL: <http://pubs.acs.org/doi/abs/10.1021/nl400815w> (visited on 10/28/2014).
- [102] Klaus Hermann. “Periodic overlayers and moire patterns: theoretical studies of geometric properties”. In: *Journal of Physics: Condensed Matter* 24.31 (2012), p. 314210. ISSN: 0953-8984. DOI: 10.1088/0953-8984/24/31/314210. URL: <http://stacks.iop.org/0953-8984/24/i=31/a=314210> (visited on 10/27/2015).
- [103] Fabian Schulz et al. “Epitaxial hexagonal boron nitride on Ir (111): A work function template”. In: *arXiv preprint arXiv:1404.7371* (2014). URL: <http://arxiv.org/abs/1404.7371> (visited on 10/15/2014).
- [104] Tanglaw Roman and Axel Groß. “Periodic Density-Functional Calculations on Work-Function Change Induced by Adsorption of Halogens on Cu(111)”. In: *Physical Review Letters* 110.15 (Apr. 12, 2013). ISSN: 0031-9007, 1079-7114. DOI: 10.1103/PhysRevLett.110.156804. URL: <https://link.aps.org/doi/10.1103/PhysRevLett.110.156804> (visited on 08/14/2018).
- [105] Tongwei Han, Ying Luo, and Chengyuan Wang. “Effects of temperature and strain rate on the mechanical properties of hexagonal boron nitride nanosheets”. In: *Journal of Physics D: Applied Physics* 47.2 (2014), p. 025303. URL: <http://stacks.iop.org/0022-3727/47/i=2/a=025303>.

- [106] Bohayra Mortazavi and Yves Rémond. “Investigation of tensile response and thermal conductivity of boron-nitride nanosheets using molecular dynamics simulations”. In: *Physica E: Low-dimensional Systems and Nanostructures* 44.9 (2012), pp. 1846–1852. ISSN: 1386-9477. DOI: <http://dx.doi.org/10.1016/j.physe.2012.05.007>. URL: <http://www.sciencedirect.com/science/article/pii/S1386947712001804>.
- [107] M. Topsakal, E. Aktürk, and S. Ciraci. “First-principles study of two- and one-dimensional honeycomb structures of boron nitride”. In: *Phys. Rev. B* 79.11 (Mar. 2009), p. 115442. DOI: 10.1103/PhysRevB.79.115442. URL: <http://link.aps.org/doi/10.1103/PhysRevB.79.115442>.
- [108] Qing Peng, Wei Ji, and Suvernu De. “Mechanical properties of the hexagonal boron nitride monolayer: Ab initio study”. In: *Computational Materials Science* 56.0 (2012), pp. 11–17. ISSN: 0927-0256. DOI: <http://dx.doi.org/10.1016/j.commatsci.2011.12.029>. URL: <http://www.sciencedirect.com/science/article/pii/S0927025611006902>.
- [109] W. Paszkowicz et al. “Lattice parameters and anisotropic thermal expansion of hexagonal boron nitride in the \$10-297.5\\$,K temperature range”. In: *Applied Physics A* 75.3 (2002), pp. 431–435. ISSN: 0947-8396. DOI: 10.1007/s003390100999. URL: <http://dx.doi.org/10.1007/s003390100999>.
- [110] H. G. Zhang et al. “Assembly of iron phthalocyanine and pentacene molecules on a graphene monolayer grown on Ru(0001)”. In: *Physical Review B* 84.24 (Dec. 19, 2011), p. 245436. DOI: 10.1103/PhysRevB.84.245436. URL: <https://link.aps.org/doi/10.1103/PhysRevB.84.245436> (visited on 05/03/2017).
- [111] “HyperChem(TM) Professional 7.51, Hypercube, Inc., 1115 NW 4th Street, Gainesville, Florida 32601, USA.”
- [112] Alan R. Battersby. “Tetrapyrroles: the pigments of life”. In: *Natural Product Reports* 17.6 (2000), pp. 507–526. ISSN: 02650568, 14604752. DOI: 10.1039/b002635m. URL: <http://xlink.rsc.org/?DOI=b002635m> (visited on 08/21/2018).
- [113] Willi Auwärter et al. “Porphyrins at interfaces”. In: *Nature Chemistry* 7.2 (Feb. 2015), pp. 105–120. ISSN: 1755-4330. DOI: 10.1038/nchem.2159. URL: <http://www.nature.com/nchem/journal/v7/n2/full/nchem.2159.html> (visited on 11/12/2015).
- [114] Willi Auwärter et al. “Controlled Metalation of Self-Assembled Porphyrin Nanoarrays in Two Dimensions”. In: *ChemPhysChem* 8.2 (Feb. 2, 2007), pp. 250–254. ISSN: 14394235, 14397641. DOI: 10.1002/cphc.200600675. URL: <http://doi.wiley.com/10.1002/cphc.200600675> (visited on 08/21/2018).
- [115] Katharina Diller et al. “In vacuo interfacial tetrapyrrole metallation”. In: *Chemical Society Reviews* 45.6 (2016), pp. 1629–1656. ISSN: 0306-0012, 1460-4744. DOI: 10.1039/C5CS00207A. URL: <http://xlink.rsc.org/?DOI=C5CS00207A> (visited on 08/21/2018).
- [116] William P. Lustig et al. “Metal–organic frameworks: functional luminescent and photonic materials for sensing applications”. In: *Chem. Soc. Rev.* 46 (11 2017), pp. 3242–3285. DOI: 10.1039/C6CS00930A. URL: <http://dx.doi.org/10.1039/C6CS00930A>.
- [117] Francesca Moresco et al. “Conformational Changes of Single Molecules Induced by Scanning Tunneling Microscopy Manipulation: A Route to Molecular Switching”. In: *Physical Review Letters* 86.4 (Jan. 22, 2001), pp. 672–675. DOI: 10.1103/PhysRevLett.86.672. URL: <http://link.aps.org/doi/10.1103/PhysRevLett.86.672> (visited on 11/12/2015).
- [118] M. Stark et al. “Massive conformational changes during thermally induced self-metalation of 2H-tetrakis-(3,5-di-tert-butyl)-phenylporphyrin on Cu(111)”. In: *Chemical Communications* 50.71 (July 14, 2014), p. 10225. ISSN: 1359-7345, 1364-548X. DOI: 10.1039/C4CC03708A. URL: <http://xlink.rsc.org/?DOI=C4CC03708A> (visited on 11/12/2015).

Bibliography

- [119] Ch. Loppacher et al. “Direct Determination of the Energy Required to Operate a Single Molecule Switch”. In: *Physical Review Letters* 90.6 (Feb. 14, 2003). ISSN: 0031-9007, 1079-7114. DOI: 10.1103/PhysRevLett.90.066107. URL: <https://link.aps.org/doi/10.1103/PhysRevLett.90.066107> (visited on 08/15/2018).
- [120] Stefanie Ditze et al. “On the Energetics of Conformational Switching of Molecules at and Close to Room Temperature”. In: *Journal of the American Chemical Society* 136.4 (Jan. 29, 2014), pp. 1609–1616. ISSN: 0002-7863. DOI: 10.1021/ja411884p. URL: <http://dx.doi.org/10.1021/ja411884p> (visited on 11/12/2015).
- [121] Puneet Mishra et al. “Current-Driven Supramolecular Motor with In Situ Surface Chiral Directionality Switching”. In: *Nano Letters* 15.7 (July 8, 2015), pp. 4793–4798. ISSN: 1530-6984, 1530-6992. DOI: 10.1021/acs.nanolett.5b01908. URL: <http://pubs.acs.org/doi/abs/10.1021/acs.nanolett.5b01908> (visited on 07/13/2015).
- [122] Takashi Yokoyama et al. “Selective assembly on a surface of supramolecular aggregates with controlled size and shape”. In: *Nature* 413 (Oct. 11, 2001), p. 619. URL: <http://dx.doi.org/10.1038/35098059>.
- [123] D. Ecija et al. “Dynamics and thermal stability of surface-confined metal–organic chains”. In: *Surface Science* 643 (Jan. 2016), pp. 91–97. ISSN: 00396028. DOI: 10.1016/j.susc.2015.08.013. URL: <http://linkinghub.elsevier.com/retrieve/pii/S0039602815002332> (visited on 08/21/2018).
- [124] William L. Jorgensen and Lionel Salem. *The Organic Chemist’s Book of Orbitals*. New York: Academic Press, 1973. ISBN: 0-12-390250-9.
- [125] Z. H. Khan and B. N. Khanna. “Electronic absorption spectra of pyrene and its monopositive ion”. In: *The Journal of Chemical Physics* 59.6 (Sept. 15, 1973), pp. 3015–3019. ISSN: 0021-9606, 1089-7690. DOI: 10.1063/1.1680437. URL: <http://scitation.aip.org/content/aip/journal/jcp/59/6/10.1063/1.1680437> (visited on 07/29/2016).
- [126] Andrew G. Crawford et al. “Experimental and Theoretical Studies of the Photophysical Properties of 2- and 2,7-Functionalized Pyrene Derivatives”. In: *Journal of the American Chemical Society* 133.34 (Aug. 31, 2011), pp. 13349–13362. ISSN: 0002-7863. DOI: 10.1021/ja2006862. URL: <http://dx.doi.org/10.1021/ja2006862> (visited on 08/22/2017).
- [127] Yeon Ok Lee et al. “Enhanced Electrogenerated Chemiluminescence of Phenylethynylpyrene Derivatives: Use of Weakly Electron-Donating Group as a Substituent”. In: *The Journal of Organic Chemistry* 77.24 (Dec. 21, 2012), pp. 11007–11013. ISSN: 0022-3263. DOI: 10.1021/jo3010974. URL: <http://dx.doi.org/10.1021/jo3010974> (visited on 08/22/2017).
- [128] Xing Feng et al. “Functionalization of Pyrene To Prepare Luminescent Materials-Typical Examples of Synthetic Methodology”. In: *Chemistry - A European Journal* 22.34 (Aug. 16, 2016), pp. 11898–11916. ISSN: 09476539. DOI: 10.1002/chem.201600465. URL: <http://doi.wiley.com/10.1002/chem.201600465> (visited on 01/04/2018).
- [129] Ryohei Kurata et al. “Diaryl amino- and Diarylboryl-Substituted Donor-Acceptor Pyrene Derivatives: Influence of Substitution Pattern on Their Photophysical Properties”. In: *The Journal of Organic Chemistry* 82.10 (May 19, 2017), pp. 5111–5121. ISSN: 0022-3263. DOI: 10.1021/acs.joc.7b00315. URL: <http://dx.doi.org/10.1021/acs.joc.7b00315> (visited on 08/22/2017).
- [130] Hajime Maeda et al. “Alkynylypyrenes as Improved Pyrene-Based Biomolecular Probes with the Advantages of High Fluorescence Quantum Yields and Long Absorption/Emission Wavelengths”. In: *Chemistry - A European Journal* 12.3 (Jan. 11, 2006), pp. 824–831. ISSN: 1521-3765. DOI: 10.1002/chem.200500638. URL: <http://onlinelibrary.wiley.com/doi/10.1002/chem.200500638/abstract> (visited on 07/12/2017).

- [131] Manfred Matena et al. “Aggregation and Contingent Metal/Surface Reactivity of 1,3,8,10-Tetraazaperopyrene (TAPP) on Cu(111)”. In: *Chemistry – A European Journal* 16.7 (Feb. 15, 2010), pp. 2079–2091. ISSN: 1521-3765. DOI: 10.1002/chem.200902596. URL: <http://onlinelibrary.wiley.com/doi/10.1002/chem.200902596/abstract> (visited on 02/22/2017).
- [132] Ada Della Pia et al. “Anomalous Coarsening Driven by Reversible Charge Transfer at Metal–Organic Interfaces”. In: *ACS Nano* 8.12 (Dec. 23, 2014), pp. 12356–12364. ISSN: 1936-0851. DOI: 10.1021/nn505063w. URL: <http://dx.doi.org/10.1021/nn505063w> (visited on 02/21/2017).
- [133] Tuan Anh Pham et al. “Comparing Ullmann Coupling on Noble Metal Surfaces: On-Surface Polymerization of 1,3,6,8-Tetrabromopyrene on Cu(111) and Au(111)”. In: *Chemistry – A European Journal* 22.17 (Apr. 18, 2016), pp. 5937–5944. ISSN: 1521-3765. DOI: 10.1002/chem.201504946. URL: <http://onlinelibrary.wiley.com/doi/10.1002/chem.201504946/abstract> (visited on 02/21/2017).
- [134] Melvin S. Newman and Daniel Lednicer. “The Synthesis and Resolution of Hexahelicene”. In: *Journal of the American Chemical Society* 78.18 (Sept. 1, 1956), pp. 4765–4770. ISSN: 0002-7863. DOI: 10.1021/ja01599a060. URL: <http://dx.doi.org/10.1021/ja01599a060> (visited on 06/01/2016).
- [135] E. Vander Donckt et al. “Fluorescence of the helicenes”. In: *Chemical Physics Letters* 2.6 (Oct. 1968), pp. 409–410. ISSN: 00092614. DOI: 10.1016/0009-2614(68)80041-7. URL: <http://linkinghub.elsevier.com/retrieve/pii/0009261468800417> (visited on 01/22/2018).
- [136] Matthias Krieg et al. “Construction of an Internally B3N3-Doped Nanographene Molecule”. In: *Angewandte Chemie International Edition* 54.28 (), pp. 8284–8286. DOI: 10.1002/anie.201412165. eprint: <https://onlinelibrary.wiley.com/doi/pdf/10.1002/anie.201412165>. URL: <https://onlinelibrary.wiley.com/doi/abs/10.1002/anie.201412165>.
- [137] F. Cicullo et al. “A Quasi-Free-Standing Single Layer of a B3N3-Doped Nanographene Molecule Deposited on Au(111) Single Crystals”. In: *The Journal of Physical Chemistry C* 120.31 (2016), pp. 17645–17651. DOI: 10.1021/acs.jpcc.6b06237. eprint: <https://doi.org/10.1021/acs.jpcc.6b06237>. URL: <https://doi.org/10.1021/acs.jpcc.6b06237>.
- [138] Jacopo Dosso et al. “Synthesis and Optoelectronic Properties of Hexa-*peri*-hexabenzoborazinocoronene”. In: *Angewandte Chemie* 129.16 (Apr. 10, 2017), pp. 4554–4558. ISSN: 00448249. DOI: 10.1002/ange.201700907. URL: <http://doi.wiley.com/10.1002/ange.201700907> (visited on 08/16/2018).
- [139] V. Palmieri et al. “Besides the standard Niobium bath chemical polishing”. In: 10 th W orkshop on RF Su percondutivity. Tsukuba , Japan, 2001. URL: <https://accelconf.web.cern.ch/accelconf/srf01/papers/pr016.pdf> (visited on 08/11/2018).
- [140] Manfred von Ardenne. “Das Elektronen-Rastermikroskop”. In: *Zeitschrift für Physik* 109.9 (Sept. 1938), pp. 553–572. ISSN: 0044-3328. DOI: 10.1007/BF01341584. URL: <http://link.springer.com/article/10.1007/BF01341584> (visited on 04/05/2016).
- [141] Yaping Wu et al. “Effects of thermally-induced changes of Cu grains on domain structure and electrical performance of CVD-grown graphene”. In: *Nanoscale* 8.2 (Dec. 23, 2015), pp. 930–937. ISSN: 2040-3372. DOI: 10.1039/C5NR06195D. URL: <http://pubs.rsc.org/en/content/articlelanding/2016/nr/c5nr06195d> (visited on 04/05/2016).
- [142] *Graphene Supermarket :: Boron Nitride (BN) :: Single layer h-BN (Boron Nitride) film grown on copper foil: 2" x 1"*. Dec. 11, 2014. URL: <https://graphene-supermarket.com/Single-layer-h-BN-Boron-Nitride-film-grown-in-copper-foil-2-x-1.html> (visited on 12/11/2014).

- [143] K. A. Simonov et al. “Controllable oxidation of h-BN monolayer on Ir(111) studied by core-level spectroscopies”. In: *Surface Science* 606.3 (2012), pp. 564–570. ISSN: 0039-6028. DOI: <http://dx.doi.org/10.1016/j.susc.2011.11.031>. URL: <http://www.sciencedirect.com/science/article/pii/S003960281100464X>.
- [144] Jose I. Urgel et al. “Controlling Coordination Reactions and Assembly on a Cu(111) Supported Boron Nitride Monolayer”. In: *Journal of the American Chemical Society* 137.7 (Feb. 25, 2015), pp. 2420–2423. ISSN: 0002-7863, 1520-5126. DOI: 10.1021/ja511611r. URL: <http://pubs.acs.org/doi/abs/10.1021/ja511611r> (visited on 09/09/2015).
- [145] Sam Haq et al. “Clean Coupling of Unfunctionalized Porphyrins at Surfaces To Give Highly Oriented Organometallic Oligomers”. In: *Journal of the American Chemical Society* 133.31 (Aug. 10, 2011), pp. 12031–12039. ISSN: 0002-7863, 1520-5126. DOI: 10.1021/ja201389u. URL: <http://pubs.acs.org/doi/abs/10.1021/ja201389u> (visited on 08/16/2018).
- [146] Florian Buchner et al. “Diffusion, Rotation, and Surface Chemical Bond of Individual 2 H-Tetraphenylporphyrin Molecules on Cu(111)”. In: *The Journal of Physical Chemistry C* 115.49 (Dec. 15, 2011), pp. 24172–24177. ISSN: 1932-7447, 1932-7455. DOI: 10.1021/jp206675u. URL: <http://pubs.acs.org/doi/10.1021/jp206675u> (visited on 08/16/2018).
- [147] Rubén González-Moreno et al. “Following the Metalation Process of Protoporphyrin IX with Metal Substrate Atoms at Room Temperature”. In: *The Journal of Physical Chemistry C* 115.14 (Apr. 14, 2011), pp. 6849–6854. ISSN: 1932-7447, 1932-7455. DOI: 10.1021/jp200533a. URL: <http://pubs.acs.org/doi/10.1021/jp200533a> (visited on 08/16/2018).
- [148] K. Diller et al. “Self-metalation of 2H-tetraphenylporphyrin on Cu(111): an x-ray spectroscopy study”. In: *The Journal of Chemical Physics* 136.1 (Jan. 7, 2012), p. 014705. ISSN: 1089-7690. DOI: 10.1063/1.3674165.
- [149] Stefanie Ditze et al. “Activation Energy for the Self-Metalation Reaction of 2H-Tetraphenylporphyrin on Cu(111)”. In: *Angewandte Chemie International Edition* 51.43 (Oct. 22, 2012), pp. 10898–10901. ISSN: 1521-3773. DOI: 10.1002/anie.201205464. URL: <http://onlinelibrary.wiley.com/doi/10.1002/anie.201205464/abstract> (visited on 11/05/2014).
- [150] Geoffrey Rojas et al. “Self-Assembly and Properties of Nonmetalated Tetraphenyl-Porphyrin on Metal Substrates”. In: *The Journal of Physical Chemistry C* 114.20 (May 27, 2010), pp. 9408–9415. ISSN: 1932-7447, 1932-7455. DOI: 10.1021/jp1012957. URL: <http://pubs.acs.org/doi/10.1021/jp1012957> (visited on 08/16/2018).
- [151] U. Schlickum et al. “Metal-Organic Honeycomb Nanomeshes with Tunable Cavity Size”. In: *Nano Letters* 7.12 (Dec. 1, 2007), pp. 3813–3817. ISSN: 1530-6984. DOI: 10.1021/nl072466m. URL: <http://dx.doi.org/10.1021/nl072466m> (visited on 08/26/2016).
- [152] Paweł Przychodzeń et al. “Supramolecular coordination networks based on octacyanometalates: From structure to function”. In: *Coordination Chemistry Reviews*. 20th International Conference on Coordination and Bioinorganic Chemistry 250.17 (Sept. 2006), pp. 2234–2260. ISSN: 0010-8545. DOI: 10.1016/j.ccr.2006.01.026. URL: <http://www.sciencedirect.com/science/article/pii/S0010854506000348> (visited on 08/26/2016).
- [153] Kazuaki Kato and Hans-Jörg Schneider. “Dispersive Effects in Chemomechanical Reactions with Polyallylamine-Derived Hydrogels”. In: *European Journal of Organic Chemistry* 2008.8 (Mar. 1, 2008), pp. 1378–1382. ISSN: 1099-0690. DOI: 10.1002/ejoc.200700850. URL: <http://onlinelibrary.wiley.com/doi/10.1002/ejoc.200700850/abstract> (visited on 04/14/2016).
- [154] Daniel Heim et al. “Surface-Assisted Assembly of Discrete Porphyrin-Based Cyclic Supramolecules”. In: *Nano Letters* 10.1 (Jan. 13, 2010), pp. 122–128. ISSN: 1530-6984. DOI: 10.1021/nl9029994. URL: <http://dx.doi.org/10.1021/nl9029994> (visited on 04/14/2016).

- [155] Daniel Heim et al. “Self-Assembly of Flexible One-Dimensional Coordination Polymers on Metal Surfaces”. In: *Journal of the American Chemical Society* 132.19 (May 19, 2010), pp. 6783–6790. ISSN: 0002-7863. DOI: 10.1021/ja1010527. URL: <http://dx.doi.org/10.1021/ja1010527> (visited on 04/14/2016).
- [156] Cristian Iacovita et al. “Controlling the Dimensionality and Structure of Supramolecular Porphyrin Assemblies by their Functional Substituents: Dimers, Chains, and Close-Packed 2D Assemblies”. In: *Chemistry - A European Journal* 18.46 (Nov. 12, 2012), pp. 14610–14613. ISSN: 09476539. DOI: 10.1002/chem.201201037. URL: <http://doi.wiley.com/10.1002/chem.201201037> (visited on 07/13/2015).
- [157] Geoffrey Rojas et al. “Surface state engineering of molecule–molecule interactions”. In: *Physical Chemistry Chemical Physics* 14.14 (2012), p. 4971. ISSN: 1463-9076, 1463-9084. DOI: 10.1039/c2cp40254h. URL: <http://xlink.rsc.org/?DOI=c2cp40254h> (visited on 08/29/2018).
- [158] Stefano Gottardi et al. “Cyano-Functionalized Triarylaminies on Au(111): Competing Intermolecular versus Molecule/Substrate Interactions”. In: *Advanced Materials Interfaces* 1.1 (Feb. 2014), p. 1300025. ISSN: 21967350. DOI: 10.1002/admi.201300025. URL: <http://doi.wiley.com/10.1002/admi.201300025> (visited on 01/18/2018).
- [159] Steven De Feyter and Frans C. De Schryver. “Two-dimensional supramolecular self-assembly probed by scanning tunneling microscopy”. In: *Chemical Society Reviews* 32.3 (Apr. 24, 2003), pp. 139–150. ISSN: 03060012, 14604744. DOI: 10.1039/b206566p. URL: <http://xlink.rsc.org/?DOI=b206566p> (visited on 08/21/2018).

Appendix

1 Crystal facets

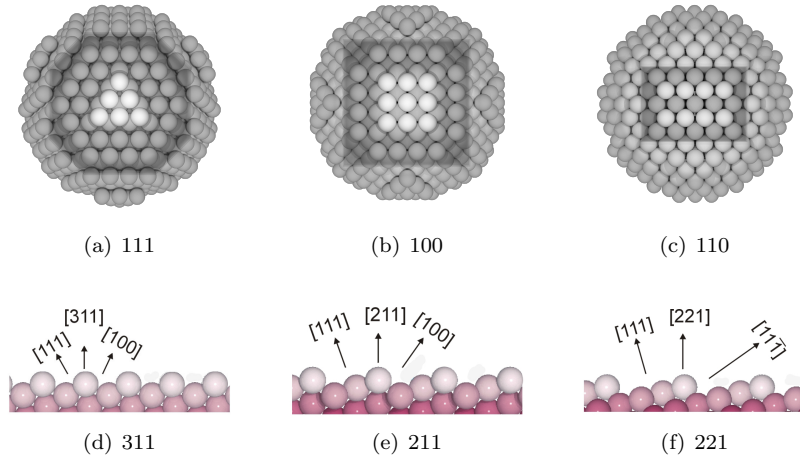


Figure 1: Hard sphere models of different surface facets for a fcc crystal. (a)-(c) Same fcc crystalline cluster, viewed along the different surface normal of surface orientations (111), (110) & (100). Terraces are parallel to the paper plane. (d)-(e) Higher order facets are shown from the side as they may be present on an unordered polycrystalline surface. 4(311), (211) & (221) consist of (111) terraces separated by steps that form a regular stepped surface. **311**: (100) steps run parallel to $[0\bar{1}1]$, rhombic unit cell. Terrace is 4.23 Å (two close-packed rows) wide and inclined by 33.5 deg, steps by 146.4 deg with respect to the surface normal. **211**: (100) steps run parallel to $[01\bar{1}]$ crystal direction. Rectangular unit cell. Terraces are four close-packed row wide (7.66 Å) and inclined by 19.5 deg, steps by 35.3 deg with respect to the 221 surface normal. 0.74 Å interlayer spacing. **221**: (111) steps parallel to $[\bar{1}10]$. Steps go up in $[\bar{1}\bar{1}4]$, rectangular unit cell. Terraces are 7.66 Å wide, inclined by 15.8 deg, steps by 54.7 deg with respect to the [221] surface normal. 0.6 Å interlayer spacing. Lower graphics row adapted from [56].

2 Orbital calculations for pyrene molecules

In this section extended hückel theory calculations of functionalized pyrene molecules are shown. After structural relaxation via the AM1 semi-empirical method in the Hyperchem software, the result is exported to an IGOR script for presentation. Single molecular orbitals as well as their sum can be shown. For all molecules some basic information is given in a box. The number of atoms, electrons and calculated orbitals is given together with a ball and stick model of the corresponding molecule. Calculated HOMO/LUMO states are shown to the right with their energies noted below. The left side of the pages shows occupied states (second column) and their sum (first column). The right side shows the unoccupied in the same manner.

The first two pages will show cis-pyrene as calculated in gas phase together with a model showing the rotation of pyridil legs and the influence on molecular orbitals. Trans- & tetra-pyrene molecules are shown afterwards.

Due to the same molecular center, all the species show distinct symmetry at their pyrene center.

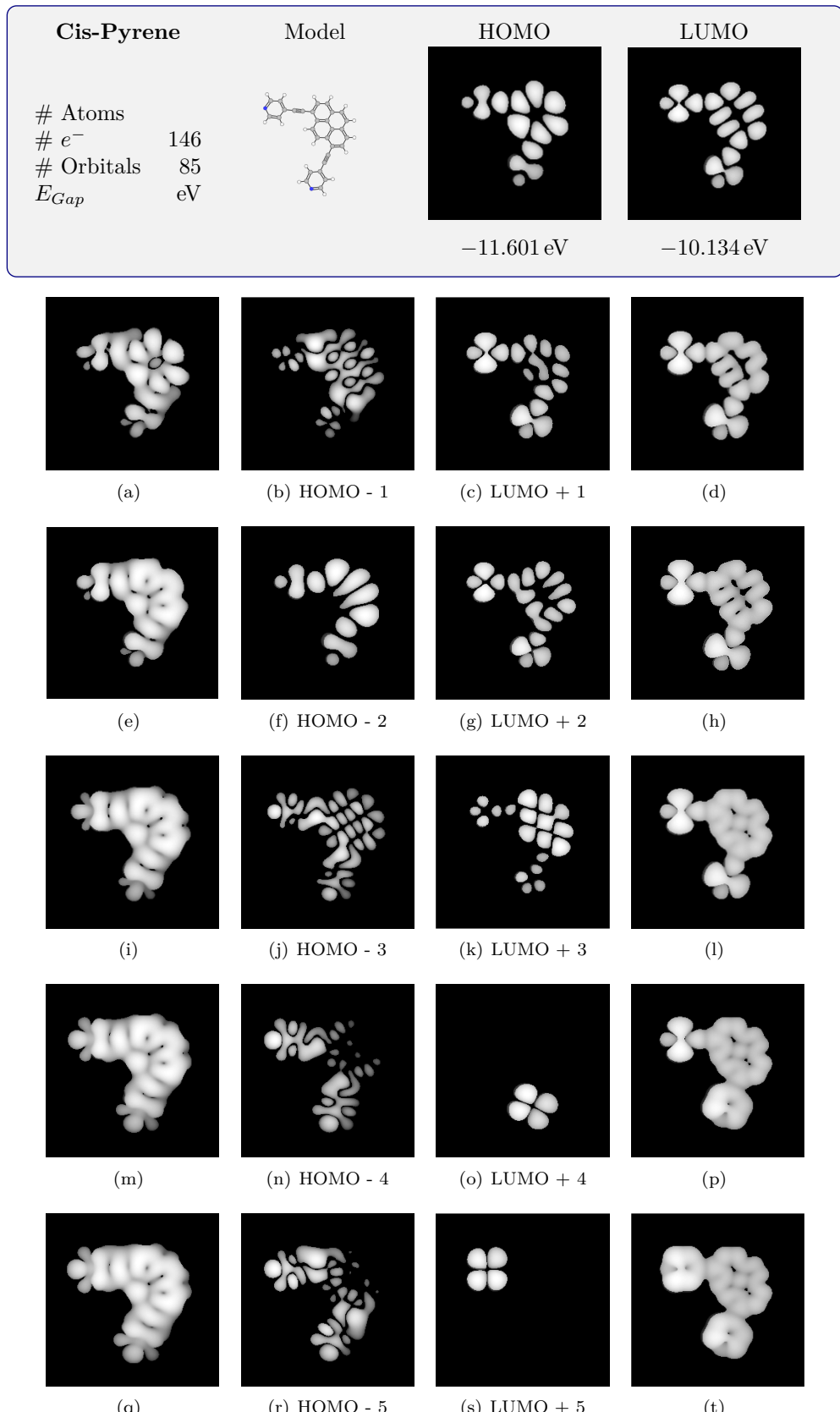


Figure 2: EHT calculated molecular orbitals. HOMO and LUMO states together with five neighboring states (shown in the same column). Inner two columns show HOMO & LUMO states. Outer columns show integration of states as STM image estimation if all states to E_F were contributing equally. Images are 2.5 nm wide

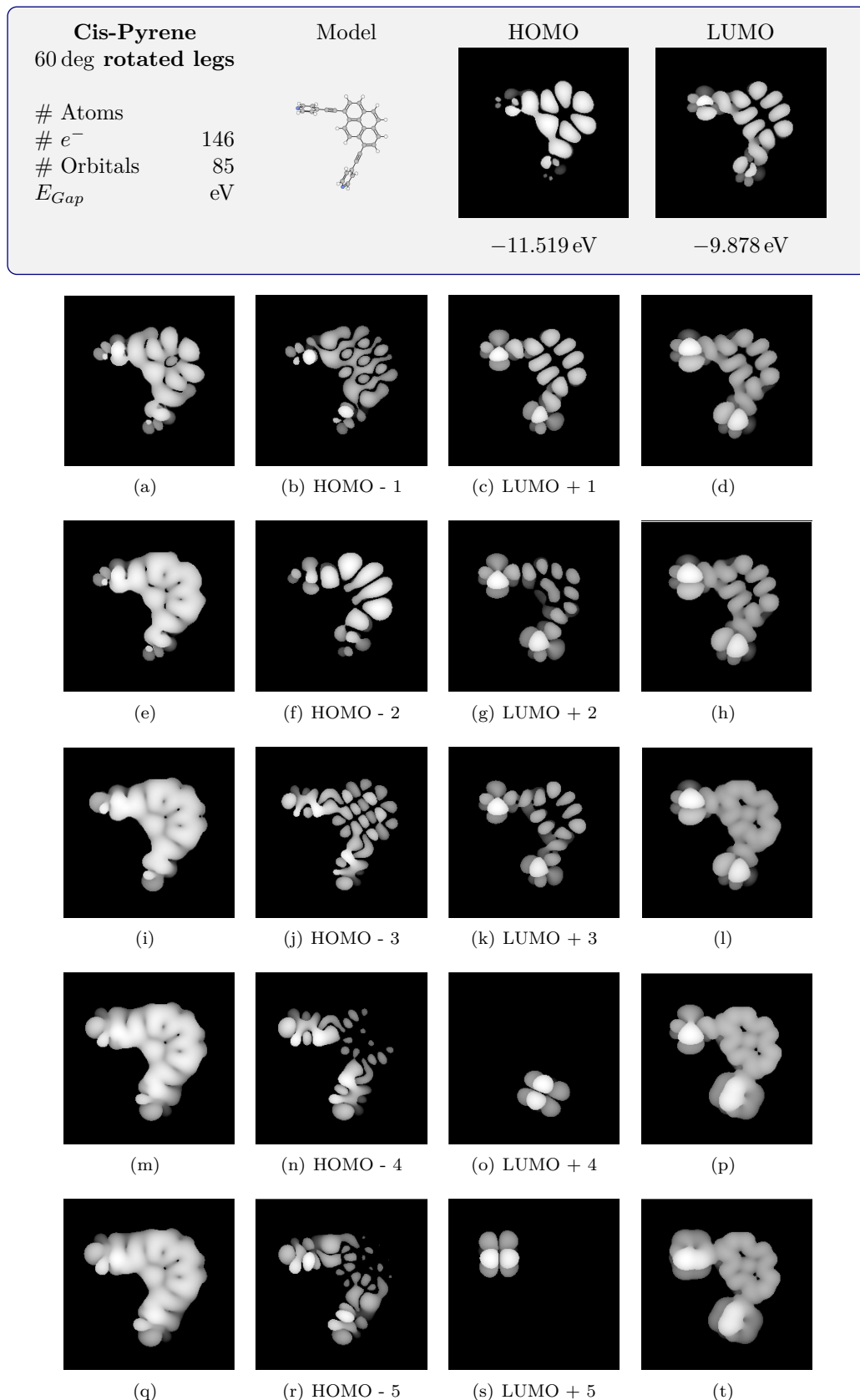


Figure 3: EHT calculated molecular orbitals. HOMO and LUMO states together with five neighboring states (shown in the same column). Inner two columns show HOMO & LUMO states. Outer columns show integration of states as STM image estimation if all states to E_F were contributing equally. Images are 2.5 nm wide

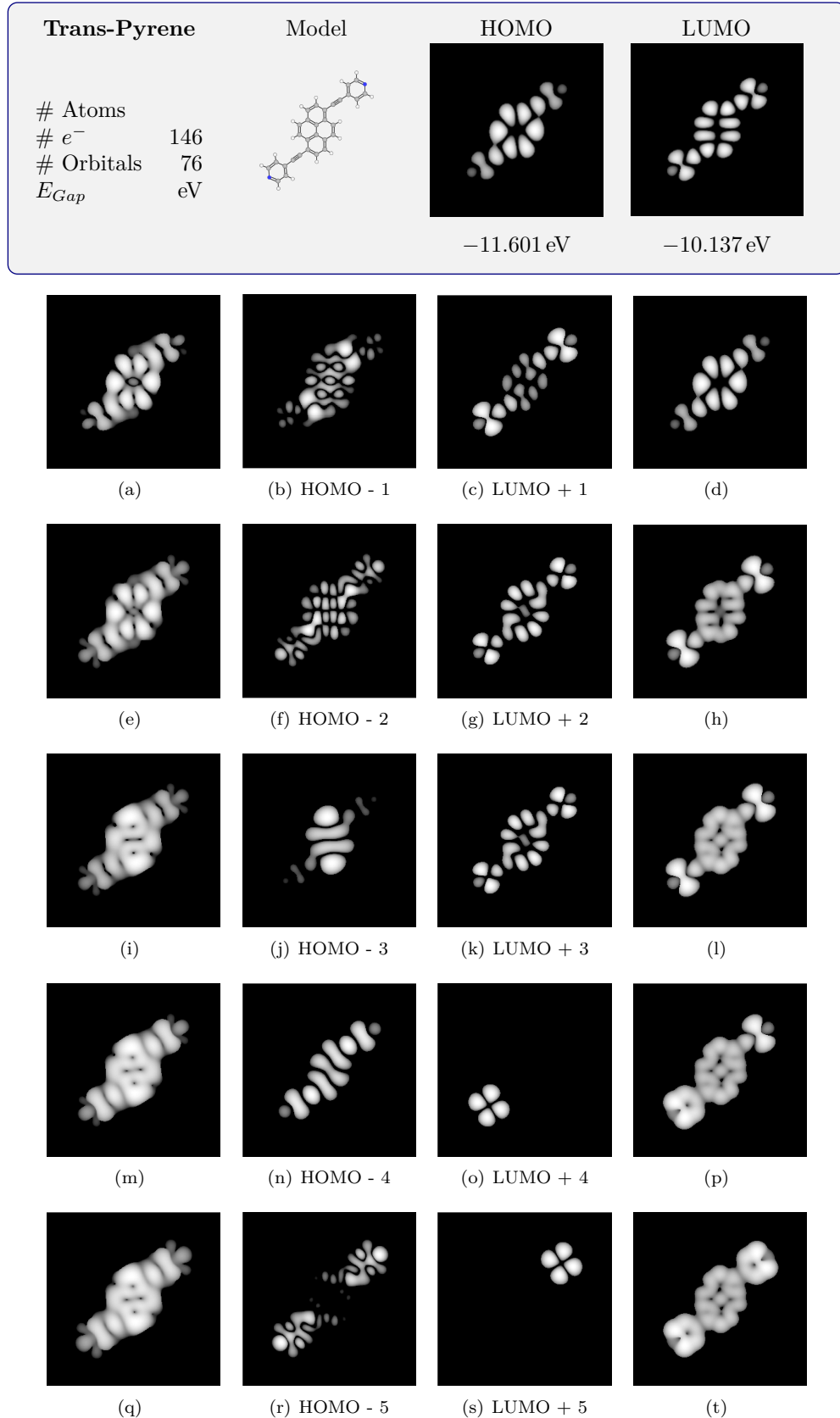


Figure 4: EHT calculated molecular orbitals. HOMO and LUMO states together with five neighboring states (shown in the same column). Inner two columns show HOMO & LUMO states. Outer columns show integration of states as STM image estimation if all states to E_F were contributing equally. Images are 2.5 nm wide

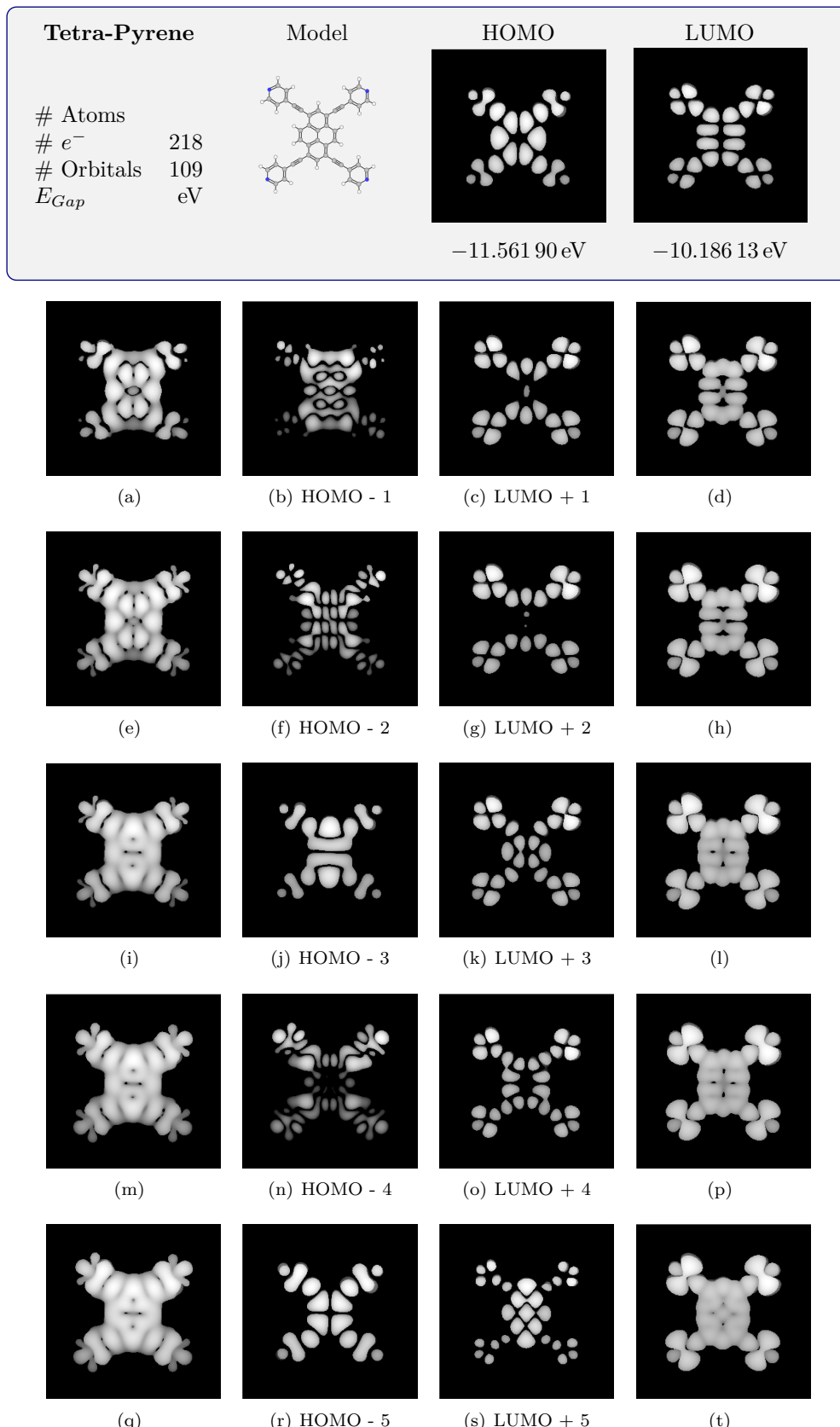
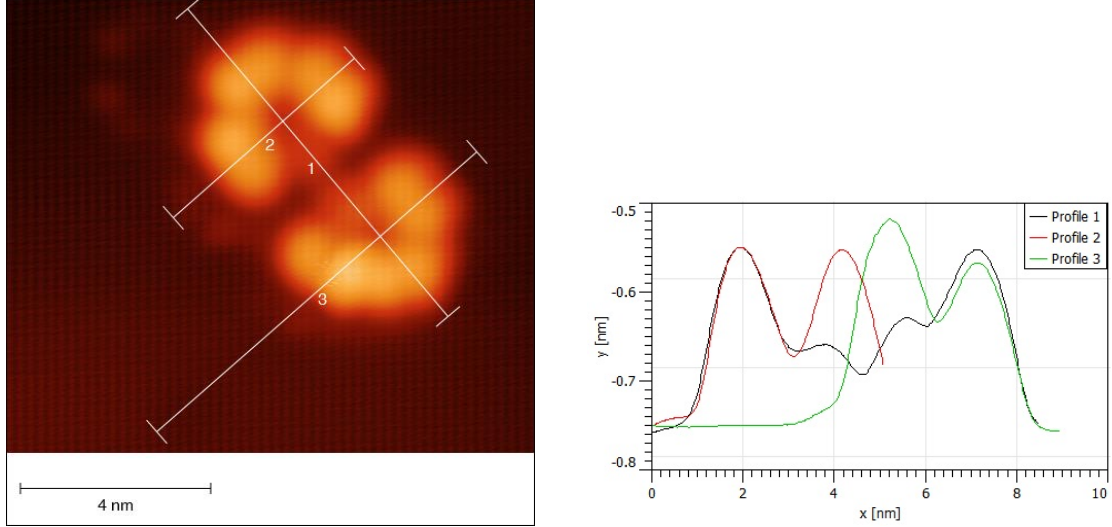


Figure 5: EHT calculated molecular orbitals. HOMO and LUMO states together with five neighboring states (shown in the same column). Inner two columns show HOMO & LUMO states. Outer columns show integration of states as STM image estimation if all states to E_F were contributing equally. Images are 2.5 nm wide



(a) Molecule with chosen profiles (1-3) indicated as white lines.

(b) Profiles 1-3 indicated in a). Local minima in profile 2/3 indicate central positions in profile 1.

Figure 6: Sketch of how to determine the distance between two molecules. As the molecule is square (with the exception of one direction, one can determine the center of the molecule by comparing two 90 deg rotated profiles. Profile 1 goes through the symmetry axis, while profile 2 and 3 intersect profile 1 at the center. As the profile 2 and 3 look the same when starting at the butyl groups, one can use the depression in profile 2 and 3 to determine the center of the molecule in profile 1.

How to determine molecules' distance To determine the distance between molecules, one has to carefully choose the points of interest. As a problem of STM imaging the contour of the molecules sometimes appears as more or less fuzzy shape. There is no sharp edge that one could take as start or end point of the profile. Therefore the center of the molecule is often used as reference point to measure the distance between two molecules (compare fig. 6). As the molecule has a square footprint, one can use the center in one direction (along profile 2/3) to determine the center in the other direction (profile 1). As one can see the three profiles match leading to a consistent center of the dimer. This is also shown as depression in profile 1.

```

1 # -*- coding: utf-8 -*-
2 """
3 See https://github.com/ga32xan/Maxigauge-TPG256A for documentation and electronic copy of the code
4 python Maxigauge-TPG256A.py -h
5
6 Created on Thu Nov 16 12:59:26 2017
7 Author: Mathias Portner, Domenik Zimmermann
8 Versions: To make it run, install python 3.6
9 Additional dependencies: matplotlib, numpy
10 For Windows: Anaconda is a bundled Python version (https://anaconda.org/anaconda/python)
11 For Linux: See above or
12 sudo apt-get install python3 pip, pip install matplotlib, pip install numpy, pip install serial
13
14 Edit this file with 4 space indentation
15
16 """
17
18 ''' This is for the serial connection and throughout the script :) '''
19 import serial
20 import time
21 import os
22 import datetime as dt
23
24 ''' This is for all the plotting stuff '''
25 import matplotlib.pyplot as plt
26 import matplotlib.dates as mdate
27 import numpy as np
28
29 ''' This is imported because of the logging facility and command line arguments '''
30 import argparse # for the argument parsing stuff and -h explanation
31 import logging # for logging purposes
32
33 ''' This is imported because of the module version logging '''
34 import inspect
35 import sys
36 import re
37

```

```
38 date_fmt = '%d-%m-%Y %H.%M.%S'
39 datenow = dt.datetime.now().strftime(date_fmt)
40
41 ''' Create helper when script is used wrong! '''
42 ''' Parses arguments given in command line '''
43 parser = argparse.ArgumentParser(
44     description = 'Reads pressures from Pfeiffer Maxigauge TPG256A and \
45                 shows interactive graph if wanted',
46     epilog = 'For detailed documentation see source code or visit \
47               http://github.com/ga32xan/Maxigauge-TPG256A'
48 )
49
50 parser.add_argument('--loglevel', '-v', \
51                     help = 'Minimum numeric loglevel/serverity: \n \
52                           Debug, Info, Warning, Error, Critical.\n \
53                           This switch does not affect the pressure log, \
54                           which is always written in the same detail.\n \
55                           Defaults to Warning.', \
56                     type = str, \
57                     default = 'Warning', \
58 )
59
60 parser.add_argument('--programlogfile', '-pl', \
61                     help = 'What filename should the pressure log have? \
62                           Always written to the directory where script is located\
63                           Defaults to control.log', \
64                     type = str, \
65                     default = 'control.log', \
66 )
67
68 parser.add_argument('--pressurelogfile', '-l', \
69                     help = 'What filename should the pressure log have? Always \
70                           written to the directory where script is located\
71                           Defaults to pressure.log', \
72                     type = str, \
73                     default = 'pressure.log', \
74 )
75
76 parser.add_argument('--plot', '-p', \
77                     help = 'Plot graph? Do not use outside spyder (Anaconda), yet!\\
```

```

78     Defaults to False. ,
79     action = 'store_true' , \
80     #default = False| #can be omitted since its the default behaviour
81 )
82
83 parser.add_argument('—comport', '-c', \
84                     help = 'What port to use? Defaults to 8.', \
85                     type = int, \
86                     default = 8\
87 )
88
89 arguments = parser.parse_args()
90
91 ''' Takes argument loglevel and programlogfile from the argparse \
92 and passes it to the logging facility '''
93 loglevel = arguments.loglevel # is str like debug, info, DeBUG or something similar
94 # compares to available loglevels and transforms into number
95 numeric_loglevel = getattr(logging, loglevel.upper(), None)
96 if not isinstance(numeric_loglevel, int):
97     raise ValueError('Invalid log level: %s' % loglevel)
98
99 suffix = arguments.programlogfile.split('.')[0]      #filename
100 ending = arguments.programlogfile.split('.')[1]      #file type
101 prefix = '%s - %datenow.replace(':', '-')
102
103 programlogfile_name = os.getcwd() + '\\\\' + prefix + suffix + '.' + ending
104 #print('Program Logging goes to : ' + programlogfile_name)
105
106 logging.basicConfig(filename = programlogfile_name, \
107                     format = '%(asctime)s %(message)s', \
108                     datefmt = '%d-%m-%Y %H:%M:%S', \
109                     filemode = 'a', \
110                     level = numeric_loglevel\
111 )
112
113 ''' Takes argument pressurelogfile from the argparse '''
114 ''' Gets and splits command line argument into prefix.ending and returns appended date '''
115 suffix = arguments.pressurelogfile.split('.')[0]      #filename
116 ending = arguments.pressurelogfile.split('.')[1]      #file type
117 prefix = '%s - %datenow.replace(':', '-')
99

```

```

100
118 pressurelogfile_name = os.getcwd() + '\\\\' + prefix + suffix + '.' + ending
119     ''' Takes argument comport from the argparse '''
120 com_port = arguments.comport
121
122     ''' Takes argument plot from the argparse '''
123     ''' Boolean to indicate if auto-updating matplotlib-graph is wanted '''
124     ''' Piviledge Error if not executed within Anaconda '''
125     ''' Set to False if script is exucuted from command line '''
126     ''' Set to true if run in IDE (tested: Anaconda) '''
127 plot = arguments.plot
128
129
130 logging.info('Using COM-Port : ' + str(com_port))
131 logging.info('Pressure Logging goes to : ' + pressurelogfile_name)
132 logging.info('Program Logging goes to : ' + programlogfile_name)
133 logging.info('Program Debug level is : ' + arguments.loglevel + '(' + str(numeric_loglevel) + ')')
134 logging.info('Do i plot something? : ' + str(plot))
135
136 def read_gauges(ser):
137     ''' Reads all 6 channels and returns status and (if applicable) pressure '''
138     ''' There is one list for status[CH] called stat and one for pressure[CH] called press returned '''
139     logging.debug('#####read_gauges#####')
140     ser.flushInput()
141
142     press = []
143     stat = []
144     for j in range(6):                      # for each channel
145         ''' request data for specific channel '''
146         send_command(ser, 'PR%i\r\n%(j+1)' ) #request channel
147         send_command(ser, '\x05')           #enquire data
148
149         ''' what the controller returns is something like 'x,x.xxxEsx <CR><LF>' '''
150         x[Status],[x.xxxEsx] Measurement value (always engineers' format)
151         0 Measurement data okay, 1 Underrange, 2 Overrange
152         3 Sensor error, 4 Sensor off, 5 No sensor, 6 Identification error
153
154
155     logging.debug('#####splitting received pressure string#####')
156     string=read_port(ser).split(',')          # splits read string into string[-1], string[0]
157     logging.debug(string)

```

```

158     string_pres=str(string[1])           #pressure value converted to string
159     logging.debug('Read pressure : ' + string_pres)
160     string_sta=int(string[0][-1])       #status value converted to int
161     logging.debug('Read status : ' + str(string_sta))
162     press.append(float(string_pres))    #append float of pressure to press-list
163     stat.append(int(string_sta))        #append int(status) to status list
164
165     return(stat,press)
166
166 def send_command(ser,command):
167     ''' Takes ascii string 'command' and converts it to bytes to send it over serial connection '''
168     logging.debug('#####ser_command#####')
169     input = command.encode('utf-8')      #encode as utf-8
170     logging.debug('Command string: ' + str(input))
171     convininput=to_bytes(input)          #convert to byte sequence
172     logging.debug('byte-input (as str repre): ' + str(convininput.decode('utf-8')))
173     logging.debug('CTS line: ' + str(ser.cts))
174     logging.debug('DSR line: ' + str(ser.dsr))
175     ser.write(convininput)              #send to wire
176     time.sleep(0.05)
177     logging.debug('Send Command: ' + str(input))
178
179 def read_port(ser):
180     ''' Reads serial port, gets bytes over wire, decodes them with utf-8'''
181     ''' and returns string with received message'''
182     logging.debug('#####read_port#####')
183     logging.debug('Am I outWaiting?: ' + str(ser.out_waiting))
184     logging.debug('Am I inWaiting?: ' + str(ser.in_waiting))
185     logging.debug('Input buffer size: ' + str(ser.in_waiting))
186     logging.debug('CTS line: ' + str(ser.cts))
187     logging.debug('DSR line: ' + str(ser.dsr))
188     out = ''                          #string to hold the received message, empty one for new reading
189     input_buffersize = ser.in_waiting  #input_buffersize: Numbers of bytes received
190     if input_buffersize == 0:
191         logging.warning('No data in input buffer...No data received')
192     while input_buffersize > 0:
193         ''' runs through twice to check consistency of received message '''
194         ''' if first read msg matches snd read msg the input is believed to be consistend '''
195         ''' No error handling. '''
196         ''' Program breaks at this point if no meaningfull serial connection is established '''
197         logging.debug('Input buffersize: ' + str(input_buffersize))

```

```
102
198     logging.debug('... ser.read ...')
199     input_buffersize_old = 0
200     time.sleep(0.05)
201     out += ser.read(64).decode('utf-8')
202     logging.debug('accomplished')
203     if input_buffersize == input_buffersize_old:
204         logging.debug('Received msg: ' + str(out))
205         break
206     else:
207         input_buffersize = input_buffersize_old
208     return out
209     logging.debug('Received msg: ' + str(out))
210
211 def test_connection(ser):
212     logging.debug('#' * 16 + 'test_connection' + '#' * 16)
213     ''' Unimplemented testing routine to test the serial connection object passed as ser '''
214     send_command(ser, 'PR%1\r\n%' + str(j+1)) #request Channel 1-6
215     send_command(ser, '\x05') #enquire data
216     read_port(ser)
217     if True:
218         ''' !Some Check routine missing! '''
219
220 def log_serial_info(ser):
221     ''' Get information about the serial connection, prints only if debug loglevel is chosen '''
222     logging.debug('#' * 16 + 'log_serial_info' + '#' * 16)
223
224     logging.debug('#' * 16 + 'Information about connection:' + '#' * 16)
225     logging.debug('Name of device: ' + ser.name)
226     logging.debug('@ port : ' + ser.port)
227     logging.debug('Port is open?: ' + str(ser.is_open))
228     logging.debug('state of ...')
229     logging.debug('... CTS line: ' + str(ser.cts))
230     logging.debug('... DSR line: ' + str(ser.dsr))
231     logging.debug('... RI line: ' + str(ser.ri))
232     logging.debug('... CD line: ' + str(ser.cd))
233
234     logging.debug('#' * 16 + 'Can set values to:' + '#' * 16)
235     logging.debug('port: ' + ser.port)
236     logging.debug('baudrate: ' + str(ser.baudrate))
237     logging.debug('bytesize: ' + str(ser.bytesize))
```

```

238     logging.debug('parity: ' + str(ser.parity))
239     logging.debug('stopbits: ' + str(ser.stopbits))
240     logging.debug('read_timeout: ' + str(ser.timeout))
241     logging.debug('write_timeout: ' + str(ser.write_timeout))
242     logging.debug('inter_byte_timeout: ' + str(ser.inter_byte_timeout))
243     logging.debug('software_flow_control_setting: ' + str(ser.xonxoff))
244     logging.debug('hardware_flow_control_setting_of ...')
245     logging.debug('\t \t \t \t ... CTS line: ' + str(ser.rtscts))
246     logging.debug('\t \t \t \t ... DSR line: ' + str(ser.dsrdtr))
247     logging.debug('RS485_settings: ' + str(ser.rs485_mode))
248
249 def log_module_info():
250     ''' This will print all the used modules together with their mapping to the logfile '''
251     for name, val in sys._getframe(1).f_locals.items():
252         if inspect.ismodule(val):
253
254             fullnm = str(val)
255
256             if not '(built-in)' in fullnm and \
257                 not __name__ in fullnm:
258                 m = re.search(r'^(.+)\.*(.+)$', fullnm)
259                 module, path = m.groups()
260                 logging.info("%-12s maps to %s" % (name, path))
261                 if hasattr(val, '__version__'):
262                     logging.info("\t Version: " + val.__version__)
263                 else:
264                     logging.info("\t No version listed in val.__version__")
265
266 def init_serial(com_port):
267     ''' Initializes serial connection, defaults to COM5 '''
268     logging.debug('#' * 16 + 'init_serial' + '#' * 16)
269     try:
270         ser = serial.Serial(timeout=0.5,\
271                             baudrate=9600,\
272                             stopbits=serial.STOPBITS_ONE,\
273                             bytesize=serial.EIGHTBITS,\
274                             parity=serial.PARITY_NONE\
275                         )
276         ser.port = 'COM' + str(com_port)
277         ser.open()
103

```

```

104
278     ser.reset_input_buffer()
279     ser.reset_output_buffer()
280     if numeric_loglevel < 30: log_serial_info(ser)
281     logging.debug('init_serial on COM' + str(com_port) + 'successfully')
282     return ser
283 except IndexError as err:
284     logging.critical('Opening of com-port failed')
285     print('Failed opening serial port at port' + str(ser.port))
286     print('Make sure you are on the right COM port and try reloading the console')
287
288 def to_bytes(seq):
289     ''' Convert a sequence of int/str to a byte sequence and returns it '''
290     logging.debug('#' * 10 + 'to_serial#' * 10)
291     if isinstance(seq, bytes):
292         return seq
293     elif isinstance(seq, bytearray):
294         return bytes(seq)
295     elif isinstance(seq, memoryview):
296         return seq.tobytes()
297     else:
298         b = bytearray()
299         for item in seq:
300             b.append(item) # this one handles int and str for our emulation and int for Python 3.x
301         return bytes(b)
302     logging.debug('Byte-conversion for ' + str(seq) + ' done')
303
304 def update_terminal(time, labels, pressures):
305     """ Print information to the console """
306     os.system('cls' if os.name == 'nt' else 'clear') #clear console screen
307     pressures_show = []
308     pressures_last = []
309     for j in range(6):
310         pressures_last.append(pressures[j][-1])
311     for n, i in enumerate(pressures_last):
312         if i == 1e10:
313             pressures_show.append('\tNAN\t')
314         else:
315             pressures_show.append(str(i))
316     print(time + ': \t ... running ...')
317     print('Program Logging goes to : ' + programlogfile_name)

```

```

318 print('Pressure Logging goes to : ' + pressurelogfile_name)
319 print('#' + labels[0] + '\t|\t' + \
320      labels[1] + '\t|\t' + \
321      labels[2] + '\t|\t' + \
322      labels[3] + '\t|\t' + \
323      labels[4] + '\t|\t' + \
324      labels[5] + '\t#')
325
326 print('# %s\t| %s\t| %s\t| %s\t| %s\t| %s\t| %s #' + \
327      %(pressures_show[0], pressures_show[1], pressures_show[2], \
328        pressures_show[3], pressures_show[4], pressures_show[5]))
329
330
331 def get_labels(ser):
332     ''' Get and return all the channel names from the controller '''
333     send_command(ser, 'CID\r\n') # request channel
334     ''' Check for ACK '''
335     send_command(ser, '\x05') # enquire data
336     labels_raw = read_port(ser).split(',')
337     logging.debug('Receiving channel names:')
338     logging.debug(labels_raw[0][3:]) # slices the \x06\r\n in beginning of MSG
339     logging.debug(labels_raw[1])
340     logging.debug(labels_raw[2])
341     logging.debug(labels_raw[3])
342     logging.debug(labels_raw[4])
343     logging.debug(labels_raw[5][: -2]) # slices ending \r\n'
344     labels = [labels_raw[0][3:], \
345               labels_raw[1], \
346               labels_raw[2], \
347               labels_raw[3], \
348               labels_raw[4], \
349               labels_raw[5][: -2]]
350     logging.info('Returning Labels: ' + str(labels))
351     return labels
352 ##### Main routine #####
353 if __name__ == '__main__':
354     ''' Messy routine that updates the data, plot it and updates the logfile '''
355     ''' Every time the program is started and writes to the same logfile a line of # is added '''
356     ''' TODO: cleanup, write subroutine update_plot and write_logfile '''
357     print('... starting up ...')

```



```

398     for sensor_num, status in enumerate(stat):
399         logging.debug('#####updating pressures inside main#####')
400         logging.info('Sensor: ' + str(sensor_num))
401         if status == 0:
402             logging.info('Channel OK')
403             pressures[sensor_num].append(stpre[sensor_num])
404             if plot:
405                 if pressures[sensor_num][-1] > 1e-1:
406                     labels[sensor_num] = labels_begin[sensor_num]+ \
407                         r' $\rightarrow$ %.2e mbar' % pressures[sensor_num][-1]
408                 elif pressures[sensor_num][-1] <= 1e-1:
409                     labels[sensor_num] = labels_begin[sensor_num]+ \
410                         r' $\leftarrow$ %.2e mbar' % pressures[sensor_num][-1]
411             elif status == 1:
412                 logging.warning('Channel Underrange')
413                 pressures[sensor_num].append(1e10)
414                 if plot: labels[sensor_num] = labels_begin[sensor_num]+ ' - Underrange'
415             elif status == 2:
416                 logging.warning('Channel OVERRANGE')
417                 pressures[sensor_num].append(1e10)
418                 if plot: labels[sensor_num] = labels_begin[sensor_num]+ ' - OVERRANGE'
419             elif status == 3:
420                 logging.error('Channel Error')
421                 pressures[sensor_num].append(1e10)
422                 if plot: labels[sensor_num] = labels_begin[sensor_num]+ ' - Error'
423             elif status == 4:
424                 logging.info('Channel Off')
425                 pressures[sensor_num].append(1e10)
426                 if plot: labels[sensor_num] = labels_begin[sensor_num]+ ' - Off'
427             elif status == 5:
428                 logging.info('Channel Not found')
429                 pressures[sensor_num].append(1e10)
430                 if plot: labels[sensor_num] = labels_begin[sensor_num]+ ' - Not found'
431             elif status == 6:
432                 logging.error('Channel Identification Error')
433                 pressures[sensor_num].append(1e10)
434                 if plot: labels[sensor_num] = labels_begin[sensor_num]+ ' - Identification error'
435             with open(pressurelogfile_name, "a") as logfile:
436                 logfile.write("%s\t%.2e\t%.2e\t%.2e\t%.2e\t%.2e\t%.2e\t%.2e\n" \
437                               %(datenow, \

```

```

108    pressures[0][0], pressures[1][0], pressures[2][0], \
109    pressures[3][0], pressures[4][0], pressures[5][0]))
110    ''' Prepare plot '''
111 if plot:
112     logging.debug('Preparing plot')
113     fig = plt.figure(figsize=(10,6), dpi=100)
114     ax = fig.add_subplot(111)
115     plt.ion()                      #autoupdate plot
116     plt.yscale('log')
117
118     sens = {}
119     col = [ 'b' , 'r' , 'g' , 'K' , 'c' , 'y' ] #colors
120
121     #For each sensors, choose a different color and plot them all on one axis
122     for j in range(6):
123         sens['sen{0}'.format(j)], = \
124             ax.plot(times, pressures[j], '.', ls = '--', color = col[j], label=labels[j])
125     #configure left axis
126     ax.set_ylimits(1e-12,1e-4)
127     ax.set_xlabel('Time')
128     ax.set_ylabel('Pressure [mbar]')
129
130     ax.legend()
131     plt.gca().xaxis.set_major_formatter(mdate.DateFormatter(date_fmt))
132     plt.gcf().autofmt_xdate()
133
134     ax2 = ax.twinx()
135     #Plot every sensor with a pressure > 1e-1 on the second axis
136     for j in range(6):
137         if pressures[j][-1] > 1e-1:
138             sens['sen{0}'.format(j)], = ax2.plot(times, pressures[j], '.', ls = '--', color = col[j])
139     #configure right axis
140     ax2.set_ylimits(1e-1,1e3)
141     ax2.set_yscale('log')
142     ax2.set_ylabel('Pressure [mbar]')
143
144     logging.info('Start Looping')
145     while True:
146         logging.debug('Loop-Top')
147         ''' Keep Com port open for only a short amount of time so that '''

```

```

478         ''' if the program is killed it is most likely in a closed state '''
479         ''' This should be done via a try: except: statement to make it exit nicely '''
480         labels=[', ',', ',', ',', ',', ',', ',']
481         ''' Continuously read data '''
482         if ser.is_open:
483             status,pre = read_gauges(ser)
484             ser.close()
485         else:
486             ser.open()
487             status,pre = read_gauges(ser)
488             ser.close()
489
490         ''' Keep track of changing labels - Crashes program when labels are changed! '''
491
492         labels_old = labels
493         if not labels_old == labels:
494             with open(pressurelogfile_name, "a") as logfile:
495                 logfile.write('#labelschanged')
496                 logfile.write('Time|t|t|t|t|t|t|')
497                 + labels[0] + '[mbar]|t|t|' + labels[1] + '[mbar]|t|t|' + labels[2] + '[mbar]|t|t|'
498                 + labels[3] + '[mbar]|t|t|t|' + labels[4] + '[mbar]|t|t|t|' + labels[5] + '[mbar]|n|')
499
500         datenow = dt.datetime.now().strftime(date_fmt)
501         times.append(mdate.datestr2num(datenow))
502
503         ''' To update the legend when a sensor is switched on/off '''
504         ''' we have to check every time we read a value '''
505         ''' Updates values in pressure lists '''
506         if plot: ax.legend_.remove()
507         for num,sensor in enumerate(status):
508             if sensor == 0:
509                 pressures[num].append(pre[num])
510                 if plot:
511                     if pressures[num][-1] > 1e-1:
512                         labels[num] = labels_begin[num]+r'$\rightarrow$ %.2e mbar'%pressures[num][-1]
513                     elif pressures[num][-1] <= 1e-1:
514                         labels[num] = labels_begin[num]+r'$\leftarrow$ %.2e mbar'%pressures[num][-1]
515             elif sensor == 1:
516                 pressures[num].append(1e10)
517                 labels[num] = labels_begin[num]+'- Underrange'

```

```

110    518 elif sensor == 2:
111        519     pressures[num].append(1e10)
112        520     labels[num] = labels_begin[num]+ ' - Overrange'
113    521 elif sensor == 3:
114        522     pressures[num].append(1e10)
115        523     labels[num] = labels_begin[num]+ ' - Error'
116    524 elif sensor == 4:
117        525     pressures[num].append(1e10)
118        526     labels[num] = labels_begin[num]+ ' - Off'
119    527 elif sensor == 5:
120        528     pressures[num].append(1e10)
121        529     labels[num] = labels_begin[num]+ ' - Not found'
122    530 elif sensor == 6:
123        531     pressures[num].append(1e10)
124        532     labels[num] = labels_begin[num]+ ' - Identification error'
125
126    533     ''' Write to log '''
127    534 with open(pressurelogfile_name, "a") as logfile:
128        535         logfile.write('%s\t%2e\t%2e\t%2e\t%2e\t%2e\t%2e\n'\
129                     % (datenow,\n
130                         pressures[0][-1], pressures[1][-1], pressures[2][-1],\n
131                         pressures[3][-1], pressures[4][-1], pressures[5][-1]))
132
133    540     ''' Update console output '''
134    541 update_terminal(datenow, labels_begin, pressures)
135    542     ''' Update plot '''
136    543 if plot:
137        544     for j in range(6):
138            545         sens['sen{0}'.format(j)].set_xdata(times)
139            546         sens['sen{0}'.format(j)].set_ydata(pressures[j])
140            547         sens['sen{0}'.format(j)].set_label(labels[j])
141
142            #Set new 'best' place for legend
143            548         ax.legend(loc = 'best')
144
145            #dynamically updating axis range, showing all data
146            549         ax.set_xlim(times[0]-(times[1]-times[0]), times[-1]+(times[1]-times[0]))
147
148            #axis range: 12h
149            550         #ax.set_xlim(dt.datetime.now()-dt.timedelta(hours=12), times[-1]+(times[1]-times[0]))
150
151    553 plt.pause(1)

```

4 Ordered areas of TBP

Ordered areas Only a single ordered area of TBP on Ag(100) was found, but its structure could not be resolved properly due to tip issues (compare figure 7). Its unit cell looks hexagonal with roughly 1.7 nm period.

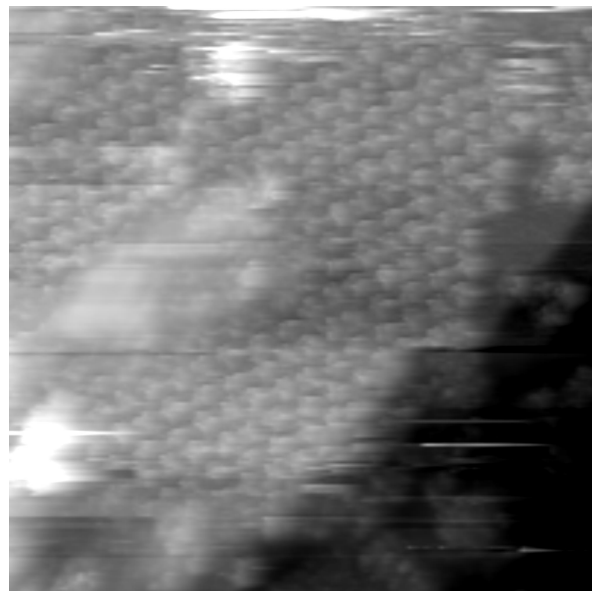


Figure 7: TBP on Ag(100) showing some ordering

TBP on Ag(100) - Symmetry relations

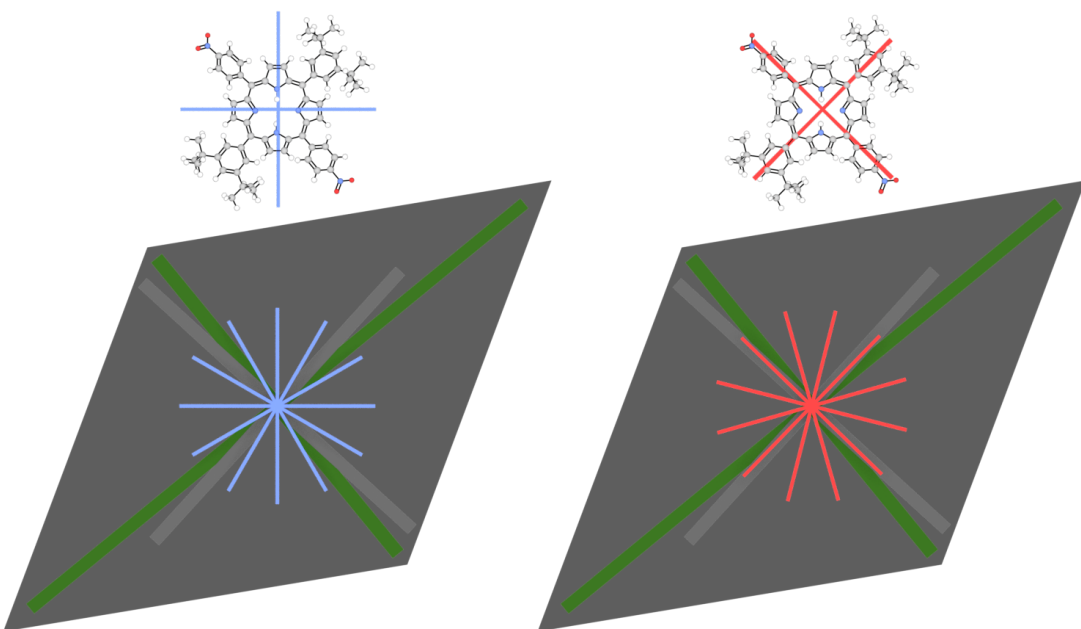


Figure 8: Symmetry relations between TBP molecule and Ag(100) crystal substrate. The same molecular model is highlighted in two different ways, emphasizing the two molecular axis (red/blue). Since the assembly is made up of three different orientations, the three rotated axis sets are shown. The assemblies derived unit cell is shown as shaded background with short and long symmetry axis highlighted in green. The crystal orientation from another preparation on the same single crystal is shown in grey.

5 HBBNC

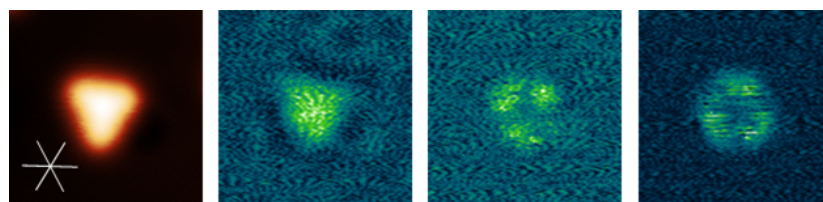


Figure 9: Choosing the spectroscopy energy to match one of the spectral maxima of the line spectra reveals the spatial distribution of electronic states as shown in the STS map. While at 650 meV only the core contributes to the DOS, energies of 1200 meV and 1600 meV are located on the leg and edge positions respectively.

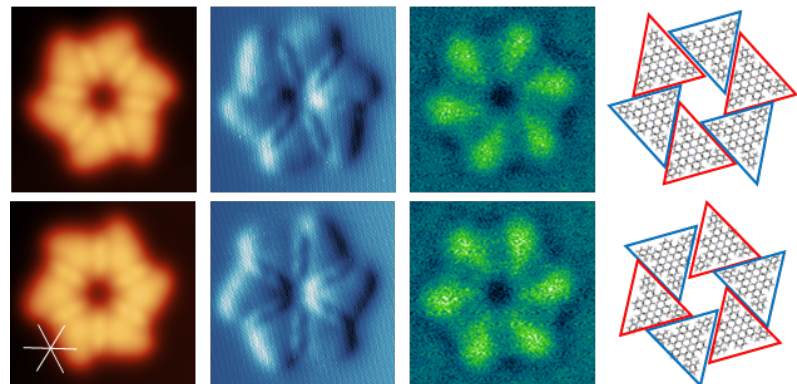


Figure 10: Comparison of two hexamers (chiral twins). While in STM the most apparent change is the orientation of the molecules within the hexamer and the resulting change in the protrusion between them, dI/dV maps (600 meV) clearly highlight the turn direction within the hexamer.

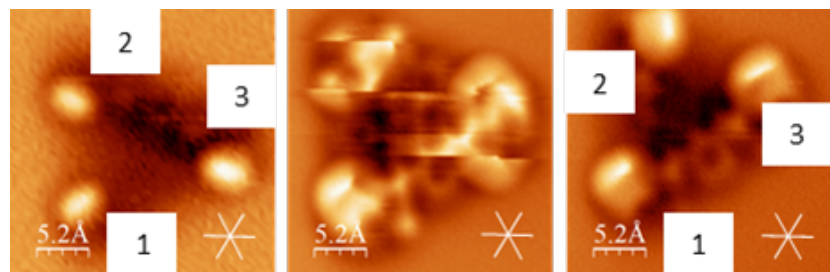


Figure 11: Conformational change of a monomer after several scans with the AFM. First the molecule starts with an orientation of the legs in 1: clockwise, 2: counterclockwise, 3: clockwise. After several scans in close proximity (how far?!) legs at positions 2 and 3 flip around and change their orientation to 1: clockwise, 2: clockwise, 3: counterclockwise. This results in a changed adsorption geometry. First the upper right edge is lifted from the substrate, while after the leg rearrangement the lower right edge is lifted from the surface. This is caused by the lower lying dimethyl groups lifting the phenyl ring and the molecules edge.

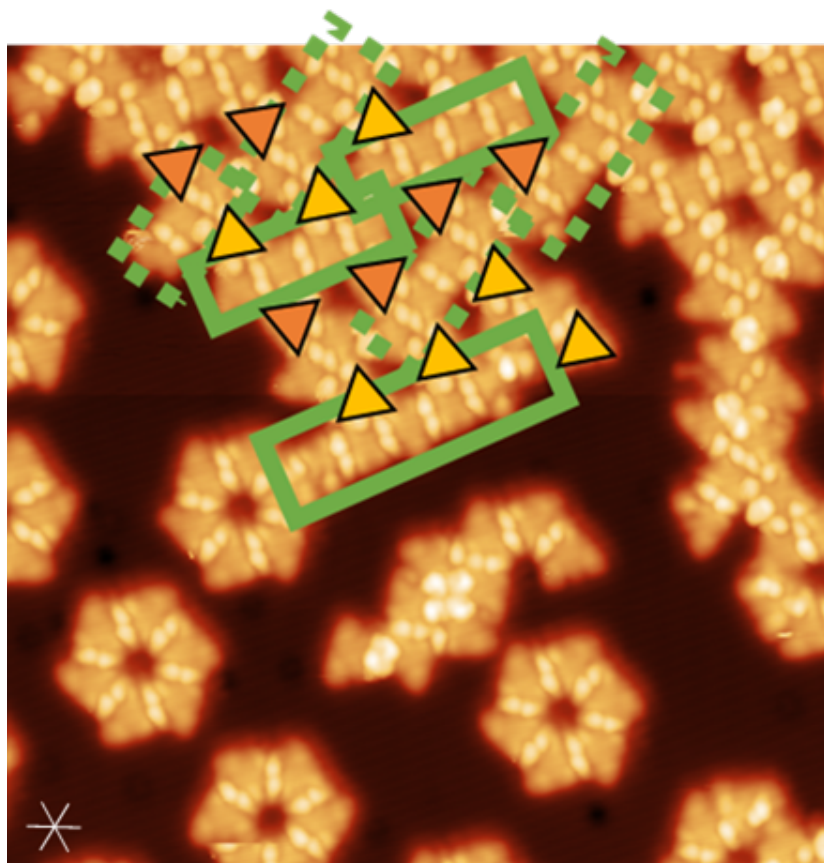


Figure 12: Rows are separated by two sets of spacer molecules (orange/yellow). What is their position in the unit cell? Rotation? Separation to all the other molecules?